

ANL-7854

RETURN TO ANL (IDAFD) LIBRARY.

7854

ANL-7854

Argonne National Laboratory

REACTOR DEVELOPMENT PROGRAM PROGRESS REPORT

August 1971

The facilities of Argonne National Laboratory are owned by the United States Government. Under the terms of a contract (W-31-109-Eng-38) between the U. S. Atomic Energy Commission, Argonne Universities Association and The University of Chicago, the University employs the staff and operates the Laboratory in accordance with policies and programs formulated, approved and reviewed by the Association.

MEMBERS OF ARGONNE UNIVERSITIES ASSOCIATION

The University of Arizona
Carnegie-Mellon University
Case Western Reserve University
The University of Chicago
University of Cincinnati
Illinois Institute of Technology
University of Illinois
Indiana University
Iowa State University
The University of Iowa

Kansas State University
The University of Kansas
Loyola University
Marquette University
Michigan State University
The University of Michigan
University of Minnesota
University of Missouri
Northwestern University
University of Notre Dame

The Ohio State University
Ohio University
The Pennsylvania State University
Purdue University
Saint Louis University
Southern Illinois University
The University of Texas at Austin
Washington University
Wayne State University
The University of Wisconsin

NOTICE

This report was prepared as an account of work sponsored by the United States Government. Neither the United States nor the United States Atomic Energy Commission, nor any of their employees, nor any of their contractors, subcontractors, or their employees, makes any warranty, express or implied, or assumes any legal liability or responsibility for the accuracy, completeness or usefulness of any information, apparatus, product or process disclosed, or represents that its use would not infringe privately-owned rights.

Printed in the United States of America
Available from
National Technical Information Service
U.S. Department of Commerce
5285 Port Royal Road
Springfield, Virginia 22151
Price: Printed Copy \$3.00; Microfiche \$0.95

ARGONNE NATIONAL LABORATORY
9700 South Cass Avenue
Argonne, Illinois 60439

REACTOR DEVELOPMENT PROGRAM
PROGRESS REPORT

August 1971

Robert B. Duffield, Laboratory Director
Robert V. Laney, Associate Laboratory Director

| | <u>Program Area</u> | <u>Lead Division</u> | <u>Division Director/ Program Manager</u> |
|------|---------------------------------|----------------------|---|
| I | EBR-II | EBR-II | M. Levenson |
| II | LMFBR Design Support | ETD | S. A. Davis |
| III | Instrumentation and Control | ETD | S. A. Davis |
| IV | Sodium Technology | CEN | R. C. Vogel/L. Burris |
| V | Fuels and Materials Development | MSD | P. G. Shewmon |
| VI | Fuel Cycle | CEN | R. C. Vogel/D. S. Webster |
| VII | Reactor Physics | AP | R. Avery |
| VIII | Reactor Safety | RAS | W. R. Simmons |
| IX | Environmental Studies | CES | E. J. Croke |

Report Coordinator: M. Weber

Issued: September 23, 1971

FOREWORD

The Reactor Development Program Progress Report describes current activities, technical progress, and technical problems in the program at Argonne National Laboratory sponsored by the USAEC Division of Reactor Development and Technology. Not all projects are reported every month, but a running account of each project is maintained in the series of reports.

The last six reports
in this series are:

| | |
|----------------|----------|
| January 1971 | ANL-7776 |
| February 1971 | ANL-7783 |
| March 1971 | ANL-7798 |
| April-May 1971 | ANL-7825 |
| June 1971 | ANL-7833 |
| July 1971 | ANL-7845 |

REACTOR DEVELOPMENT PROGRAM

Highlights of Project Activities for August 1971

EBR-II

Further experience with GLASS (Ge-Li Argon-scanning System) indicates that it is faster and more sensitive than previous methods used for monitoring fission products. It detected an increase in cover-gas activity at least $1\frac{1}{2}$ min sooner than other systems. Also, it gives data on some short-lived isotopes not previously monitored. These data give more detail on activity increases than could be obtained before.

The first two in a series of three irradiations in EBR-II of sub-assemblies containing dosimetry-foil materials have been concluded. One was at 50 kWt for 1 hr and one was at 62.5 MWt for $8\frac{1}{2}$ days.

The Graphics Display Library of the Digital Data Acquisition System has been put into operation. The library allows use of the full capability of the graphic-display unit.

LMFBR DESIGN SUPPORT

Engineering Mechanics

A computer program (DYPHLHX) has been developed for calculating dynamic plastic deformation of hexagonal shells typical of LMFBR subassembly ducts. The program is based upon an arbitrary time description of an internal load and assumes rigid plastic material behavior. Test problems, using rectangular, exponential decay and linear decay as pressure-pulse-shape descriptions, have been successfully executed.

REACTOR PHYSICS

FTR Power Distribution and Coolant-voiding Experiments

Experimental measurements directed primarily at determining the power distribution in the FTR, now simulated in the beginning-of-life (BOL) configuration of the Engineering Mockup Critical, were made in ZPR-9. For this purpose, the relative radial reaction-rate distributions of $^{239}\text{Pu}(n,f)$, $^{238}\text{U}(n,f)$ and $^{10}\text{B}(n,\alpha)$ were evaluated in this reactor.

In ZPPR, sodium-voiding measurements were made in both pin and plate environments in support of the FTR program to obtain data to test the calculations of the central void effect. A perturbation-sample method of evaluating sodium worth by integration of traverse data was developed, and results were correlated with worths in the FTR voiding configurations.

LMFBR Physics Parameter Changes Near a Boron Control Rod

A series of control-rod experiments, planned to characterize the effects of a single LMFBR-type B_4C control-rod assembly on important core-physics parameters, has begun in the high-plutonium-240 zone on ZPR-6, Assembly 7. Reactivity worths and reaction rates were determined in the vicinity of a simulated rod, with and without a 1/2-in. BeO control-rod sheath. In the region of the BeO -softened neutron spectrum, the worth of the B_4C control rod is enhanced and the relative fission rates in ^{239}Pu and ^{235}U are increased, but the fission rate in ^{238}U is essentially unchanged.

REACTOR SAFETY

Fuel-Coolant Interactions

The medium-energy power-excursion Test S7 has been performed in the piston autoclave within TREAT. This was the initial transient meltdown test that used sections of prototypal FFTF fuel and sodium at 500°C. For this test, the piston did not vent the fuel chamber at full stroke as it did in previous tests. The average energy deposited in the fuel in the S7 test, 514 cal/g UO_2 , was comparable to that in Tests S3, S5, and S6, which were conducted with ~200°C sodium. The largest pressure pulse observed in Test S7 was 430 psi, and the calculated conversion ratio from thermal into mechanical energy was 6×10^{-6} . Both these values are the lowest observed in any of the S-series tests, probably because of the 20%-lower fuel-failure threshold energy in Test S7. However, because of uncertainties about the governing mechanisms, it is not yet possible to conclude that lower pressures and conversion efficiencies will always result from pin meltdown in 500°C sodium than in 200°C sodium. Analysis of the S7 results is continuing.

TABLE OF CONTENTS

| <u>189a No.</u> | | <u>Page</u> |
|-----------------|--|-------------|
| | I. EXPERIMENTAL BREEDER REACTOR NO. II | 1.1 |
| | A. Analysis and Testing | 1.1 |
| 02-144 | 1. Reactor Analysis, Testing, and Methods Development | 1.1 |
| | a. Nuclear, Thermal, and Hydraulic Surveillance | 1.1 |
| | b. Analysis for EBR-II | 1.13 |
| 02-148 | 2. Operation with Failed Fuel | 1.14 |
| | a. Studies of Transient Fuel Performance | 1.14 |
| | b. Failure Diagnostics and Procedures | 1.15 |
| 02-151 | 3. Characterization of Irradiation Environment | 1.23 |
| | a. Radial Reaction-rate Traverses for ZPR-3 Assembly 63B | 1.23 |
| | b. Calculated Energy Spectra in ZPR-3 Assembly 63B | 1.24 |
| | c. Fission-rate Measurements in ZPR-3 Assembly 63 | 1.24 |
| | d. EBR-II Dosimetry Study | 1.27 |
| | e. Comparison of Calculated and Measured ^{235}U and ^{238}U Activations in EBR-II Run 29D | 1.27 |
| | f. Testing of Burnup Calculation System | 1.29 |
| | g. Comparison of Calculated and Measured Flow Rates in Subassembly XX02 | 1.30 |
| 02-530 | 4. Operation of Digital Data Acquisition System (DAS) | 1.31 |
| | a. Operational Support | 1.31 |
| | b. Test-data Acquisition and Support | 1.32 |
| | PUBLICATIONS | 1.33 |
| | II. LMFBR DESIGN SUPPORT | 2.1 |
| 02-097 | A. Heat Transfer and Fluid Flow | 2.1 |
| | 1. LMFBR Flow Stability Studies | 2.1 |
| | a. Preparation of Apparatus | 2.1 |
| | 2. Nonboiling Transient Heat Transfer | 2.1 |
| | a. Analysis of Heat-flux Transients | 2.1 |
| | 3. Liquid-metal Heat Transfer in Pin Bundles | 2.2 |
| | a. Analytical Investigations | 2.2 |
| | 4. Heat Transfer in Liquid-metal-heated Steam Generators | 2.4 |

TABLE OF CONTENTS

| <u>189a No.</u> | | <u>Page</u> |
|-----------------|---|-------------|
| 02-099 | B. Engineering Mechanics | 2.4 |
| | 1. Structure-fluid Dynamics | 2.4 |
| | a. Parallel Flow-induced Vibration | 2.4 |
| | 2. Components Impulse Response | 2.6 |
| | a. Dynamic Plasticity Analysis of Hexagonal Shells | 2.6 |
| | III. INSTRUMENTATION AND CONTROL | 3.1 |
| 02-024 | A. Instrumentation Development for Instrumented Subassembly | 3.1 |
| | 1. Fuel-pin and Coolant Thermocouples | 3.1 |
| 02-025 | B. FFTF Instrumentation Development | 3.2 |
| | 1. Permanent-magnet Probe-type Flowsensors | 3.2 |
| | 2. Magnetometer Probe-type Flowsensors | 3.3 |
| 02-138 | C. Neutron-detector Channel Development | 3.4 |
| | 1. Intermediate- and Wide-range Systems | 3.4 |
| | 2. High-temperature Neutron-detector Cable Technology | 3.4 |
| | 3. NITF Test Program | 3.5 |
| 02-096 | D. Advanced Technology Instrument Development | 3.5 |
| | 1. Acoustic Surveillance | 3.5 |
| | a. Development of High-temperature Detector | 3.5 |
| | b. Development of Acoustic Waveguides | 3.6 |
| | IV. SODIUM TECHNOLOGY | 4.1 |
| 02-607 | A. On-line Monitoring and Sampling for Sodium Systems | 4.1 |
| | 1. National Meter Program | 4.1 |
| | 2. Oxygen Meters | 4.1 |
| | 3. Hydrogen Meters | 4.2 |
| | 4. Carbon Meters | 4.3 |
| | 5. Meter Modules for FFTF | 4.3 |
| | 6. Detectors for Leaks in Steam Generators | 4.4 |
| | 7. Characterization of Impurity Meters and Meter Response to Impurity Species | 4.6 |

TABLE OF CONTENTS

| <u>189a No.</u> | | <u>Page</u> |
|-----------------|---|-------------|
| | V. FUELS AND MATERIALS DEVELOPMENT | 5.1 |
| | A. LMFBR Cladding and Structural Materials | 5.1 |
| 02-605 | 1. Swelling and Mechanical Behavior of Cladding Alloys | 5.1 |
| | a. Swelling of Type 304 Stainless Steel | 5.1 |
| | b. Theoretical Aspects of Void Formation | 5.2 |
| 02-092 | 2. Nondestructive Testing Research and Development | 5.2 |
| | a. Data-handling System Investigation | 5.2 |
| | B. Fuel Properties | 5.4 |
| 02-094 | 1. High-temperature Properties of Ceramic Fuels | 5.4 |
| | a. Plastic Yielding and Fracture of Mixed Oxides | 5.4 |
| | b. Crack-healing Studies in UO ₂ | 5.6 |
| 02-162 | 2. Thermochemical Properties of Reactor Fuels | 5.8 |
| | a. U-Pu-O and U-Pu-O-Na Phase Diagram and Kinetic Studies | 5.8 |
| 02-175 | 3. Physical and Chemical Studies--Molten Fuel, Cladding, and Coolant | 5.10 |
| | a. Thermal Diffusivity for Solid and Liquid Reactor Materials | 5.10 |
| | C. Fuel Elements | 5.11 |
| 02-086 | 1. Behavior of Reactor Materials | 5.11 |
| | a. Oxide-fuel Swelling Mechanisms and Models | 5.11 |
| | b. Fuel-Fission-product-Cladding Interactions | 5.12 |
| | c. Experimental Studies of Swelling Mechanisms | 5.15 |
| 02-005 | 2. Oxide Fuel Studies | 5.18 |
| | a. Fuel-swelling Studies | 5.18 |
| | b. Fuel-element Performance | 5.20 |
| | D. Core Materials Applications | 5.21 |
| none | 1. Core Design Technology | 5.21 |
| | a. Empirical Assessment of Swelling and Creep Correlations | 5.21 |
| | PUBLICATIONS | 5.24 |

TABLE OF CONTENTS

| <u>189a No.</u> | | <u>Page</u> |
|-----------------|---|-------------|
| | VI. FUEL CYCLE | 6.1 |
| 02-173 | A. Molten-metal Decladding of LMFBR Fuels | 6.1 |
| | 1. Engineering Development | 6.1 |
| | a. Zinc Decladding | 6.1 |
| | 2. Process Demonstration Experiments | 6.1 |
| | a. Irradiated-fuel Experiments | 6.1 |
| 02-159 | B. LMFBR Reprocessing--Plutonium Isolation | 6.2 |
| | 1. Plutonium Valence Adjustment | 6.2 |
| 02-158 | C. LMFBR Fuel Refabrication--Analyses and Continuous Processing | 6.4 |
| | 1. Plutonium/Uranium Ratio in Fuel | 6.5 |
| | PUBLICATION | 6.6 |
| | VII. REACTOR PHYSICS | 7.1 |
| | A. ZPR Fast Critical Experiments | 7.1 |
| 02-179 | 1. Fast Critical Facilities; Experiments and Evaluation--Illinois | 7.1 |
| | a. Clean Critical Experiments | 7.1 |
| | b. Mockup Critical Experiments | 7.5 |
| 02-181 | 2. Fast Critical Facilities; Experiments and Evaluation--Idaho | 7.8 |
| | a. Coolant-reactivity Experiments | 7.8 |
| | b. Heterogeneity Experiments | 7.12 |
| | c. Measurement of Shielding and Neutron Streaming | 7.15 |
| | B. Support of ZPR Fast Critical Experiments | 7.18 |
| 02-134 | 1. Fast Critical Experiments; Theoretical Support--Illinois | 7.18 |
| | a. Supplementary Analytical Interpretation of Integral Data | 7.18 |
| 02-010 | 2. Fast Critical Experiments; Theoretical Support--Idaho | 7.20 |
| | a. ZPR Heterogeneity Method Development | 7.20 |
| | b. Supplementary Analytical Interpretations of Integral Data | 7.22 |

TABLE OF CONTENTS

| <u>189a No.</u> | | <u>Page</u> |
|--------------------|---|-------------|
| 02-013 | 3. Fast Critical Experiments; Experimental Support--Illinois | 7.23 |
| | a. Development of Techniques for Critical Experiments | 7.23 |
| 02-011 | 4. Fast Critical Experiments; Experimental Support--Idaho | 7.24 |
| | a. Neutron Spectroscopy | 7.24 |
| | b. Development of Techniques for Critical Experiments | 7.24 |
| 02-019 | 5. Production of Materials for ZPR Experiments | 7.28 |
| | a. Special Measurement Elements | 7.28 |
| | C. Fast Reactor Analysis and Computational Methods | 7.32 |
| 02-085 | 1. Reactor Code Center | 7.32 |
| | PUBLICATIONS | 7.34 |
| | VIII. REACTOR SAFETY | 8.1 |
| 02-114 & 02-614 | A. Coolant Dynamics | 8.1 |
| | 1. Sodium Superheat | 8.1 |
| | a. Single-pin Superheat Tests with Loss of Flow and Boiling Detection | 8.1 |
| | 2. Sodium Expulsion and Reentry: Out-of-pile | 8.3 |
| 02-116 | B. Fuel-element Failure Propagation | 8.4 |
| | 1. Out-of-pile Studies | 8.4 |
| | a. Fission-gas Release Studies | 8.4 |
| | b. Failure-propagation Modes Other than due to Fission-gas Release | 8.6 |
| | 2. In-pile Studies | 8.8 |
| | a. Loop Development | 8.8 |
| | b. Preparation of Experiment Plan | 8.9 |
| 02-117 | C. Fuel Dynamics Studies in TREAT | 8.11 |
| | 1. Transient In-pile Tests of Ceramic Fuel | 8.11 |
| | a. Loss-of-flow Simulation with Seven-pin Cluster of Fresh Fuel (Test L2) | 8.11 |

TABLE OF CONTENTS

| <u>189a No.</u> | | <u>Page</u> |
|-----------------|---|-------------|
| | 2. Experiment Support | 8.12 |
| | a. Procurement of Mark-IIA Loops for In-pile Tests | 8.12 |
| | b. Procurement of Stretched Mark-IIC Loops for In-pile Tests | 8.12 |
| | 3. Analytical Support | 8.12 |
| | a. Modeling of Multiple-pin Behavior | 8.12 |
| | b. TREAT Test Analyses | 8.13 |
| | 4. Hot Laboratory Examinations | 8.16 |
| | a. Posttransient Examinations of Samples | 8.16 |
| | 5. Idaho Loop Operations | 8.16 |
| | a. Unloading of TREAT Loops in Idaho Facilities | 8.16 |
| 02-119 | D. High-temperature Physical Properties and Equation-of-state of Reactor Materials | 8.18 |
| | 1. Theoretical Extrapolation of Measured Physical Properties to Very High Temperatures | 8.18 |
| 02-164 | E. Fuel-Coolant Interactions | 8.19 |
| | 1. In-pile Simulation Tests: Pressure and Work Energy | 8.19 |
| | a. Medium-energy Power-excursion Test (S7) | 8.19 |
| | 2. Model Development | 8.22 |
| | a. Improvement of Basic Parametric Model of FCI | 8.22 |
| 02-165 | F. Postaccident Heat Removal | 8.22 |
| | 1. Core-debris Retention in Reactor Vessel | 8.22 |
| | a. Simulation Experiments to Verify Heat-transfer Model for Internal Heat Generation in Pools | 8.22 |
| 02-122 | G. TREAT Operations | 8.24 |
| | 1. Operations | 8.24 |
| | a. Neutron Radiography | 8.24 |
| 02-126 | H. Structural Dynamics and Containment | 8.24 |
| | 1. Hydrodynamic Response of Primary Containment to High-energy Excursion | 8.24 |
| | a. Insertion of Heat Transfer into Codes | 8.24 |

TABLE OF CONTENTS

189a No.

Page

| | |
|---|------|
| 2. Dynamic Response of Core Subassemblies | 8.26 |
| a. Development of Mathematical Model | 8.26 |
| b. Use of Modified NASTRAN Code to Calculate Elastic and Plastic Stresses and Deformations for the FFTF Reactor Grid-support Structure | 8.27 |

| | |
|--------------|------|
| PUBLICATIONS | 8.31 |
|--------------|------|

| | |
|---------------------------|-----|
| IX. ENVIRONMENTAL STUDIES | 9.1 |
|---------------------------|-----|

Listing of Reportable
ANL Reactor Development Program Projects
in 189a Order

| 189a No. | Reported This Month in Section | 189a Title | RDT Branch |
|-------------|--------------------------------------|---|---------------|
| 02-005 | V | Oxide Fuel Studies | RT-FM |
| 02-010 | VII | Fast Critical Experiments; Theoretical Support--Idaho | RT-PH |
| 02-011 | VII | Fast Critical Experiments; Experimental Support--Idaho | RT-PH |
| 02-012 | | Fast Critical Experiments--Industrial Appointments | RT-PH |
| 02-013 | VII | Fast Critical Experiments; Experimental Support--Illinois | RT-PH |
| 02-015 | | Planning and Evaluation of Critical Assembly Experiments | RT-PH |
| 02-019 | VII | Production of Materials for ZPR Experiments | RE-FE |
| 02-020 | | ZPR Materials Procurement | RE-FE |
| 02-024 | III | Instrumentation Development for Instrumented Subassembly | PE-IC |
| 02-025 | III | FFTF Instrumentation Development | PE-IC |
| 02-026 | | Core Component Test Loop (CCTL) | RE-CD |
| 02-045 | | Equipment--Fuel Related | RE-FH |
| 02-046 | | New Subassemblies and Experimental Support | RE-CD |
| 02-048 | | Instrumented Subassemblies | RE-CD |
| 02-061 | | Nuclear Instrument Test Facility | PE-IC |
| 02-068 | | Systems Engineering | PE-LS |
| 02-073 | | Fuel and Hardware Procurement | RE-FE |
| 02-075 | | Reactor Operations | PE-LS |
| 02-076 | | Fuels and Examination Facility Operations | RE-FE |
| 02-081 | | Reactor Physics--Applied Computational Methods | RT-PH |
| 02-082 | | Cross-section Measurements | RT-PH |
| 02-083 | | Burnup Analysis and Fission Yields for Fast Reactors | RT-PH |
| 02-084 | | Determination of Nuclear Constants | RT-PH |
| 02-085 | VII | Reactor Code Center | RT-PH |
| 02-086 | V | Behavior of Reactor Materials | RT-FM |
| 02-087 | | Chemistry of Irradiated Fuel Materials | RT-FM |
| 02-091 | | Creep, Fracture, and Fatigue Studies on Stainless Steel | RT-FM |
| 02-092 | V | Nondestructive Testing Research and Development | RT-FM |
| 02-094 | V | High-temperature Properties of Ceramic Fuels | RT-FM |
| 02-096 | III | Advanced Technology Instrument Development | RT-ST |
| 02-097 | II | Heat Transfer and Fluid Flow | RT-ST |

| 189a No. | Reported This Month in Section | 189a Title | RDT Branch |
|-------------|--------------------------------------|---|---------------|
| 02-099 | II | Engineering Mechanics | RT-ST |
| 02-112 | | Accident Analysis and Safety Evaluation | NS-FS |
| 02-114 | VIII | Coolant Dynamics | NS-FS |
| 02-116 | VIII | Fuel-element Failure Propagation | NS-FS |
| 02-117 | VIII | Fuel Dynamics Studies in TREAT | NS-FS |
| 02-119 | VIII | High-temperature Physical Properties and Equation-of-state of Reactor Materials | NS-FS |
| 02-122 | VIII | TREAT Operations | NS-FS |
| 02-126 | VIII | Structural Dynamics and Containment | NS-FS |
| 02-131 | | EBR-II In-core Instrument Test Facility (INCOT) | PE-IC |
| 02-133 | | NDT Characterization of Cladding Alloys | RT-FM |
| 02-134 | VII | Fast Critical Experiments; Theoretical Support--Illinois | RT-PH |
| 02-137 | | Nonmetallic Impurity Interactions in Sodium-Metal Systems | RT-CC |
| 02-138 | III | Neutron-detector Channel Development | PE-IC |
| 02-144 | I | Reactor Analysis, Testing, and Methods Development | RE-CD |
| 02-145 | | Metal Driver Fuel Development and Application | RE-FE |
| 02-148 | I | Operation with Failed Fuel | RE-CD |
| 02-150 | | Hot Fuel Examination Facilities | PE-FH |
| 02-151 | I | Characterization of Irradiation Environment | RE-CD |
| 02-157 | | LMFBR Fuel Materials Preparation--U/Pu Nitrates to Oxides | RT-FR |
| 02-158 | VI | LMFBR Fuel Refabrication--Analyses and Continuous Processing | RT-FR |
| 02-159 | VI | LMFBR Reprocessing--Plutonium Isolation | RT-FR |
| 02-162 | V | Thermochemical Properties of Reactor Fuels | RT-FR |
| 02-164 | VIII | Fuel-Coolant Interactions | NS-FS |
| 02-165 | VIII | Postaccident Heat Removal | NS-FS |
| 02-166 | | Thermal-plume Dispersion Studies | PA |
| 02-173 | VI | Molten-metal Decladding of LMFBR Fuels | RT-FR |
| 02-175 | V | Physical and Chemical Studies--Molten Fuel, Cladding, and Coolant | RT-FR |
| 02-177 | | Activation Studies of Fast-neutron Spectra | RT-FM |
| 02-178 | | ZPR-6 and -9 Operations and Maintenance | RT-PH |
| 02-179 | VII | Fast Critical Facilities; Experiments and Evaluation--Illinois | RT-PH |
| 02-180 | | ZPPR Operations and Maintenance | RT-PH |
| 02-181 | VII | Fast Critical Facilities; Experiments and Evaluation--Idaho | RT-PH |
| 02-185 | | Lake Circulation Model Development | PA |

| 189a No. | Reported This Month in Section | 189a Title | RDT Branch |
|-------------|--------------------------------------|---|---------------|
| 02-194 | | Surveillance and Failure Evaluation of Experimental Fuel Irradiations | RT-FM |
| 02-195 | | Instrumentation System Engineering | PE-IC |
| 02-197 | | TREAT Improvements | PM-EB |
| 02-204 | | Reactor Plant Services for Experimenters | RT-FM |
| 02-205 | | Nondestructive Testing and Services to Experimenters | RT-FM |
| 02-206 | | Operations in Support of Experimental Irradiations | RT-FM |
| 02-210 | | Great Lakes Power Plant Siting Study | PA |
| 02-213 | | Sodium Effects on Mechanical Behavior of Stainless Steel | RT-CC |
| 02-528 | | Plant Dynamics and Control Analysis | PE-IC |
| 02-530 | I | Operation of Digital Data Acquisition System (DAS) | PE-IC |
| 02-593 | | Sodium Impurity Analysis and Control | RT-CC |
| 02-595 | | Radioactivity Monitoring in LMFBF Systems | RT-CC |
| 02-605 | V | Swelling and Mechanical Behavior of Cladding Alloys | RT-FM |
| 02-606 | | Theoretical Fast-reactor Physics | RT-PH |
| 02-607 | IV | On-line Monitoring and Sampling for Sodium Systems | RT-CC |
| 02-609 | | Coolant Chemistry | RT-CC |
| 02-610 | | Materials-Coolant Compatibility | RT-CC |
| 02-611 | | GCFR Fuel-element Development | RT-FM |
| 02-613 | | GCFR Safety-related Performance Aspects of Fuel and the Core | NS-AE |
| 02-614 | VIII | Coolant Dynamics | NS-FS |
| 02-615 | | Postaccident Heat Removal | NS-FS |
| 02-616 | | Fuel Inherent Safety | NS-FS |
| 02-617 | | Determination of Experiment In-reactor Condition | RE-CD |
| 02-618 | | Disposal of Krypton and Tritium | RT-FR |

I. EXPERIMENTAL BREEDER REACTOR NO. II

A. Analysis and Testing

1. Reactor Analysis, Testing, and Methods Development (02-144)

a. Nuclear, Thermal, and Hydraulic Surveillance (Last reported: ANL-7833, p. 1.1)

(1) Self-powered Ion Chambers (J. R. Karvinen and C. C. Price).

A self-powered ion chamber (see ANL-7705, p. 100) requires no external power source and, consequently, no high-voltage leads. Such devices are small and rugged and can withstand the environment of LMFBR systems. They have been successfully used in thermal reactors.* However, the only known experience with them in a fast breeder system is that acquired at EBR-II in instrumented subassemblies XX01 and XX03.

The self-powered ion chamber resembles a conventional ion chamber in many respects. Principal components of a typical chamber (see Fig. I.1) are: a central electron-emitting material attached to a conducting lead, mineral insulation, and a collector, which usually is the external protective sheath. A compensating lead of the same material, size, and geometry as the central conductor is used to compensate for the signal generated in the conductor lead.

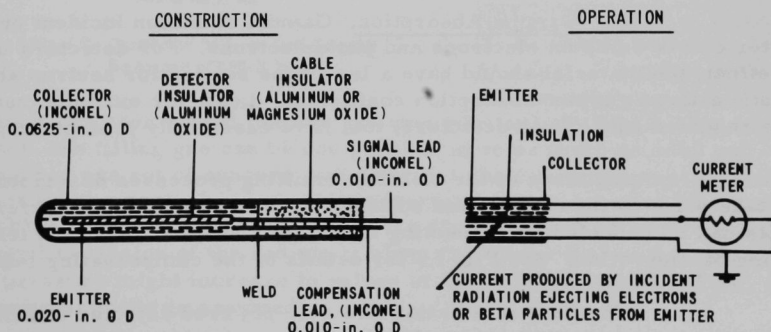


Fig. I.1. Self-powered Detector

These ion chambers operate on the following principle: Radiation incident on the emitter results in energetic electrons that penetrate the insulation and reach the collector (see Fig. I.1). The resulting excess of charge on the collector causes a potential difference between the

*A. Goodings, Technical Survey No. 1, In-core Instrumentation: In-core Neutron Flux Detectors for Power Reactors, Nucl. Eng. International, pp. 599-603 (July-Aug 1970).

emitter and the collector. If the central conductor is connected to the outer sheath through a resistor, the rate of charge production is directly proportional to the rate of absorption of radiation by the emitter.

There are three principal mechanisms for conversion of incident radiation to energetic electrons.

(a) Neutron Capture followed by Beta Decay. Neutron capture in the emitter results in a radioisotope, e.g., ^{103}Rh , that decays by beta-particle emission. The capture product is ^{104}Rh , which emits 2.4-MeV beta particles with a 42-sec half-life.

(b) Neutron-capture Gamma Conversion. Neutron capture in the emitter results in prompt-capture gamma radiation that is partially absorbed in the emitter itself. As a result of this absorption, Compton electrons and photoelectrons are produced. For emitters using this effect, the cross-section for neutron absorption should be large, but the product nuclide should be free of interfering beta emissions. In practice, a material with a very long-lived beta emitter can be used, because the buildup of the extraneous beta signal is relatively slow. An example of such material is ^{59}Co , which has a beta-emitting half-life of 5.3 years. However, cascade gamma radiation, emitted within 10^{-14} sec after neutron capture, ejects Compton electrons and photoelectrons. Thus the response of the detector, which is a function of the electron collection, is prompt.

(c) Gamma Absorption. Gamma radiation incident on the emitter ejects Compton electrons and photoelectrons. For detectors using this effect, the material should have a low cross section for neutron absorption and a large gamma-absorption coefficient. Lead, for example, satisfies these requirements. Such detectors, too, have essentially prompt responses.

All three of the electron-emitting processes described above also take place in the emitter and collector leads. These lead-interference effects can be canceled by connecting the emitter and compensation leads in bucking configuration. See Fig. I.1 for details of the compensating lead.

The first irradiation of a self-powered detector in EBR-II was in instrumented subassembly XX01. The results from irradiation studies showed that the response was nearly linear with power, with a slight tendency for decreasing efficiency at higher powers.

The results of these tests were so encouraging that plans were made to incorporate additional chambers in instrumented subassembly XX03, with emphasis on compensation and shorter response times. (The detector in XX01 was not compensated.) Two detectors were selected and installed. One had a rhodium emitter, 20 cm (7.87 in.) long and 0.020 in. in diameter, and the other a cobalt emitter 35 cm (13.78 in.) long and 0.020 in. in diameter. Both chambers were compensated.

Both detectors are being irradiated. The results obtained during a typical reactor startup, Run 50F, are presented in Fig. I.2. For comparison, the response of a conventional compensated ion chamber in the J-4 thimble is also given. In general, the data indicate that the responses of both self-powered ion chambers and the conventional compensated ion chamber are reasonably linear with power.

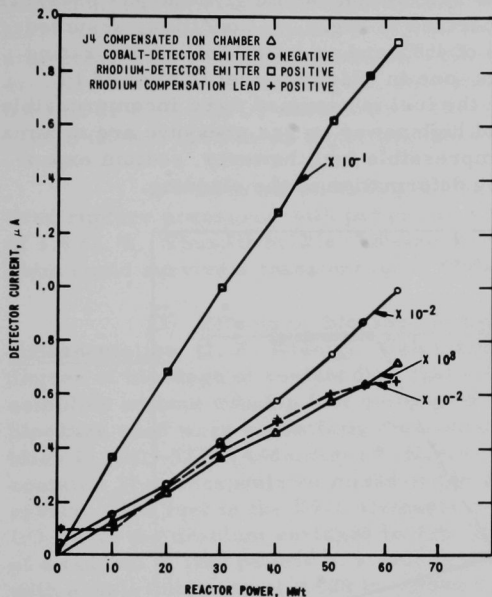


Fig. I.2. Currents of Self-powered Detector for Startup of EBR-II Run 50F

Figure I.2 also shows the signal of the compensation lead for the rhodium detector. The signal from the compensation lead of this cobalt detector is not shown because of malfunction of the detector; the compensation lead appears to have developed a short to the emitter.

(2) Effects of Over-power Conditions on Irradiated EBR-II Driver-fuel Elements (J. F. Koenig and C. C. Ford).

At 1.5 at. % burnup, most of the sodium bond in a Mark-IA fuel element has been forced into the gas space by fuel swelling. As a consequence, the filling gas can be compressed up to as much as 1400 psi. Such pressures are not of concern under normal steady-state operating conditions. If, however, a control rod should inadvertently be inserted at 5 in./min, the resulting power increase would heat the displaced sodium and, because the thermal expansion of the sodium is about five times that of the cladding, the gas pressure might increase to values of the order of 3000-4000 psi, if fuel incompressibility is assumed.

To assess the effects of such a transient on irradiated Mark-IA driver-fuel elements, calculations, based on the BEMOD code,* were carried out. Although BEMOD is a steady-state program, the short time constant of the fuel (about 0.3 sec) permits near-equilibrium fuel temperatures during the relatively slow transient initiated by continuous control-rod insertion. Output from the program consists of pressure-stress information.

*V. Z. Jankus, BEMOD, A Code for the Lifetime of Metallic Fuel Elements, ANL-7586 (July 1969).

The expansion of displaced sodium under transient conditions can be accommodated by either straining the cladding or compressing the fuel. The results of a BEMOD calculation, which give the gas pressure as a function of power, are summarized in Fig. 1.3. Conditions assumed in the calculations were a burnup of 1.8% and an initial full-power rating of 6 kW/ft. Two cases are shown: one in which the fuel is allowed to compress, and the other in which the fuel is assumed to be incompressible. As the data indicate, the effects of high power on gas pressure are minimal for compressible fuel. For incompressible fuel, however, sodium expansion can be accommodated only by deformation of the cladding.

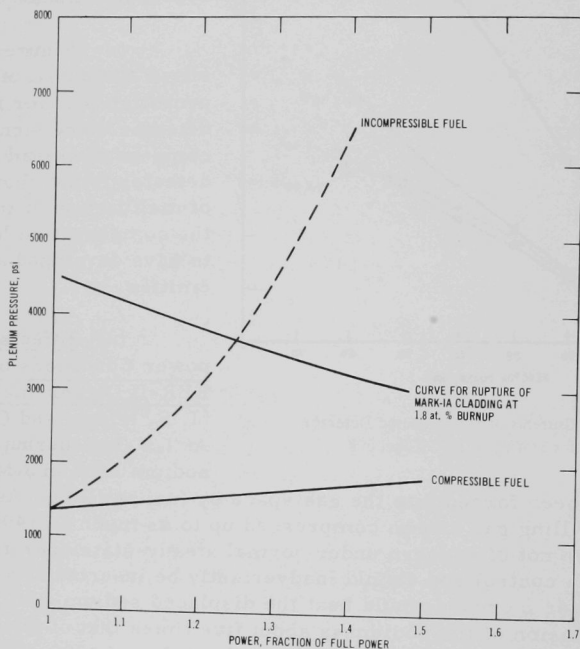


Fig. 1.3. Plenum Pressure for a Mark-IA Fuel Element at 1.8 at. % Burnup during an Overpower Transient

Recent measurements of change in volume as a function of temperature and pressure show that fuel is essentially incompressible under the pressure conditions associated with the transient. Therefore, sodium expansion can be accommodated only by cladding strain. In the BEMOD calculation, it was assumed that only elastic deformation takes place; i.e., plastic strain was not allowed. Once the yield strength is reached, however, plastic strain can occur, and it could increase the effective volume of the element. This condition would tend to limit the increase in gas pressure.

Irradiation damage can reduce the ductility of the cladding from approximately 40% for unirradiated material to the essentially brittle condition that exists under conditions of high fluence. Cladding from Mark-IA elements irradiated to 1.8 at. % has been ruptured, and the cladding strain has been measured (see ANL-7825, p. 1.30). For cladding samples taken in the fuel region, only small diametral increases (about 0.5 mil or 0.3% $\Delta D/D$) were noted. Therefore, the elastic model, with brittle failure used as an upper pressure limit, is not unduly conservative.

Also shown in Fig. I.3 is a smooth curve that relates measured rupture pressures with power for a Mark-IA fuel element with a burnup of 1.8 at. %. Thus, if brittle cladding failure is assumed, a Mark-IA element could survive a transient up to 125% of nominal full power.

(3) Effects of Blockage of Coolant Flow in Oxide-fueled Subassemblies (J. F. Koenig). Calculations were made to determine the degree of blockage of coolant flow that could exist in oxide-fueled subassemblies without causing fuel melting or sodium boiling. The models for blockage used were essentially those described for driver-fuel subassemblies in ANL-5719 (Addendum).^{*} Experimental subassembly X040, which contains 37 unencapsulated mixed-oxide elements, was used as the reference. The fuel in the X040 elements is a mixture of 20% PuO_2 and 80% UO_2 , with the uranium enriched to 93% in ^{235}U . The fuel consists essentially of a column of fuel pellets in 0.290-in.-OD Type 304 stainless steel cladding, with a wall thickness of 0.020 in. Power generation in a typical X040 element was assumed to be 16 kW/ft.

Also assumed was that fuel at uniform density had swelled to fill the volume circumscribed by the inner edge of the cladding. The value used for the contact heat-transfer coefficient between fuel and cladding was 1500 Btu/hr-ft²-°F. Pellet densities for X040 elements range from 86 to 92% of theoretical density (TD), and smear densities range from 82 to 88% TD. Values used for the thermal conductivity of the fuel were derived from the expression

$$k = 0.0110 + \frac{1}{T[0.4848 - 0.4465(\text{TD})]},$$

where k is in W/cm-°C, T is in °C, and TD is the fraction of theoretical density.

It was assumed that fuel restructuring had occurred and that uranium-plutonium oxide tends to densify at high temperatures in the presence of a temperature gradient. Columnar grains with a density of 99% TD form above 3900°F. Equiaxed grains with a density of 97% TD form between

^{*}L. J. Koch, W. B. Loewenstein, and H. O. Monson, Addendum to Hazard Summary Report: Experimental Breeder Reactor-II (EBR-II), ANL-5719 (Addendum), p. 233 (June 1962).

3000 and 3900°F. Below 3000°F, the oxide remains at its fabricated density. A void of a volume that corresponds to the density changes in the fuel forms at the center of the fuel. Densification of the fuel has been assumed in developing the model used in the calculations. For the reference oxide fuel element used in the analysis, three cases, similar to those of ANL-5719 (Addendum), p. 23 were studied for fuels of 92 and 82% TD. The radii of the different grain regions are:

| Density, % of Theoretical: | 92 | 82 |
|----------------------------|--------|--------|
| Temperature, °F | | |
| Maximum | 4580 | 4360 |
| Surface | 1530 | 1530 |
| Radii, in. | | |
| Void | 0.0219 | 0.0389 |
| Columnar grain | 0.0658 | 0.0710 |
| Equiaxed grain | 0.0918 | 0.0966 |
| Original density | 0.125 | 0.125 |

Case 1: For the Case-1 study similar to that of ANL-5719 (Addendum), oxide fuel was assumed to accumulate in the coolant triffute between the fuel elements. The fuel, assumed to be of the density of the fabricated pellets, generates heat at the same rate as oxide fuel within the cladding. One-half of a symmetrical fuel element in the triffute was considered as subdivided for two-dimensional analysis of heat transfer. The fuel deposit was assumed to be long enough to permit neglect of axial heat transfer. The thickness of the symmetrical oxide fuel deposited in the triffute varied from 0.055 in. at the center of the deposit to 0.028 in. at the edge. Under these conditions, heat generated in the deposit must be transferred circumferentially through the fuel deposit, cladding, or fuel to the sodium coolant 30° away at the edge of the deposit.

Figure I.4 shows the radial temperature distributions at the center of the deposit and opposite the deposit, obtained from the THTB program* for 92%-TD oxide fuel elements. The maximum cladding temperature at the center of the deposit is 2100°F for 92%-TD and 2170°F for 82%-TD fuel. Both temperatures are below the melting point (about 2600°F) of Type 304 stainless steel. At 2200°F, the short-term tensile strength of unirradiated stainless steel is about 2000 psi. This strength would contain an internal pressure of about 300 psi. The fuel-element pressure, originating from accumulation of rare-gas fission products, can easily exceed this value; therefore, the cladding may fail.

Part of the fuel at the center of the element would be above the melting temperature (>5000°F). For the model, it was assumed that the

*G. L. Stephens and D. J. Campbell, Program THTB for Analysis of General Transient Heat Transfer Systems, R60FPD647, General Electric Co. (Apr 1961).

central void would retain its original dimensions. In reality, however, the molten fuel might run down the void and solidify on the cooler fuel or in the bottom of the void. For 82%-TD fuel, the void radius would vary from 0.039 in. at the axial flux peak to 0.026 in. at the bottom of the fuel rod. If the voids were filled, the fuel volume would increase from 11% at the flux peak to 4% at the bottom of the fuel. The corresponding values for the 92%-TD fuel are an 0.022-in. void at the flux peak and an 0.0099-in. void at the bottom. The corresponding volumes of the voids are 3 and 0.6% of the fuel volume. Such fuel movement, if it occurs, would cause reactivity changes and increases in the axial heat-transfer rate.

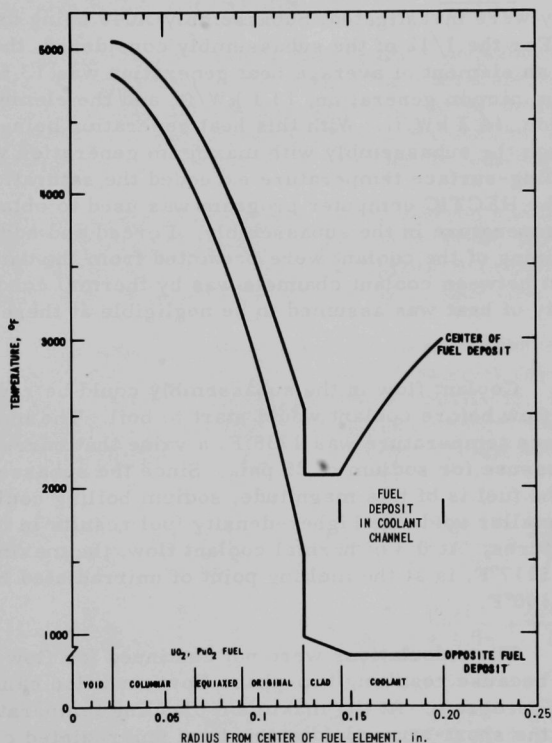


Fig. 1.4. Radial Temperature Distribution at Flux Peak for Case-1 Coolant-blockage Condition. Element of 92% TD operating at 16 kW/ft transferring heat to 850°F coolant. Coolant triflute filled with fuel. ANL Neg. No. 103-P5651 Rev. 1.

Case 2: For Case-2 conditions, the fuel element clad with stainless steel (0.290-in. OD, with a wall thickness of 0.020 in.) was assumed to be covered with oxide fuel of a thickness equal to that of a spacer wire, 0.056 in. The fuel deposit, which generates heat, was assumed to be at its

original density. The angle of the cladding surface that was covered with fuel was assumed to increase until the cladding reached its melting temperature. No axial heat conduction was considered.

The cladding temperature would exceed the melting point when approximately 100° of the element surface is covered with fuel. The maximum oxide temperature is higher for the lower-density fuel because of its lower thermal conductivity. The maximum cladding temperature is also higher for this fuel.

Case 3: The consequences of reduced coolant flow rate in a subassembly were investigated, Subassembly X040 being used as an illustration. For the 1/12 of the subassembly considered, the average heat generation in an element of average heat generation was 13.5 kW/ft; the element with minimum generation, 13.1 kW/ft; and the element with maximum generation, 14.2 kW/ft. With this heat generation being maintained, the flow through the subassembly with maximum generation was reduced until the cladding-surface temperature exceeded the saturation temperature of sodium. The HECTIC computer program was used to obtain distribution of flow and temperature in the subassembly. Forced and eddy-diffusivity-momentum mixing of the coolant were predicted from the data of Bump.* Heat transport between coolant channels was by thermal conduction. The eddy diffusivity of heat was assumed to be negligible at these low Peclet numbers.

Coolant flow in the subassembly could be reduced to 0.3 of its normal flow before coolant would start to boil. The maximum cladding-surface temperature was 1735°F, a value that corresponds to a saturation pressure for sodium of 25 psia. Since the subassembly pressure at the top of the fuel is of this magnitude, sodium boiling could occur. Because of its smaller void, the higher-density fuel results in higher maximum temperatures. At 0.3 of normal coolant flow, the maximum fuel temperature, 5117°F, is at the melting point of unirradiated hypostoichometric fuel, 5100°F.

The calculations were not continued for flow rates below 0.3 of normal because resulting two-phase flow condition cannot be described by the HECTIC program. At the maximum cladding temperatures associated with 0.3 flow, the short-term yield strength of unirradiated cladding would be about 6000 psi; it would be 18,000 psi at 1000°F (full-flow conditions). If a 6000-psi yield strength is used, the rupture pressure would be about 900 psi. Because irradiation tends to increase the yield strength, the actual rupture pressure would be somewhat higher.

*T. R. Bump, Coolant Mixing in Fuel Subassemblies, Trans. Am. Nucl. Soc. 9(2), 571 (Nov 1966).

The effect of coolant flow on temperature mixing in the sub-assembly, as calculated by HECTIC, was negligible for the central element. The effect was more pronounced, however, for the overcooled channels adjacent to the outside channel. At 0.3 of normal flow, the temperature of the exit coolant adjacent to the central element was calculated to be 1692°F; that in an outside channel was at 1178°F. If no momentum mixing, conduction around the cladding circumference, or interchannel thermal conduction were allowed, the exit temperature of the central-element coolant would be 1694°F, whereas the exit temperature of coolant adjacent to an outside channel would be 1114°F. The calculated mixing reduced the coolant temperature of the central element by only 2°F.

In summary, oxide subassemblies probably could withstand a blockage of coolant flow that would reduce the subassembly flow to 0.3 of normal. Under this condition, sodium boiling would occur next to the hottest element. Further flow reduction would allow additional boiling to occur. The accompanying increase in pressure drop would reduce the flow further.

(4) Rod-drop Experiments (H. A. Larson and I. A. Engen). During Run 49F, rod-drop experiments were done at 58, 50, and 40 MWt, with calibration data taken at 500 kWt. Calibration data indicate a rod worth of about 0.020\$, it was 0.022\$ for Run 49C. (See ANL-7825, p. 1.81.)

Average time-dependent reactivity for three rod drops at each power level is subtracted from the time-dependent reactivity determined at 500 kWt to obtain a resulting feedback reactivity. Modeling is done with the feedback reactivity as described in ANL-7686.* The resulting models for the feedback transfer function for 58, 50, and 40 MWt are, respectively:

$$-H(s) = \frac{0.058}{1 + 0.2s} + \frac{0.098}{1 + 0.4s} - \frac{0.02}{1 + 2.0s} + \frac{0.05}{1 + 4.0s} + \frac{0.011e^{-910s}}{1 + 3.0s}, \quad (1)$$

$$-H(s) = \frac{0.055}{1 + 0.2s} + \frac{0.090}{1 + 0.4s} - \frac{0.02}{1 + 2.0s} + \frac{0.01}{1 + 4.0s} + \frac{0.005e^{-7.5s}}{1 + 3.0s}, \quad (2)$$

and

$$-H(s) = \frac{0.040}{1 + 0.2s} + \frac{0.080}{1 + 0.4s} - \frac{0.03}{1 + 2.0s} + \frac{0.01}{1 + 4.0s} + \frac{0.005e^{-7.5s}}{1 + 3.0s}. \quad (3)$$

The units of $H(s)$ are the same as those in ANL-7686.

(5) Rod Oscillator Experiments (H. A. Larson, I. A. Engen, and M. R. Tuck). Rotary-rod oscillator tests were done for Run 49F at 58, 50, and 40 MWt. Reactor transfer functions were calculated by using

*I. A. Engen, A New Technique for Investigating Feedback and Stability of a Nuclear Reactor, ANL-7686 (June 1970).

the analysis method described in ANL-7476* and in ANL-7825 (p. 1.82). The magnitude and phase of these data are plotted in Fig. I.5 for frequencies from 0.007 to 8 Hz.

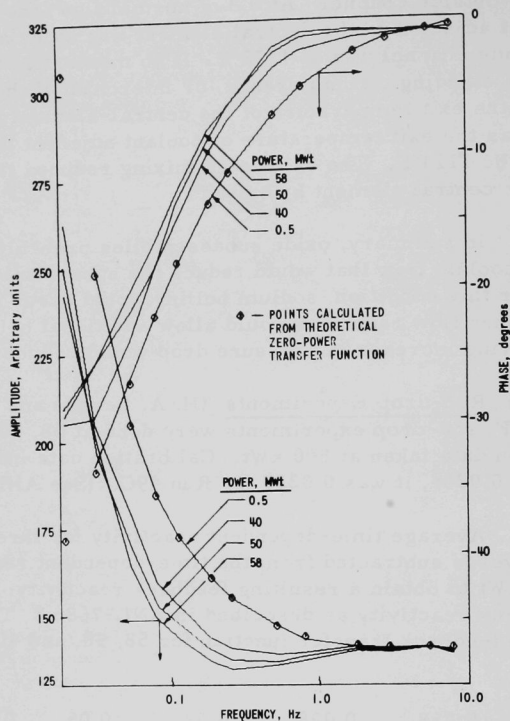


Fig. I.5. Magnitude and Phase of EBR-II Transfer Function, Run 49F, Normalized to Theoretical Zero-power Transfer Function at 5.5 Hz

The measured transfer-function phase at zero power did not exactly match the theoretical phase; a normalization procedure suggested by Hyndman (in ANL-7825) was used to obtain a correction factor, which was subsequently applied to the measured transfer-function phase at power. The frequency-dependent correction, which is given by

$$\phi_c = \phi_0 + \tan^{-1} \frac{f}{f_0},$$

*R. W. Hyndman and R. B. Nicholson, The EBR-II Feedback Function, ANL-7476 (July 1968).

when applied to the measured phase, minimized the squared difference between measured and calculated zero-power phase when $\phi_0 = -1.11$ and $f_0 = 315$. No corrections were made to the magnitudes of the transfer-function data.

To assess the reliability of the data, the feedback transfer function was determined from the oscillator data taken at 58 MWt. Designating these data as $G(s)$ and the zero-power data as $G_0(s)$, the feedback transfer function, $H_0(s)$, is determined from

$$G(s) = \frac{G_0(s)}{1 + G_0(s)H_0(s)}.$$

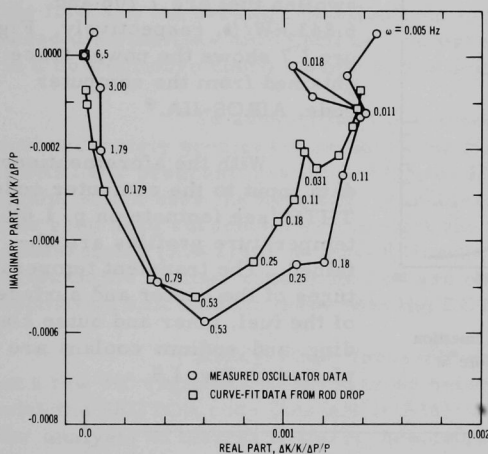


Fig. I.6. Real Part of $[H(j\omega)]$ vs Imaginary Part for Run 49F at 58 MWt

Figure I.6 shows a plot of $H_0(j\omega)$ along with that calculated from the rod-drop experiment and shown in Eq. 3 of the feedback models. The feedback functions, in units of the inverse of the transfer function, are plotted as a function of increasing frequency, ω . Normalization does not exactly match between the curves, but good qualitative comparison can be made.

Figure I.6 shows that the rod-drop and oscillator methods are qualitatively equivalent; both methods predict essentially the same transfer function. Efforts are being made to explain quantitative differences to place the

two methods on as near a one-to-one basis as possible. For example, a natural mechanical resonance in the oscillator rod near 9 Hz explains the high-frequency correction to the measured phase that is required.

(6) Temperature Distributions in Mark-II Fuel during the Transient Induced by Insertion of a Control Rod into an EBR-II Core at Full-power Operation (R. K. Lo and B. R. Sehgal). Calculations were made to determine the transient temperature distribution in fresh and swollen Mark-II fuel resulting from insertion of a control rod into an EBR-II core during full-power operation. The size of the fresh fuel element considered is: fuel, 14.22 in. long and 0.130 in. diameter; Type 304 stainless steel cladding, 0.174-in. OD and 0.150-in. ID; and sodium bond, 0.010 in. thick. According to surveillance studies on Mark-II fuel

(see ANL-7737, p. 90), at a burnup of about 3 at. %, the fuel swelled radially to come in contact with the cladding over the whole length and swelled axially to the restrainer, which is 1 in. above the top of the fresh fuel. The fuel

element is assumed to be in Row 5. The flow rate is 0.69 gpm/element. The physical properties of fresh Mark-II fuel were assumed to be the same as those of Mark-I fuel. For the swollen fuel, the reduction in density and thermal conductivity was accounted for. The heat-generation rates of the fresh fuel and the swollen fuel are 7.706 and 6.843 kW/ft, respectively. Figure I.7 shows the power trace obtained from the computer code, AIROS-IIA.*

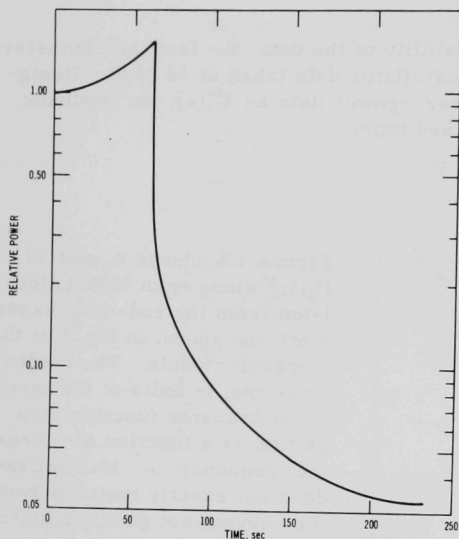


Fig. I.7. Increase in Power after Accidental Insertion of a Control Rod into an EBR-II Core at Normal Operating Power

With the aforementioned data input to the computer code THTB (see footnote on p. 1.6), temperature profiles are obtained. The transient temperatures of the center and surface of the fuel, inner and outer cladding, and sodium coolant are plotted in Fig. I.8.

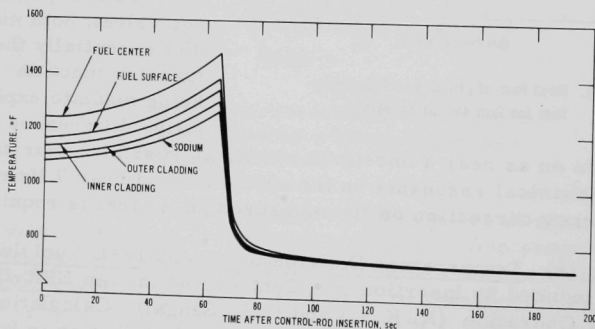


Fig. I.8. Transient Temperatures at Outlet of Hottest Mark-II Fuel Element during Insertion of a Control Rod into an EBR-II Core at Full Power

*A. V. Campise, ANL, private communication (Jan 1971).

At 70 sec after inception of the transient, the peak fuel temperature of the fresh fuel reaches 1470°F; the peak temperature of fuel with 3 at. % burnup reaches 1440°F. For neither fuel is the eutectic temperature reached.

b. Analysis for EBR-II

(1) Prediction and Measurement of Reactivity Effects due to Thermal Bowing of Subassemblies in an EBR-II Core with a Depleted-uranium Blanket (A. Gopalakrishnan and D. Mohr). The reactivity feedback due to thermal bowing of the subassemblies in EBR-II is a function of the core loading, reactor power level, and distribution of coolant flow. Sophisticated thermal-hydraulic codes have recently been developed to calculate the flow and temperature distributions in the core and blanket regions; these distributions have been used to estimate the thermal bowing effects in a current core configuration with a depleted-uranium blanket.

To account for the heterogeneity in EBR-II core loadings and accurately predict the coolant flow distribution in the reactor, the EBRFLOW program (see ANL-7705, p. 92) has been developed. This program, which uses the hydraulic characteristics of each reactor subassembly, has been used successfully to predict the flow rate through an instrumented subassembly (XX02) for several different core loadings. Heat-generation rates in the various subassemblies are obtained from neutronics and gamma-deposition calculations made with the DOT transport-theory code.*

Steady-state, three-dimensional temperature distributions in a few 30° segments of the reactor between Rows 5 and 12 were obtained with the SECTOR code (see ANL-7825), which was specifically developed for analysis of thermally interconnected subassemblies. The resulting differences in temperature between opposite faces of the hexagonal cans were input to the BOW-V program** for calculating the restrained thermal deflections of the subassemblies and the consequent feedback reactivity.

There is now no direct means to measure the subassembly deflections or the thermal-bowing component of the feedback reactivity. The only experimental information on bowing reactivity is that deduced from the measurement of the total power-reactivity decrement (PRD) of the core. Analytical models,[†] must be used to calculate the reactivity effects due to causes other than thermal bowing, and these effects are then subtracted from the measured total PRD to obtain the thermal-bowing component

*F. R. Mynatt, DOT, A Two-dimensional Discrete-ordinates Transport Code, K-1694, Radiation Shielding Information Center, ORNL. See also ANL-7513, p. 50.

**D. A. Kucera and D. Mohr, BOW-V, A CDC-3600 Program to Calculate the Equilibrium Configurations of a Thermally Bowed Reactor Core, ANL/EBR-014 (Jan 1970).

†J. K. Long, Analysis of the Static Power Coefficient of EBR-II with Reduced Coolant Flow, Nucl. Appl. 6(2), 116 (Feb 1969); J. K. Long, The Effect of a Metallurgical Phase Change in Fuel on the Power Coefficient of EBR-II, Nucl. Technol. 10(1), 17 (Jan 1971).

of feedback. Figure I.9 compares the bowing reactivity component calculated for Run 46A by using the physics, thermal-hydraulic, and bowing analyses mentioned earlier, with its value deduced from PRD measurements. The probable errors in the measured PRD and in the calculated reactivity components (other than that due to bowing) are indicated in the figure. A statistical combination of these errors result in the error band shown on the deduced bowing reactivity component.

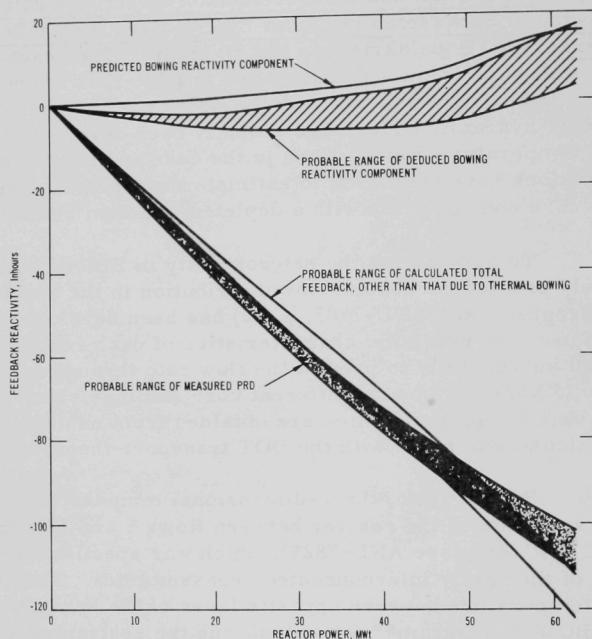


Fig. I.9. Calculated and Measured Reactivity Feedback for Run 46A

Results show that the analytical prediction of the positive reactivity effects due to thermal bowing is slightly higher than the range indicated by PRD data. However, the predicted rate of change of bowing reactivity with power compares well with that of the deduced component.

2. Operation with Failed Fuel (02-148)

a. Studies of Transient Fuel Performance (Last reported: ANL-7705, p. 110)

(1) Adaptation of a Linear Variable Differential Transformer (LVDT) for Fuel-expansion Measurements in TREAT (R. M. Fryer and J. R. Karvinen). The effects of fuel-cladding contact on the overall expansion characteristics of driver-fuel elements are only partially

understood. To assess the importance of these effects, attempts are being made to measure the axial motion of the fuel column when driver-fuel elements are subjected to transient power conditions in TREAT. The technique, as originally implemented, used an eddy-current proximeter probe as the motion-sensing device. Actuating the probe was a steel rod that rested on top of the fuel column of the test specimen (see ANL-7705, p. 110).

To test the operation of the device under transient conditions, a transient test was conducted in which the fuel pin was replaced by a solid stainless steel rod. The results indicated no discernible change in the transducer signal before, during, or after the transient. From this information, effects of the transient on the test section, transducer, and electrical leads were concluded to be negligible.

In the next test, an unirradiated Mark-IA element was used as a test specimen. Three separate transients were carried out; the transducer indicated fuel motion in all of them. An analysis of the data showed that the motion was higher by a factor of about three than could be explained on the basis of the power-generation schedule and accepted values of the linear-expansion coefficient. Because no explanation was found, the test will be repeated, with a linear variable differential transformer (LVDT) used as the motion-sensing device.

LVDT's were originally considered, but they were rejected on the basis that the eddy-current proximeter indicated better performance at the high temperatures (600-700°F) expected in the test loop. Since then, actual temperature measurements have shown that transducer temperatures never exceed 400°F under test conditions. Because conventional LVDT's can operate satisfactorily up to 500°F, their use in future tests appears promising. The LVDT's also have a greater measurement span and are less temperature-sensitive than the magnetic devices used in the earlier tests.

A supply of LVDT's and the exciter-demodulator unit needed for their use have been purchased. Preliminary tests carried out with the devices indicate that they are promising. A furnace suitable for temperature-calibration studies has been fabricated, and the mechanical changes needed to mate the LVDT with the Mark-I loop section have been made. The equipment is being bench-tested. When these tests are completed, another transient test, again with an unirradiated driver-fuel element, will be made in TREAT.

b. Failure Diagnostics and Procedures (Last reported: ANL-7833, p. 1.19)

(1) Thermal Analysis of the Use of the Failed-fuel Transfer System for Identifying Leaking Fuel Elements (R. A. Cushman). Use of the Failed-fuel Transfer System (FFTS)* to detect failed fuel elements in an

*C. J. Divona and E. Hutter, Preliminary System Design Description of the EBR-II Failed-fuel Transfer System, ANL/EBR-024 (July 1970).

experimental subassembly has been proposed. The principle of the procedure is based on the following: When a subassembly is in the raised position during fuel handling (storage position II), transfer of decay heat to the environment is impeded. The resulting temperature increase could increase the plenum-gas pressure enough to cause release of additional gas. If this release should happen, analysis of the gas in the reservoir above the FFTS could lead to a positive identification of a suspect element. To establish guidelines for operating the facility in detecting leaks, heat-transfer calculations were carried out to evaluate temperatures when subassemblies are in the raised position.

Because of the variety of experimental subassemblies for which the procedure could be used, a hypothetical subassembly that would give results applicable to all types was chosen. For a given thermal conductivity of a heat-generating material operating at a given linear heat rate, the temperature drop across the radius is independent of the radius; therefore the entire volume of the hexagonal can over the 14.2-in. core length was assumed to contain power-generating material. The thermal conductivity of this material was based on its being 50 vol % sodium, 10 vol % stainless steel, and 40 vol % (U-Pu)O₂; a conductivity of 20 Btu/hr-ft-°F was used. The volume 3 in. above and below the fuel portion was assumed to have a conductivity of 25 Btu/hr-ft-°F, and an additional 3 in. below the fuel was assumed to be sodium. The top and bottom of this 23.2-in.-high volume (3+14.2+3+3) were assumed to be surfaces with zero heat transfer.

The experimental subassembly (a hexagonal can, converted to a 2.406-in.-dia cylinder) was centered in the dipper of the FFTS, a 4-in. schedule-10 stainless steel pipe, and the dipper was centered in the raised position in the X-nozzle sleeve. With the dipper in this position, only the lower 5½ in. of the core region of a subassembly is below the sodium-argon interface in the primary tank. For conservatism, only the bottom 5 in. was assumed to be below the sodium level. Figure I.10 shows the model used in the THTB calculations. Film coefficients, based on natural-convection heat transfer (plus radiation in the argon cover gas) of 180 and 15 Btu/hr-ft²-°F respectively, were used for the outside of the nozzle in the sodium and argon regions.

The argon in the space between the nozzle sleeve and the dipper insulates the upper portion of the dipper, and very little heat is transferred into the argon cover gas. Instead, most of the heat generated in the upper 9.2 in. of the fuel is transferred by conduction downward through the fuel region and the sodium within the dipper, and then radially out to the primary-tank sodium. The temperature distribution in the fuel region is shown in Fig. I.11, where the parameter used was the linear heat rate. The figure shows the range of values for the cover-gas region. A uniform linear heat rate was used rather than one with a chopped-cosine distribution, but the results are valid in either case. Because the fuel length used was

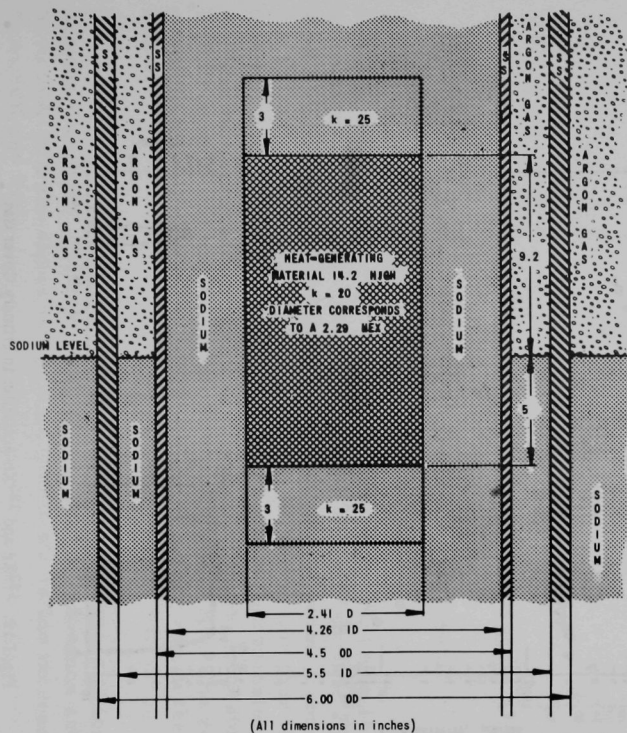


Fig. I.10. Model for THTB Calculations.
 ANL Neg. No. 103-P5642 Rev. 1.

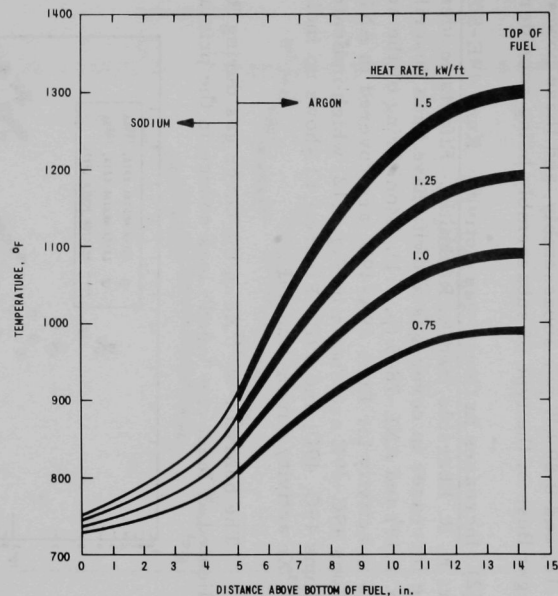


Fig. I.11. Temperature Distribution in Fuel Portion of an Experimental Subassembly in the Failed-fuel Transfer System--Storage Position II. ANL Neg. No. 103-P5641 Rev. 1.

14.2 in., the heat rates of 1.5, 1.25, 1.00, and 0.75 kW/ft correspond to 1.78, 1.48, 1.18, and 0.89 kW per subassembly, and these power productions are valid, regardless of the type of subassembly being considered.

(2) Increases in Cover-gas Activity: Runs 49E-50F

(R. M. Fryer, E. R. Ebersole, and R. R. Smith). Efforts to identify the origins of the increases in cover-gas activity have been described in ANL-7833 (p. 1.19) and ANL-7845 (p. 1.1). Monitoring of the activity, and the increases in activity for Runs 49A-49D, are covered in ANL-7833. The results for Runs 49C-49E are shown in Fig. I.12, which indicates the high activity for Runs 49C, 49D, and 49E. Figure I.13 shows no indication of an increase in ^{133}Xe activity during Run 49F.

The behavior of ^{133}Xe in the cover gas during Run 49F, however, indicated at least one "aged" leak source in the primary tank

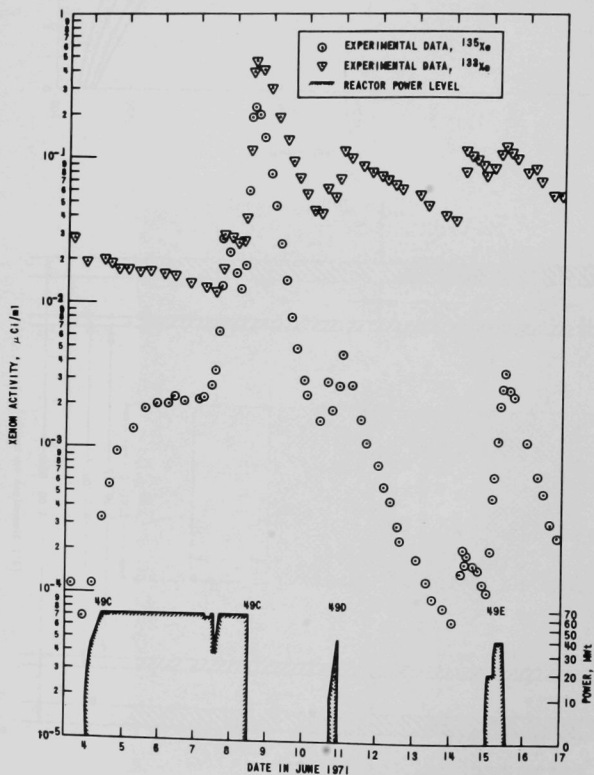


Fig. I.12. ^{133}Xe and ^{135}Xe Activities in Primary Cover Gas, Runs 49C through 49E. ANL Neg. No. 103-P5654.

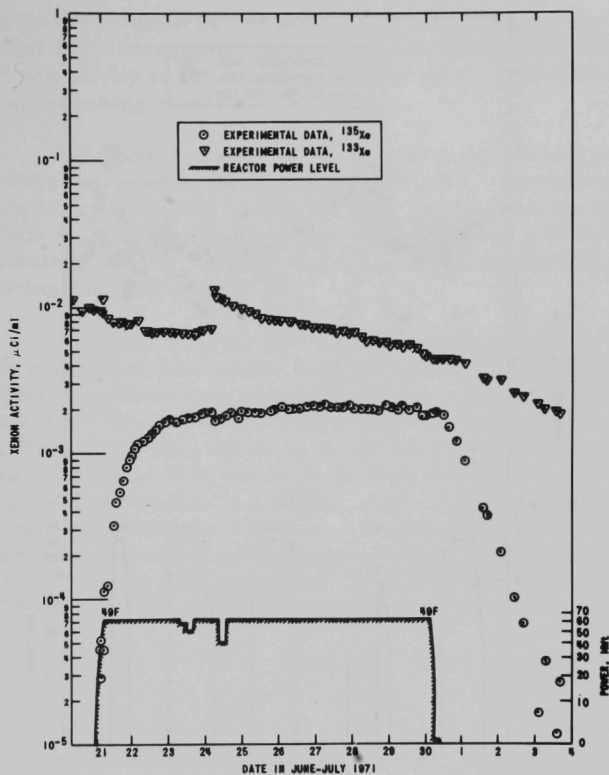


Fig. I.13. ^{133}Xe and ^{135}Xe Activities in Primary Cover Gas, Run 49F. ANL Neg. No. 103-P5658.

(see Fig. I.13). After the release of ^{133}Xe in Run 49E (June 15), the ^{133}Xe decayed normally until reactor startup for Run 49F on June 20-21. During June 21-23, the ^{133}Xe remained essentially unchanged at a concentration of $7 \times 10^{-3} \mu\text{Ci/ml}$ in the cover gas, a level approximately four times the normal tramp saturation background. On June 24, a fuel transfer, with the associated changes in storage-basket elevation, apparently started a gas-bubble release that contained only the long-lived ^{133}Xe . The release was correctly interpreted to be evidence that the leaker was in the basket for Run 49F.

Run 50 was planned for the sole purpose of locating the sub-assembly with the cladding penetration. The data on xenon activity for Runs 50A-50E are shown in Fig. I.14, which shows the increases for Runs 50B and 50E.

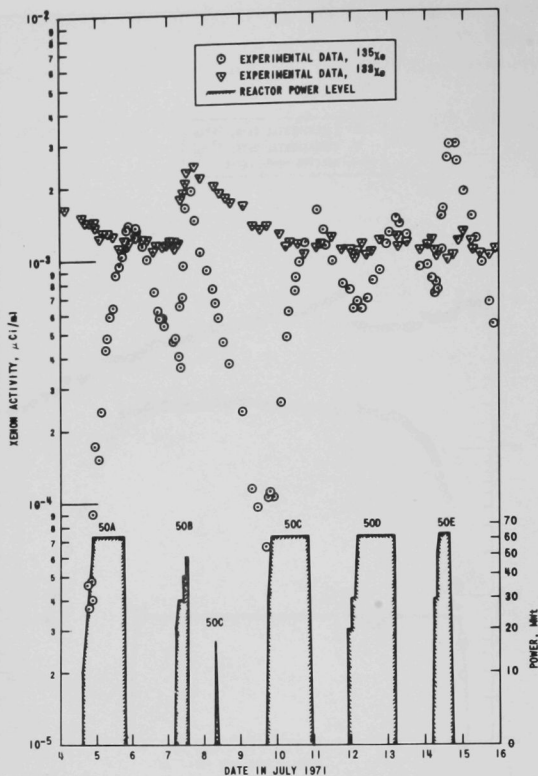


Fig. I.14. ^{133}Xe and ^{135}Xe Activities in Primary Cover Gas, Runs 40A through 50E. ANL Neg. No. 103-P5656.

(3) GLASS (Ge-Li Argon-scanning System) (G. S. Brunson and P. B. Henault). Improvements in the GLASS installation (see ANL-7825, p. 1.61) have been made and some new results are available. Lead shielding was installed around the detector, and the isolation-purge system for the gas-sample chamber was placed in operation.

GLASS detected the increase in cover-gas activity on May 31, at least $1\frac{1}{2}$ min sooner than any other system for fission-product monitoring. This difference was to be expected, because the fission-gas sample stream is surveyed by GLASS before the stream passes through the delay line. However, the results from this activity increase showed a problem of saturation. After consideration of various alternatives, it was decided to increase the dynamic range of the instrument by controlling mechanically the geometric efficiency of the system. A sample chamber incorporating metal bellows has been designed, built, and installed. It will reduce the sensitivity of the

system by a factor of about 100 by decreasing the sample volume at the same time that it increases the average sample-to-detector distance. This reduction of sensitivity is to be triggered by a count-rate circuit, which detects the approaching saturation condition.

The power supply in the GLASS multichannel analyzer failed, and the unit was returned to the factory for repairs. A substitute analyzer provided data of lower quality during the hunt for the leaking subassembly, June 18 to July 9. The repaired analyzer was installed late on July 9, and data were obtained on two "clean" runs of the search before the leaks re-appeared during Run 50E on July 14.

GLASS data obtained on Runs 50D and 50E are presented in Fig. I.15. In addition to data on the isotopes already being monitored with the RCGM (Reactor Cover Gas Monitor) and analyzed in grab samples (^{85m}Kr , ^{133}Xe , and ^{135}Xe), data are also shown for three shorter-lived isotopes (^{87}Kr , ^{88}Kr , and ^{138}Xe), which have not been monitored before. The value of these additional data can be seen from the information they provide on the details of the increase in activity. After the initial indication of an increase in Run 50E, there is evidence of three subsequent, and much smaller, increases (indicated by the arrows). This evidence is rather clear in the curves for ^{138}Xe and ^{87}Kr and is indicated by the data on the longer-lived isotopes. The data on ^{85m}Kr and ^{88}Kr indicate another point. Bridging the

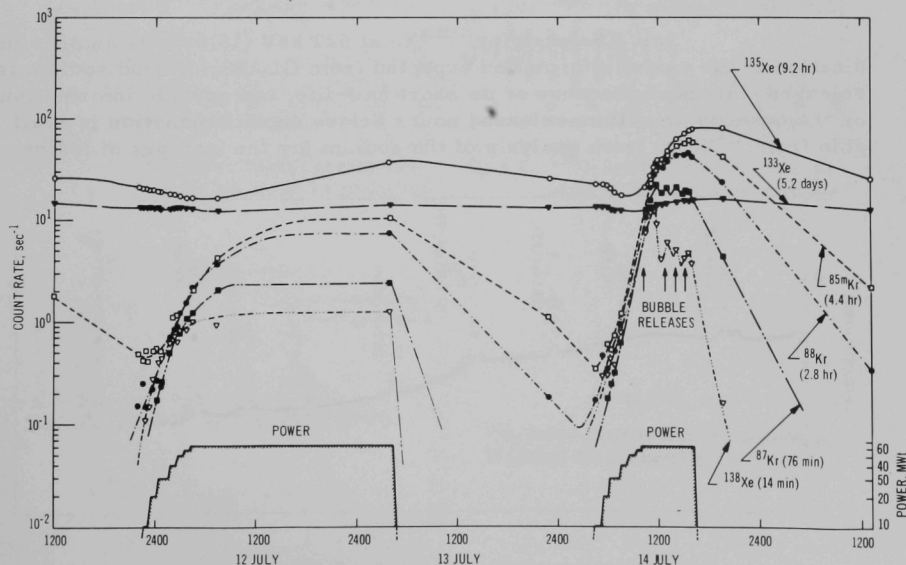


Fig. I.15. Activities of Rare-gas Fission-products as Sensed by GLASS. ANL Neg. No. 103-P5660 Rev. 1.

gap in the data (0359 to 2254, July 13) with straight lines yields slopes shallower than their respective half-lives require, suggesting that a very small increase in activity may have occurred during or after the shutdown following Run 50D.

After the leaking subassembly was removed, sustained reactor operation permitted analysis of a near-equilibrium gamma spectrum, which is shown in Fig. I.16; all isotopes can be considered saturated except for ^{133}Xe , which is about 70% of saturation. Several observations can be made concerning this spectrum:

(a) When GLASS was originally conceived, it was thought that daughters of the radioactive noble gases might "fall out" and deposit a significant background source on the walls of the chamber. This effect has been trivial, and only a very small indication of ^{138}Cs can be seen at 463 and 546 keV.

(b) Xenon-135 is by far the most abundant activity, and it is readily counted with the on-line digital subtract unit (ODSU) described in ANL-7737, p. 94. However, increasing the sensitivity to the point that the other useful isotopes can be easily counted requires too much of the system's dynamic range. To remedy this difficulty, a second type of ODSU was designed and built (see ANL-7825, p. 1.61). This latter device is expected to be more useful, at least for the less-intense activities.

(c) The peak for $^{135\text{m}}\text{Xe}$ at 527 keV (15.6 m) is another indication of the useful information expected from GLASS. If bond sodium is released, this peak, because of its short half-life, can provide information on the quantity of sodium released hours before such information is available from ^{135}Xe or from analysis of the sodium for the isotopes of iodine.

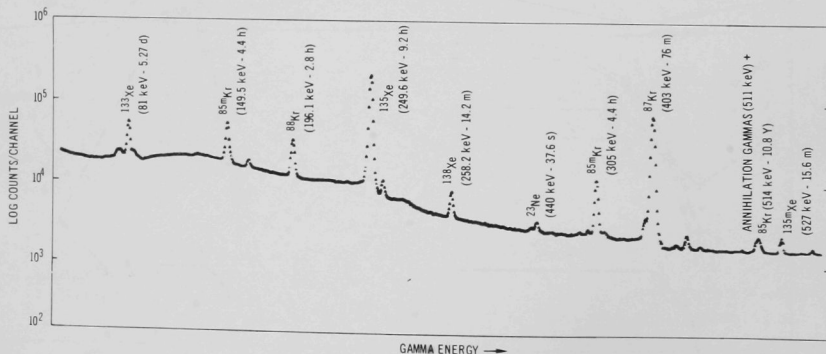


Fig. I.16. Spectrum of Gamma-pulse Height of Tramp Activity as Recorded by GLASS. ANL Neg. No. 103-P5659 Rev. 1.

3. Characterization of Irradiation Environment (02-151; last reported: ANL-7833, p. 1.27)

a. Radial Reaction-rate Traverses for ZPR-3 Assembly 63B. D. G. Stenstrom and D. Meneghetti

Two-dimensional, XY-geometry, S_4 transport neutronic analyses with the DOT code were used to calculate the reaction-rate traverses for $^{235}\text{U}_f$, $^{238}\text{U}_f$, and $^{10}\text{B}_c$ in ZPR-3 Assembly 63B. The 29-group cross-section set was used in the calculations, and axial bucklings of 0.00235 and 0.00085 were used for the core and the reflector/blanket regions, respectively.

Figures I.17, I.18, and I.19 compare the calculated radial traverses through the P row of the assembly for $^{235}\text{U}_f$, $^{238}\text{U}_f$, and $^{10}\text{B}_c$, respectively, with corresponding experimental values reported by the ZPR-3 experimental group in ANL-7776 (p. 12). The individual drawers in the core region through which the detector traverses were made are shown in the figures.

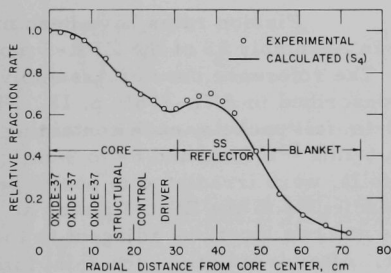


Fig. I.17. $^{235}\text{U}_f$ Radial Traverse at Axial Midplane of Core of ZPR-3 Assembly 63B

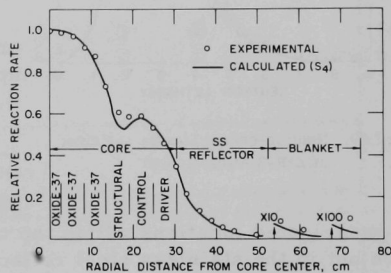


Fig. I.18. $^{238}\text{U}_f$ Radial Traverse at Axial Midplane of Core of ZPR-3 Assembly 63B

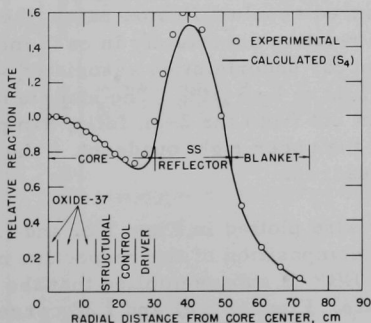


Fig. I.19
 $^{10}\text{B}_c$ Radial Traverse at Axial Midplane of Core of ZPR-3 Assembly 63B

b. Calculated Energy Spectra in ZPR-3 Assembly 63B.
K. E. Phillips, D. Meneghetti, and D. G. Stenstrom

Proton-recoil neutron-spectrum measurements were made at the center of the central zone, which simulates a 37-pin oxide element, of ZPR-3 Assembly 63B. The experiments* are compared with the 1/120-lethargy-width flux spectrum obtained from an MC² calculation of the simulated 37-pin-oxide region. Figure I.20 compares the experimental results with the calculated ultrafine spectrum and with the ultrafine spectrum modified by a 15%-resolution Gaussian energy window.

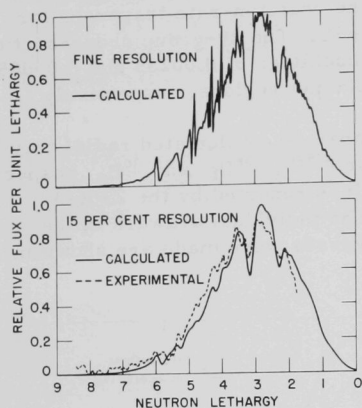


Fig. I.20. Neutron-energy Spectra at Center of ZPR-3 Assembly 63B

13 preselected locations within the core and two locations adjacent to the core but in the stainless steel reflector. After irradiation, the 2-in. foils were cut into 1-in.-square quadrants to provide spatial resolution within each drawer. Sample counting, data processing, and fission-rate determinations were identical with those reported for Assemblies 60-62. (See, for example, ANL-7753, p. 92.)

Table I.1 shows the measured absolute fission rates, the matrix location within the assembly, and the relative uncertainty in each measurement. All errors are included, except for uncertainties associated with absolute fission yields; these are thought to be 5-10%. The sample number at each location refers to the quadrant cut from the 2-in. foils; Sample 1 represents the upper left quadrant, 2 the upper right quadrant, 3 the lower left quadrant, and 4 the lower right quadrant.

The fission-rate data are also plotted in Figs. I.21 and I.22 to emphasize the effects of position and composition of the respective matrix positions. The figures show types of EBR-II subassemblies that the respective drawers were designed to simulate. Figures I.21 and I.22 correspond to

c. Fission-rate Measurements in ZPR-3 Assembly 63.

N. R. Dudey, R. J. Popek, and R. R. Heinrich

Fission rates have been measured in Assembly 63 of the ZPR-3 mock-ups. The reference core of Assembly 63* was described in ANL-7765, p. 18. Fifteen 2 x 2-in. foil packets, each containing 3- to 6-mil ²³⁵U foils and 6- to 9-mil ²³⁸U foils, were irradiated in positions perpendicular to the ZPR-3 plates at

*G. G. Simons, ANL internal memorandum (May 25, 1971).

TABLE I.1. Absolute Fission Rates (in 10^{-15} fissions/atom-sec) for ^{235}U and ^{238}U Samples Irradiated in ZPR-3 Assembly 63

| Matrix Position | Sample | ^{235}U | | ^{238}U | | Matrix Position | Sample | ^{235}U | | ^{238}U | |
|-----------------|--------|------------------|----------|------------------|----------|-----------------|--------|------------------|----------|------------------|----------|
| | | Rate | Error, % | Rate | Error, % | | | Rate | Error, % | Rate | Error, % |
| P-16 | 1 | 39.9 | 2.1 | 2.84 | 2.5 | O-15 | 1 | 37.2 | 2.1 | 2.20 | 2.3 |
| | 2 | 40.2 | 2.1 | 2.84 | 2.4 | | 2 | 36.7 | 2.3 | 2.29 | 2.3 |
| | 3 | 39.6 | 2.2 | 2.77 | 2.4 | | 3 | 37.2 | 2.1 | 2.23 | 2.6 |
| | 4 | 39.9 | 2.1 | 2.85 | 2.4 | | 4 | 38.4 | 2.2 | 2.33 | 2.4 |
| P-15 | 1 | 38.6 | 2.2 | 2.57 | 2.4 | Q-11 | 1 | 26.9 | 2.2 | 1.15 | 2.4 |
| | 2 | 39.8 | 2.1 | 2.71 | 2.4 | | 2 | 26.6 | 2.2 | 1.38 | 2.3 |
| | 3 | 38.2 | 2.2 | 2.59 | 2.6 | | 3 | 26.5 | 2.1 | 1.16 | 2.5 |
| | 4 | 39.4 | 2.2 | 2.72 | 2.5 | | 4 | 26.4 | 2.1 | 1.38 | 2.3 |
| P-14 | 1 | 36.1 | 2.2 | 2.34 | 2.6 | P-11 | 1 | 26.8 | 2.4 | 1.21 | 2.4 |
| | 2 | 37.4 | 2.2 | 2.52 | 2.3 | | 2 | 26.8 | 2.3 | 1.43 | 2.4 |
| | 3 | 36.1 | 2.2 | 2.32 | 2.4 | | 3 | 26.7 | 2.1 | 1.12 | 2.3 |
| | 4 | 37.3 | 2.1 | 2.44 | 2.3 | | 4 | 26.5 | 2.2 | 1.40 | 2.3 |
| P-13 | 1 | 32.3 | 2.2 | 1.68 | 2.6 | O-11 | 1 | 25.7 | 2.3 | 1.37 | 2.4 |
| | 2 | 34.5 | 2.2 | 1.86 | 2.7 | | 2 | 27.0 | 2.1 | 1.51 | 2.3 |
| | 3 | 32.5 | 2.3 | 1.64 | 2.6 | | 3 | 26.1 | 2.1 | 1.32 | 2.7 |
| | 4 | 34.5 | 2.1 | 1.87 | 2.7 | | 4 | 27.0 | 2.1 | 1.52 | 2.6 |
| M-15 | 1 | 33.6 | 2.1 | 2.30 | 2.8 | P-10 | 1 | 29.6 | 2.2 | 0.480 | 2.7 |
| | 2 | 34.7 | 2.2 | 2.41 | 2.6 | | 2 | 28.8 | 2.4 | 0.715 | 3.0 |
| | 3 | 35.3 | 2.3 | 2.46 | 2.4 | | 3 | 30.1 | 2.2 | 0.466 | 2.7 |
| | 4 | 35.7 | 2.2 | 2.58 | 2.3 | | 4 | 28.6 | 2.2 | 0.682 | 2.9 |
| L-15 | 1 | 30.0 | 2.3 | 1.74 | 2.8 | K-15 | 1 | 28.9 | 2.1 | 1.13 | 3.1 |
| | 2 | 30.2 | 2.2 | 1.79 | 2.8 | | 2 | 27.5 | 2.4 | 1.35 | 2.8 |
| | 3 | 32.2 | 2.2 | 1.96 | 2.5 | | 3 | 28.5 | 2.3 | 1.44 | 2.7 |
| | 4 | 32.0 | 2.2 | 2.02 | 2.5 | | 4 | 28.4 | 2.3 | 1.58 | 2.3 |
| N-12 | 1 | 27.3 | 2.3 | 1.56 | 2.4 | J-15 | 1 | 31.0 | 2.2 | 0.452 | 3.0 |
| | 2 | 28.3 | 2.2 | 1.69 | 2.4 | | 2 | 30.4 | 2.2 | 0.515 | 3.5 |
| | 3 | 27.9 | 2.2 | 1.59 | 2.5 | | 3 | 30.0 | 2.3 | 0.666 | 2.8 |
| | 4 | 29.4 | 2.2 | 1.80 | 2.5 | | 4 | 28.9 | 2.2 | 0.753 | 2.9 |
| P-12 | 1 | 28.9 | 2.1 | 1.67 | 2.4 | | | | | | |
| | 2 | 30.8 | 2.2 | 1.77 | 2.4 | | | | | | |
| | 3 | 28.9 | 2.3 | 1.64 | 2.5 | | | | | | |
| | 4 | 30.3 | 2.1 | 1.73 | 2.3 | | | | | | |

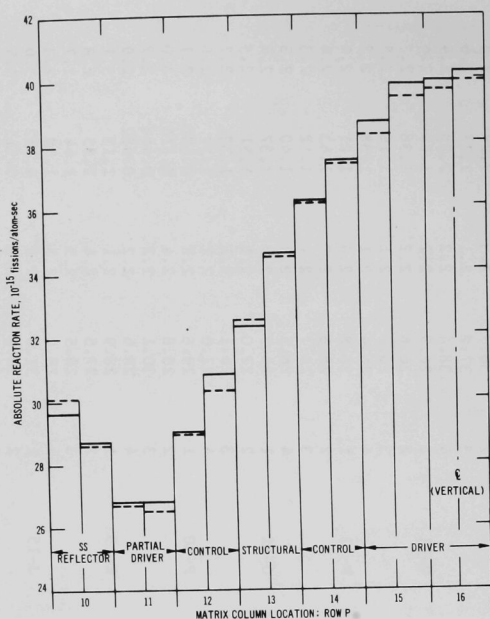


Fig. I.21. Horizontal Traverse of ^{235}U Fission-rate Distribution in ZPR-3 Assembly 63

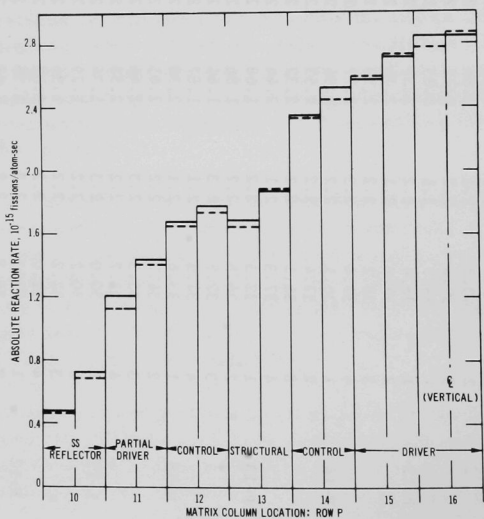


Fig. I.22. Horizontal Traverse of ^{238}U Fission-rate Distribution in ZPR-3 Assembly 63

horizontal traverses along Row P for ^{235}U and ^{238}U , respectively. Two values at each measurement point are shown: The solid lines represent samples above the horizontal centerline of the reactor (top half of Row P), and the dashed lines represent samples below the center horizontal line. Differences between the two lines reflect experimental precision or spectral asymmetries about the reactor centerline, or both. In no location do the measurements from the top and bottom half of the Row P traverses differ by more than 2%. These results may be compared with ^{235}U and ^{238}U fission-counter traverses also measured in Row P of Assembly 63 (see ANL-7765, p. 15). The spatial variations in reaction rates determined in the two experiments are in satisfactory agreement; the spectral-depression effects from the structural subassembly (P-13) are demonstrated in both measurements by ^{238}U fission rates.

d. EBR-II Dosimetry Study. A. A. Madson

The first two of a series of three irradiations in EBR-II of subassemblies containing dosimetry-foil materials have been concluded. The first irradiation (Run 50G) was conducted at 50 kWt for 1 hr. The second irradiation (Run 50H) was conducted at 62.5 MWt for $8\frac{1}{2}$ days. The dosimetry subassemblies have been removed from the reactor and disassembled to retrieve the foil materials. The foils have been shipped to various laboratories, where counting and analysis are in progress.

e. Comparison of Calculated and Measured ^{235}U and ^{238}U Activations in EBR-II Run 29D. B. R. Sehgal, F. S. Kirn, and R. H. Rempert

Spatial distributions of ^{235}U and ^{238}U fissions were measured in EBR-II Run 29D at selected axial and radial positions in the core, the radial depleted-uranium blanket, and the axial stainless steel reflectors. The ^{235}U detectors were in the form of 1/16-in.-dia uranium-aluminum wires (with 15% of 93% enriched uranium), and the depleted-uranium detectors were 1/32-in.-dia wires. Relative fission rates after irradiation at 50 kW* for 1 hr were determined by counting the wires with NaI crystal counters; the gross gamma count between 0.5 and 1.0 MeV was used. Absolute fissions were determined for some samples by making absolute determinations of ^{99}Mo , the values for fission yields of 6.1 and 6.3%, respectively, being used for ^{235}U and ^{238}U fission.

The usual detailed representation of geometry and composition of the reactor was used in 2-D calculations with the DOT** transport code in the S_4 approximation. In the XY geometry the individual subassemblies of different compositions were represented explicitly and the axial leakage

*H. C. Honeck, ENDF/B, Specifications for an Evaluated Nuclear Data File for Reactor Applications, BNL-50066 (T-467), ENDF102 (July 1967).

**F. R. Mynatt, DOT, A Two-dimensional Discrete-ordinates Transport Code, K-1694, Radiation Shielding Information Center, ORNL.

was approximated with a DB^2 absorption at a constant B^2 . In the R-Z geometry, the subassemblies comprising a row were volume-homogenized and the axial reflectors were represented explicitly.

The 29-group set derived with the MC^2 code* from the ENDF/B (Version I) data** was used. The core-region cross sections were calculated at critical buckling and the others at zero buckling. Detector cross sections were averaged over the fine spectrum of the different reactor regions.

The calculated and measured ^{235}U radial fission distribution at the core midplane are compared in Fig. I.23. There is good agreement except beyond Row 6 (core edge), where the differences are ≈ 6 to 10%. Figure I.24 compares the calculated ^{238}U fissions with the measurements made in three subassemblies in three core positions. The agreement is good.

Similar differences between calculated and measured fission distributions were observed in the analysis of the data from the critical assemblies† using the same cross-section data and methods of analysis.

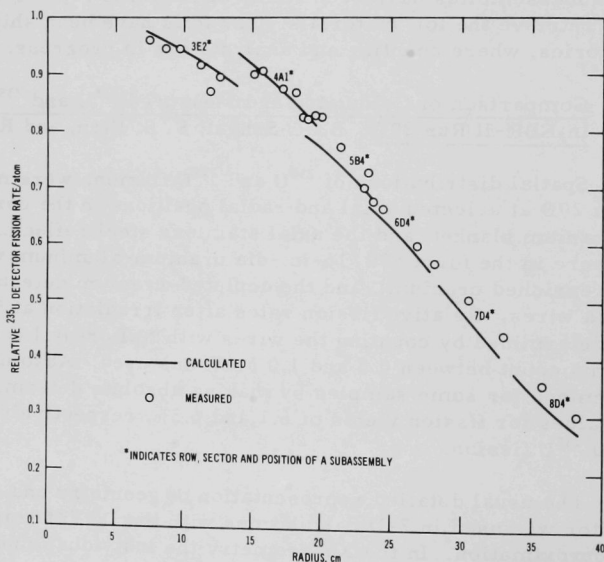


Fig. I.23. Radial ^{235}U Fission Distribution in EBR-II Run 29D

*B. J. Toppel, A. L. Rago, and D. M. O'Shea, MC^2 , A Code to Calculate Multigroup Cross Sections, ANL-7318 (June 1967).

**H. C. Honeck, *ibid.*

†D. Meneghetti *et al.*, Depleted-uranium, Nickel, and Steel-reflected EBR-II Critical Assemblies in ZPR-3--Experiments and Calculations, Trans. Am. Nucl. Soc. 13, 733 (1970).
p. 89; and ANL-7765, p. 48.

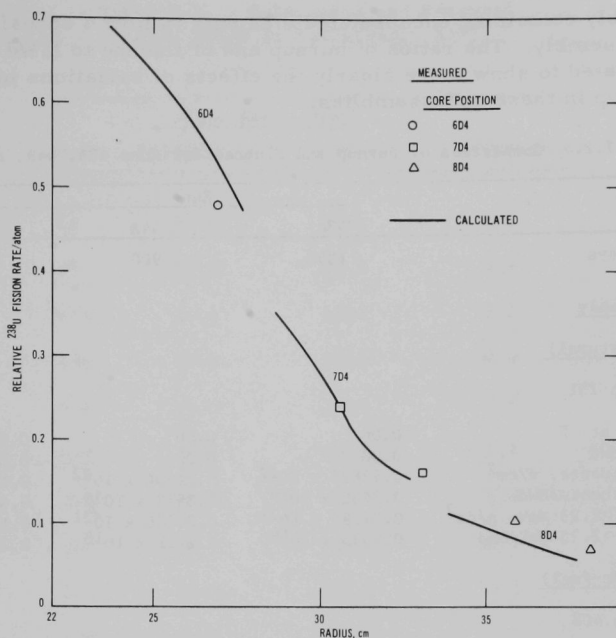


Fig. 1.24. Radial ^{238}U Fission Distribution in EBR-II Run 29D

The calculated spatial ^{235}U and ^{238}U fission distributions showed differences of 3-15% at equivalent subassembly positions and predicted the measured local variations well.

f. Testing of Burnup Calculation System. P. L. Walker

A set of computer programs is being written to calculate the burnup history of EBR-II. The REBUS code from the ARC programming system is being used for the burnup and depletion parts of the calculation. The DOT transport code will be used for the neutronics calculations, which will be done with S_4 quadrature. To test some aspects of the two-dimensional XY-geometry burnup computations, a series of burnup calculations was done. The simpler diffusion module DIF2D was used for the neutronics solutions, instead of a transport calculation. This series, which was for Runs 43A, 44A, and 44B, was started by using output data from the previous run (42A) and proceeded from run to run by using as input only the loading changes.

Some of the results of these runs are given in Table I.2. The burnup and fluence are tabulated for a subassembly of structural materials near the center, a driver-fuel subassembly in Row 4, and an experimental

subassembly containing encapsulated elements in Row 4 opposite the driver-fuel subassembly. The ratios of burnup and of fluence to MWd have also been tabulated to show more clearly the effects of variations in flux level upon burnup in these subassemblies.

TABLE I.2. Comparison of Burnup and Fluence for Runs 43A, 44A, and 44B

| | Run | | |
|--------------------------------------|--------------------------|--------------------------|--------------------------|
| | 43A | 44A | 44B |
| Megawatt Days | 1350 | 900 | 450 |
| <u>Subassembly</u> | | | |
| <u>X057 (Structural)</u> | | | |
| Position 2B1 | | | |
| Burnup, at. % | 0.00 | 0.00 | 0.00 |
| Burnup/MWd | 0.00 | 0.00 | 0.00 |
| Total fluence, n/cm ² | 0.47676×10^{22} | 0.31606×10^{22} | 0.15979×10^{22} |
| Total fluence/MWd | 0.3532×10^{19} | 0.3512×10^{19} | 0.3551×10^{19} |
| Fluence >2.23 MeV, n/cm ² | 0.34195×10^{21} | 0.21786×10^{21} | 0.11378×10^{21} |
| Fluence >2.23 MeV/MWd | 0.2533×10^{18} | 0.2421×10^{18} | 0.2528×10^{18} |
| <u>2207 (Driver-fuel)</u> | | | |
| Position 4C2 | | | |
| Burnup, at. % | 0.34855 | 0.23303 | 0.11767 |
| Burnup/MWd | 0.2581×10^{-4} | 0.2589×10^{-4} | 0.2615×10^{-4} |
| Total fluence, n/cm ² | 0.44942×10^{22} | 0.30087×10^{22} | 0.15278×10^{22} |
| Total fluence/MWd | 0.3329×10^{19} | 0.3343×10^{19} | 0.3395×10^{19} |
| Fluence >2.23 MeV, n/cm ² | 0.39852×10^{21} | 0.26763×10^{21} | 0.13684×10^{21} |
| Fluence >2.23 MeV/MWd | 0.2952×10^{18} | 0.2978×10^{18} | 0.3041×10^{18} |
| <u>X064 (Experimental)</u> | | | |
| Position 4F2 | | | |
| Burnup, at. % | 0.47856 | 0.32816 | 0.16095 |
| Burnup/MWd | 0.3545×10^{-4} | 0.3646×10^{-4} | 0.3577×10^{-4} |
| Total fluence, n/cm ² | 0.35383×10^{22} | 0.24304×10^{22} | 0.11908×10^{22} |
| Total fluence/MWd | 0.2621×10^{19} | 0.2700×10^{19} | 0.2646×10^{19} |
| Fluence >2.23 MeV, n/cm ² | 0.31336×10^{21} | 0.21591×10^{21} | 0.10619×10^{21} |
| Fluence >2.23 MeV/MWd | 0.2321×10^{18} | 0.2399×10^{18} | 0.2360×10^{18} |

g. Comparison of Calculated and Measured Flow Rates in Subassembly XX02. J. L. Gillette

The calculated flow rates reported in ANL-7825 (p. 1.49) have been slightly revised because the hydraulic characteristics of some of the half-fueled subassemblies used in the earlier calculations were incorrect. The new results are presented in Table I.3, which replaces Table I.20 in ANL-7825.

TABLE I.3. Calculated and Measured
Flow Rates in Subassembly XX02

| Run | Flow Rate, gpm | | % Difference |
|-----|----------------|----------|--------------|
| | Calculated | Measured | |
| 42 | 53.0 | 52.5 | 1.0 |
| 43 | 51.9 | 51.5 | 0.8 |
| 44A | 51.6 | 51.0 | 1.2 |
| 44B | 50.9 | 50.5 | 0.8 |
| 45A | 51.0 | 50.0 | 2.0 |
| 45B | 50.1 | 49.2 | 1.8 |
| 46A | 49.0 | 46.5 | 5.4 |
| 46B | 48.7 | 46.5 | 4.7 |
| 47A | 49.0 | 46.6 | 5.2 |
| 47B | 49.6 | 46.2 | 7.4 |
| 48A | 49.2 | 46.5 | 5.8 |
| 48B | 49.1 | 46.5 | 5.6 |
| 48C | 49.5 | 46.5 | 6.5 |
| 48D | 50.1 | 46.7 | 7.3 |
| 48E | 49.9 | 46.5 | 7.3 |

The discussion in ANL-7825 is correct and is not affected by these new results.

4. Operation of Digital Data Acquisition System (DAS) (02-530; last reported: ANL-7833, p. 1.34)

a. Operational Support. M. R. Tuck and K. D. Tucker

Work on the data-acquisition software completed this month included the following:

- (1) A sampling rate of 10/sec has been added to the existing ones because 2/sec appeared insufficient to keep the error from accumulating in the inverse-kinetics calculation.

(2) The use of system library routines in the convert-to-engineering portion of this software has been discontinued because of the large amount of core used by these routines. Wherever possible, a third- or fourth-order polynomial has been used to replace these routines.

The Graphics Display Library (GDL) has been received for the DAS. This library allows the programmer to easily exercise the full capability of the DAS graphics-display unit. The GDL also enables the user to display vectors and characters on the cathode-ray tube of the graphics display unit. Intensity, character size, and blinking functions are all under program control. In addition, the user can modify the display programs through the use of the light gun, keyboard, and various hardware-function switches.

b. Test-data Acquisition and Support

(1) Data Obtained by DAS (W. R. Wallin). The DAS is being increasingly used to process operating data--e.g., temperatures, pressures, and flow rates. At present, 146 signals from various sensors are being recorded with the DAS. Of these signals, 44 are directly processed by the DAS for use in the Run Report. Mean, maximum, and minimum values for a given data set are computed each hour, and each value can be displayed visually on a cathode-ray tube and photographed. Enlargements of the photographs can then be used for analysis and directly in the Run Report. An example of the data format is given in Fig. I.25, which shows temperature data for about two weeks from three subassembly-outlet thermocouples.

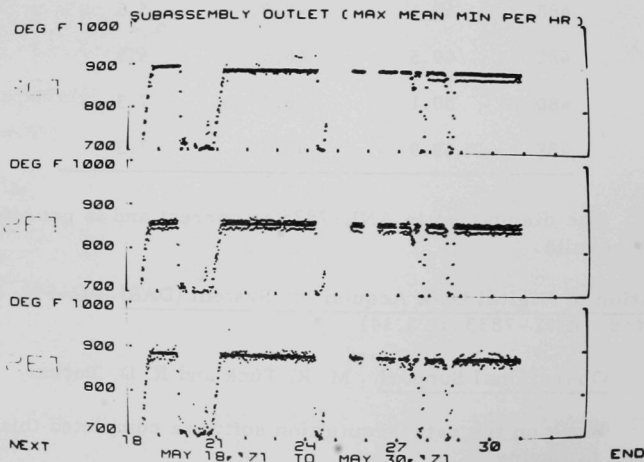


Fig. I.25. Typical Graphic Display of Operating Plant Data

(2) Maintenance of Data Acquisition System (R. A. Call).

Table I.4 shows malfunctions of the DAS since system acceptance.

TABLE I.4. Log of Downtime for Sigma-5

| Trouble or Symptom | Time of Occurrence | Time Repaired | Downtime, hours | Description of Malfunction | Action Taken | System Malfunction ^a |
|----------------------------------|--------------------|------------------|-----------------|---|--------------------------|---------------------------------|
| RAD ^b not recognized | 10/19/70 0830 | 10/19/70 0900 | 0:30 | 2400-Hz power-supply breaker opened | Reset breaker | Yes |
| Malfunction of RAD No. 1 | 10/28/70 | 10/30/70 | 48:00 | Tachometer malfunctioned | Replaced tachometer | Yes |
| RAD not recognized | 11/2/70 0800 | 11/2/70 0810 | 0:10 | 2400-Hz power-supply breaker opened | Reset breaker | Yes |
| RAD No. 1 failed | 11/11/70 0800 | 11/11/70 1300 | 5:00 | Tachometer and control-circuit power supply malfunctioned | Replaced defective parts | Yes |
| Malfunction of power-supply fan | 11/23/70 0800 | 11/23/70 1100 | 3:00 | Fan bearings malfunctioned | Replaced power supply | Yes |
| RAD not recognized | 1/8/71 0800 | 1/8/71 1030 | 2:30 | 2400-Hz power-supply breaker opened | Replaced power supply | Yes |
| Malfunction of line printer | 2/12/71 1530 | 2/12/71 1600 | 0:30 | Blown fuse in clutch circuit | Replaced fuse | Yes |
| Malfunction of DM40 power supply | 5/24/71 1000 | 5/25/71 1000 | 24:00 | +12 clamp circuit malfunctioned | Replaced power supply | Yes |
| Malfunction of graphic display | 7/13/71 1000 | 7/14/71 1300 | 27:00 | Low-voltage power supply malfunctioned | Replaced power supply | No |

^aSystem cannot acquire and log data or support reactor operations.^bRapid-access Disk.

PUBLICATIONS

Identification and Removal of the Noise Source in the EBR-II Intermediate Heat Exchanger (IHX)

H. W. Buschman, B. C. Cerutti, and A. F. Clark

Trans. Am. Nucl. Soc. 14(Suppl. 2), 28 (Aug 1971) Abstract

Removal and Modification of Primary Sodium Pump at EBR-II

G. E. Deegan, W. H. Perry, and R. E. Seever

Trans. Am. Nucl. Soc. 14(Suppl. 2), 29 (Aug 1971) Abstract

Operating Experience and Evaluation of the EBR-II Emergency Power System

J. R. Goodrich

ANL/EBR-038 (Apr 1971)

In-Line Vacuum-Distillation Sodium Sampler

W. H. Olson

Nucl. Technol. 12, 7-11 (Sept 1971)

Computer-Aided Experimental Support

M. R. Tuck, I. A. Engen, and R. W. Hyndman

Trans. Am. Nucl. Soc. 14(Suppl. 2), 34 (Aug 1971) Abstract

Application of a Medium-Scale Digital Computer to Operational Support of EBR-II

K. D. Tucker, E. W. Laird, and R. W. Hyndman

Trans. Am. Nucl. Soc. 14(Suppl. 2), 33 (Aug 1971) Abstract

Modification of the EBR-II Core Fuel Handling Holddown Mechanism

J. B. Waldo, H. W. Sine, and J. S. Remsburg

Trans. Am. Nucl. Soc. 14(Suppl. 2), 29 (Aug 1971) Abstract

II. LMFBR DESIGN SUPPORT

A. Heat Transfer and Fluid Flow

R. P. Stein (02-097)

Analytical and experimental investigations of liquid-metal heat transfer and fluid flow in components and systems are conducted to provide information of immediate interest to the FFTF and LMFBR Programs. Fundamental studies in heat transfer and fluid flow also are conducted to improve current, or to devise new, engineering prediction methods essential to the advancement of reactor technology in general.

1. LMFBR Flow Stability Studies. R. R. Rohde

This activity covers (1) the acquisition and analysis of experimental data on the vaporization and superheating of sodium in operating ranges (pressures, flow rates, temperatures, and equivalent diameters) and flow circuits of interest to the LMFBR Program; and (2) the determination, by both experiment and analysis, of two-phase flow phenomena related to flow stability. An LMFBR Simulation Heat Transfer Loop is being constructed for the experiments.

a. Preparation of Apparatus (Last reported: ANL-7845, p. 2.1)

The status of construction of the LMFBR Simulation Heat Transfer Loop is as follows: Enclosure panels for the loop were lined with sheet metal as a safeguard against sodium fires. Connection of thermocouples to the multipen recorders is about 70% complete. Special reducer fittings for connecting the electromagnetic pumps in the Sodium Purification and Monitoring System were fabricated. Tubing and certified material for fabricating the balance of fittings needed in this system have been obtained. Twelve amplifiers for the loop instrumentation were received, checked out, and found to be operating properly.

2. Nonboiling Transient Heat Transfer. R. P. Stein

The objective of this activity is to develop improved engineering prediction methods to account for nonboiling forced-convection heat transfer in ducts during transients.

a. Analysis of Heat-flux Transients (Last reported: ANL-7845, p. 2.1)

The new prediction methods have been successfully applied to sample cases in which heat generation within the walls is specified. Previous attempts, which involve application of finite-difference techniques for solving a complex set of partial differential equations, had resulted in

what appeared to be numerical instabilities. Alternate finite-differencing schemes have been developed which remove these instabilities.

It is planned to apply the new prediction methods to a variety of sample cases illustrative of possible LMFBR power excursions. Analyses related to flow transients will be initiated.

3. Liquid-metal Heat Transfer in Pin Bundles. T. Ginsberg

The objectives of this activity are to: (1) develop and evaluate analytical models for predicting steady-state temperature distributions in LMFBR fuel assemblies, and (2) develop empirical data and correlations for use in the analytical models. The latter objective includes development of a model that describes the interchannel-mixing mechanism in fuel assemblies containing helical-wire-wrapped fuel elements.

a. Analytical Investigations (Last reported: ANL-7845, p. 2.2)

The swirl-flow model used in conjunction with the COBRA-II computer code* specified that where a helical spacer wire completes a traverse of a subchannel, it transports a fraction of the flow from the previous subchannel to the one ahead of it. Thus the directional nature of the fluid-transport mechanism is accounted for in the model.

A modified version of this model, in which only energy is transported between subchannels, was incorporated into the COBRA code. The code was altered to accept this modified model, and to accept up to 96 subchannels and 37 rods. The EBR-II Fuel Subassembly No. X040A geometry, flow, and power characteristics were supplied as input to the code.

To display the effect of the directional transport model on the mixing characteristics of the helical spacer wires, a test case was run at zero power. The central six subchannels were assigned an inlet sodium temperature of 1000°F, with the remaining subchannels at 700°F. Figure II.1 shows the calculated temperature distributions for a central channel and for one of the remaining channels. The distributions display a periodic dependence on axial distance, and the characteristic "wavelength" is equal to the spacer pitch. This behavior has been observed experimentally.**

Temperature distributions were then computed for the X040A subassembly, using various combinations of turbulent mixing factor β , thermal-conduction geometry factor, and fraction of flow diverted in the swirl-flow model. The results are shown in Fig. II.2. Also shown is the result of a

*D. S. Rowe, COBRA-II: Digital Computer Program for Thermal-hydraulic Subchannel Analysis of Rod-bundle Nuclear Fuel Elements, BNWL-1229 (1970).

**V. R. Marian and D. P. Hines, Transfer of Coolant between Adjacent Subchannels in Wire-wrap and Grid-spacer Rod Bundles, Trans. Am. Nucl. Soc. 13(2), 807 (1970).

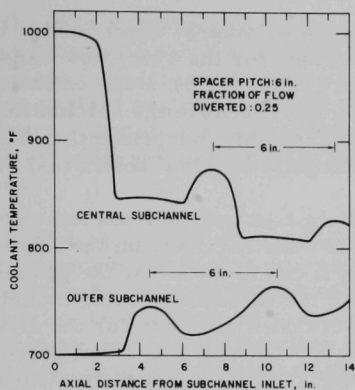


Fig. II.1
Axial Temperature Distribution
for the Zero-power Case

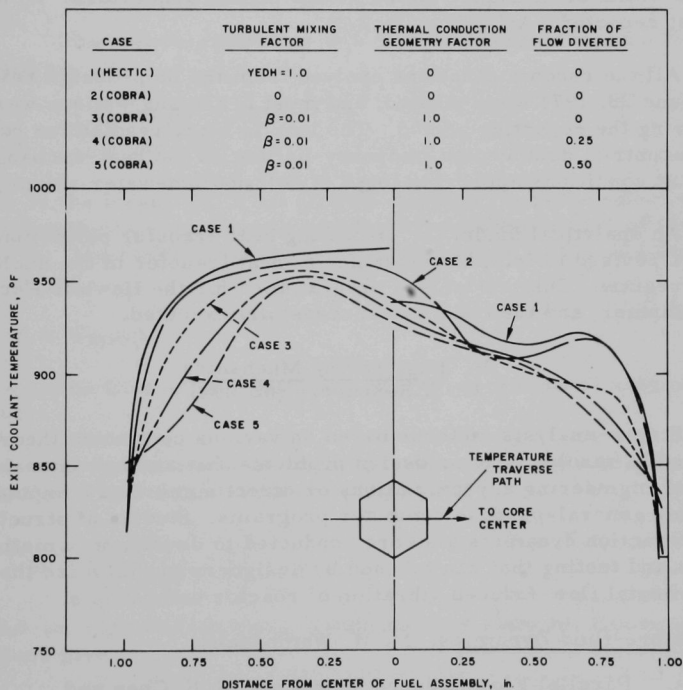


Fig. II.2. Computed Temperature Distributions at
Exit of EBR-II X040A Fuel Assembly

HECTIC Code* calculation, performed by others, which uses a turbulent-mixing model (nondirectional) to account for the swirl flow caused by the wire wrap. For the case presented (YEDH = 1.0), a discontinuity occurs in the curve at the subassembly centerline, because the calculations were performed using two sectors of the assembly independently. The dips in the Case 2 curve are due to the proximity of a low-power fuel element.

It is difficult to draw firm conclusions from the above results because temperature measurements were not made on the X040A subassembly. At the present time, however, it can be said that the proposed swirl-flow model is a viable alternative to the turbulent-mixing model. The strength of the model lies in the fact that it accounts for the directional flow characteristics of helical spacer wire systems. Comparison of COBRA calculations using the swirl-flow model with temperature measurements from instrumented EBR-II subassemblies is planned.

4. Heat Transfer in Liquid-metal-heated Steam Generators. D. M. France
(Last reported: ANL-7845, p. 2.2)

All the recommendations evolved from the loop-design review meeting of June 28, 1971 were studied, and most of the suggestions were complied with during the reporting period. The loop is being readied for experiments on a concentric, double-pipe, mercury-boiling Freon heat-exchanger test section at conditions approximating LMFBR sodium-water steam generators.

An analytical model for predicting heat-transfer performance of the loop was revised to include resistance to heat transfer in the nucleate boiling regime. This model was programmed for the Hewlett-Packard 2100 computer, and the code was successfully executed.

B. Engineering Mechanics
G. S. Rosenberg (02-099)

Stress-analysis methods based on various continuum theories are developed to resolve reactor design problems that are not amenable to conventional engineering approximations or direct numerical computations employing general-purpose computer programs. Studies of structure-fluid interaction dynamics also are conducted to develop new methods of analysis and testing that can be used by designers to minimize the potential of detrimental flow-induced vibration of reactor components.

1. Structure-fluid Dynamics. M. W. Wambsganss

- a. Parallel Flow-induced Vibration. S. S. Chen and
M. W. Wambsganss (Last reported: ANL-7845, p. 2.3)

A series of experiments designed to validate a mathematical model describing the "added mass" effect associated with vibration of a

*N. Kattchee and W. C. Reynolds, HECTIC-II, An IBM-7090 FORTRAN Computer Program for Heat-transfer Analysis of Gas or Liquid Cooled Reactor Passages, IDO-28595 (1965).

cylindrical rod in a fluid annulus were reported in ANL-7825, p. 2.7, under the heading "Damping and Virtual Mass." In these experiments, the change in virtual mass was sensed by measuring resonant frequency of the test element for various annular gaps and specified test-element displacements. This approach assumes that any changes in resonant frequency caused by changes in damping are negligible in comparison with the change caused by virtual mass.

For each value of maintained, rms-displacement of the test element, measurements of period are made at each annular gap. By traversing two cycles of increasing and decreasing annular gaps over the range from 0.125 to 1.0 in., four independent measurements are obtained. Measurements at a given gap are compared to assess reliability and, if reliability is shown, then averaged. The rms value of the current supplied to the exciter coils to maintain the vibration is also measured; this result allows computation of a measure of the change in effective damping with annular gap.

The natural frequency of a cantilever vibrating in a fluid can be expressed as

$$f_n = \frac{3.52}{2\pi \ell^2} \sqrt{\frac{EI}{m+M}}, \quad (1)$$

where ℓ is the length, EI is the flexural rigidity, m is the effective mass per unit length of the cantilever, and M is the "added mass" of fluid per unit length. The "added mass" can be expressed in terms of a correction factor C_M as

$$M = C_M \rho_f A, \quad (2)$$

where ρ_f is the fluid density, and A is the cross-sectional area of the cantilever.

If f_0 is denoted the natural frequency of the cantilever in air ($M \approx 0$), Eqs. 1 and 2 can be combined to obtain

$$C_M = \frac{m}{\rho_f A} \left[\left(\frac{f_0}{f_n} \right)^2 - 1 \right]. \quad (3)$$

For a 0.5-in.-dia, 28.1-in.-long, aluminum test element, theoretical considerations give

$$C_M = 3.31 \left[\left(\frac{f_0}{f_n} \right)^2 - 1 \right]. \quad (4)$$

Having experimental measurements of f_0 and f_n for various annular gaps, we can plot C_M versus flow-channel- to test-element-diameter ratio (D/d).

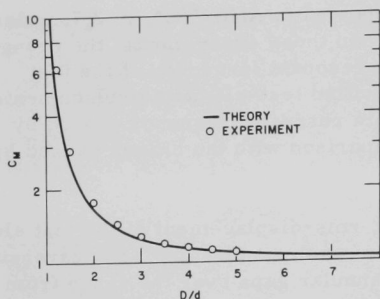


Fig. II.3. Correction Factor (C_M) as a Function of Flow-channel- to Test-element-diameter Ratio (D/d)

In Fig. II.3, the solid curve is the theoretically derived relationship for the correction factor obtained by neglecting viscous effects. The averaged experimental data plotted were obtained using the relationship

$$C_M = 3.25 \left[\left(\frac{f_0}{f_n} \right)^2 - 1 \right] \quad (5)$$

to compute the correction factor. The value of 3.25 for the coefficient was obtained by forcing the data to fit at $D/d = 5$; this value compares favorably with the theoretical value of 3.31. Both theory and experiment agree well over

the range tested; this tends to verify the mathematical model for "added mass" proposed in ANL-7825. However, further theoretical and experimental studies, including the effect of viscosity, are planned.

2. Components Impulse Response. C. K. Youngdahl

NOTE: This activity was initiated on July 1, 1971; it is a continuation of selected aspects of work performed for the Core Structural Safety Program, which terminated on that date.

- a. Dynamic Plasticity Analysis of Hexagonal Shells. C. K. Youngdahl
(Last reported: ANL-7798, p. 116)

For the initial study of hexagonal-subassembly-can deformations, the can was assumed to be made of a rigid, perfectly plastic material, and uniformly loaded internally. The deformations of interest are of the order of the thickness of the can wall or larger; thus the problem is nonlinear, not only because of the plastic deformation, but also because of nonlinear geometric effects. It was observed that nonlinear geometric effects result in redistribution of the loading between bending and membrane reactions of the shell and changes in the deformation modes. Accordingly, a model was developed to include the most important nonlinear effects; the corresponding differential equations were derived and programmed for the CDC-3600 computer. This program, DYPLHX, is now operational, and parameter studies are being performed to determine the effects of pulse shape, intensity, and duration on subassembly deformation. Some preliminary results of these studies are described below.

Consider a hexagonal shell made of a rigid, perfectly plastic material with yield stress σ_y and density ρ , and loaded internally by a time-dependent pressure $P(t)$. The width and wall thickness of a side of

the hexagon are L and H , respectively, and the outward plastic deformation at the center of a side is U_0 . (See Fig. III.A.1, ANL-7753, p. 146.)

Define dimensionless pressure p , time τ , geometric parameter α , and deformation u_0 by

$$p = \frac{P}{P_0}; \quad \tau = \frac{t}{t_0}; \quad \alpha = \frac{H}{L}; \quad u_0 = \frac{U_0}{H}; \quad (1)$$

where

$$P_0 = \frac{\sigma_y H}{L}, \quad \text{and} \quad t_0 = L \sqrt{\frac{\rho}{\sigma_y}}. \quad (2)$$

For an FFTF subassembly can, $\alpha = 0.056$. Its yield stress depends on temperature and irradiation history; for $\sigma_y = 30,000$ psi, $P_0 = 1700$ psi, and $t_0 = 0.4$ msec, and for $\sigma_y = 75,000$ psi, $P_0 = 4200$ psi, and $t_0 = 0.25$ msec.

The first parameter study performed, using DYPLHX to calculate dynamic plastic deformations of hexagonal subassembly cans, was for idealized rectangular pressure pulses of intensity P_m and duration t_1 (corresponding to dimensionless quantities p_m and τ_1). Typical final plastic-deformation results are shown in Fig. II.4 for $\alpha = 0.056$. For large values of τ_1 , the deformation stops while the pressure is still being applied; i.e., the can has deformed sufficiently to contain the applied pressure statically. However, the amount of plastic deformation exceeds that which would be obtained by slowly pressurizing the can.

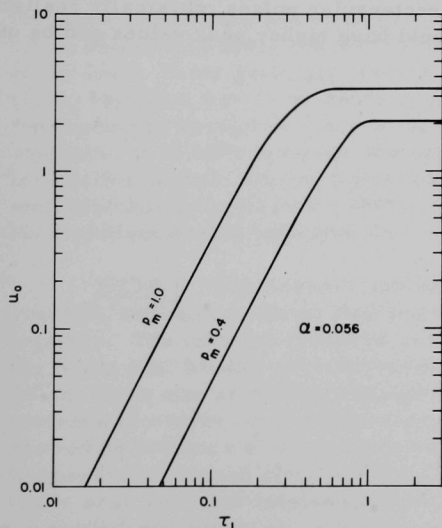


Fig. II.4. Typical Final Deformation (u_0) of Hexagonal Subassembly Can as a Function of Pulse Duration (τ_1) for Two Rectangular-pulse Intensities (p_m). $\alpha = 0.056$

For small values of pulse duration τ_1 , the curves are straight lines with slope 2 on the log-log plot; this implies that u_0 is proportional to τ_1^2 . For a rectangular pulse, the impulse I and its dimensionless counterpart i are given by

$$I = P_m t_1, \quad i = p_m \tau_1. \quad (3)$$

Then for a given α and small τ_1 ,

$$u_0 = i^2 f(p_m). \quad (4)$$

Figure II.5 shows u_0/i^2 as a function of p_m for $\alpha = 0.056$. For large p_m ,

the curve flattens out, so that the plastic deformation at the center of the side of the can becomes approximately proportional to the square of the applied impulse.

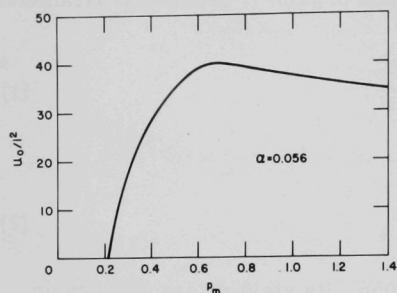


Fig. II.5. Hexagonal-can Deformation (u_0) Divided by the Square of the Impulse (i^2) as a Function of Pressure (p_m) for Rectangular Pulses of Short Duration

The program DYPLHX also calculates the stretching of the sides of the can and the motion of the corners. If u_0 is small, the corners remain essentially stationary; but if u_0 is large, the corners move in as the cross section of the hexagon becomes more rounded. Significant stretching of the sides occurs for large u_0 .

For other structural configurations it was reported* that a rectangular pulse produces more plastic deformation than other pulse shapes having the same impulse and peak value. The same is expected to be true here.

Therefore, parameter studies for other, more physically realistic, pulse shapes will be performed. Equivalent-load parameters to correlate the deformations produced by differing pulse shapes, such as were found for other structural configurations, will be investigated for the hexagonal shell. It is significant that the results shown in Figs. II.4 and II.5 were obtained for idealized rectangular pulses; physically realistic pulses which do the same damage would have higher peak values and be of considerably longer durations.

*C. K. Youngdahl, The Dynamic Plastic Response of a Tube to an Impulsive Ring Load of Arbitrary Pulse Shape, ANL-7562 (Apr 1969); *ibid.*, Load-equivalence Parameters for Dynamic Loading of Structures in the Plastic Range, ANL-7677 (May 1970); and *ibid.*, Correlating the Dynamic Plastic Deformation of a Circular Cylindrical Shell Loaded by an Axially Varying Pressure, ANL-7738 (Oct 1970).

III. INSTRUMENTATION AND CONTROL

A. Instrumentation Development for Instrumented Subassembly T. P. Mulcahey (02-024)

Instruments for in-core measurement of flow, fuel and coolant temperatures, and fuel-pin pressure are being developed consistent with requirements defined by the EBR-II Instrumented Subassembly test program. Development encompasses instrument design, performance analysis, fabrication, and tests leading to specifications and quality-assurance procedures for procurement from commercial vendors.

1. Fuel-pin and Coolant Thermocouples. A. E. Knox (Last reported: ANL-7845, p. 3.1)

Fuel centerline thermocouples (FCTC) in capsules No. 2 and 7, which were irradiated in EBR-II Test ISA XX01, were removed from their fuel elements and examined visually and electrically with the following results:

FCTC 2: The ceramic insulator of the upper hermetic seal was intact. However, the Kovar feedthroughs of both the upper and lower hermetic seals were broken, probably during disassembly, indicating that the Kovar had become brittle. The ceramic insulator of the lower hermetic seal was cracked, and a metallic deposit on the ceramic bridged the two Kovar feedthroughs. The Niore and copper brazes were slightly degraded. The tantalum sheath was badly cracked in the lower-temperature region (at the top of the fuel). Some grain growth was observed in the high-temperature regions, but there was no evidence of gross tantalum- UO_2 reaction. This thermocouple showed no clear evidence of electrical shorting during reactor operation at 50 MW; however, the output was erratic toward the end of the irradiation period. During operation at this power level, FCTC 2 indicated temperatures from 1220 to 1340°C. Electrical measurements made at the time of disassembly indicated that the thermocouple was not functional.

FCTC 7: The ceramic insulator of the upper hermetic seal was cracked, and the two Niore seal brazes on the Kovar feedthroughs had fused together. The ceramic insulator of the lower hermetic seal was intact, but the Niore seal brazes were degraded. The tantalum sheath was in good condition; there was some grain growth in the high-temperature regions, but no evidence of cracks or gross tantalum- UO_2 reaction. This thermocouple also showed no evidence of shorting during operation at reactor power; indicated temperatures ranged from 1170 to 1270°C. After removal of the upper hermetic seal, loop and insulation measurements indicated that the thermocouple was still functional.

B. FFTF Instrumentation Development. R. A. Jaross (02-025)

Prototypes of permanent-magnet, eddy-current, and magnetometer probe-type flowsensors are being designed, fabricated, and flowtested to establish detailed specifications and design for the FFTF permanent-magnet probe-type flowsensor, and to provide technical guidance to ensure competence in commercial fabrication of probe-type flowsensors. Supporting tests are conducted to determine long-term thermal effects on permanent-magnet materials of interest, and to study the effects of simulated fission-gas release on flowsensor response.

1. Permanent-magnet Probe-type Flowsensors. F. Verber (Last reported: ANL-7833, p. 3.1)

Table III.1 summarizes the average percentage changes that have occurred in the magnetic field strength of Alnico V and VIII magnet samples

TABLE III. 1. Thermal Stability of Alnico V and VIII Magnets
after 6000 hr at 700-1200°F

| Alnico V | | | Alnico VIII | | |
|-------------|--------------|-----------------|-------------|--------------|-----------------|
| Temp, °F | L/D Ratio | Avg. Chg., % | Temp, °F | L/D Ratio | Avg. Chg., % |
| 700 | 1 | - 5.3 | 900 | 1 | + 9.0 |
| | 2 | - 0.6 | | 2 | + 8.3 |
| | 4 | + 2.7 | | 4 | + 7.6 |
| 800 | 1 | + 0.3 | 1000 | 1 | +26.3 |
| | 2 | + 1.3 | | 2 | +16.7 |
| | 4 | + 2.8 | | 4 | +15.4 |
| 900 | 1 | + 3.8 | 1100 | 1 | + 4.2 |
| | 2 | + 2.4 | | 2 | + 2.2 |
| | 4 | + 5.2 | | 4 | - 1.4 |
| 1000 | 1 | +13.3 | 1200 | 1 | -72.4 |
| | 2 | + 7.3 | | 2 | -66.1 |
| | 4 | + 8.5 | | 4 | -52.8 |
| 1100 | 1 | -38.3 | | | |
| | 2 | -24.3 | | | |
| | 4 | -16.8 | | | |

after 6000 hr. These samples are undergoing fundamental thermal-stability tests in an individually heated, multisection, high-temperature oven. The measurements are made at room temperature, and the values listed represent the average of five samples for the specific temperature and L/D ratio.

A comparison with previous data (see Table III.1, ANL-7833, p. 3.2) shows there is no leveling off of the trends established earlier. Analysis of the reference magnet data indicates that the drift in the instrumentation has been less than 0.5%, and random errors for individual samples are no more than 1%.

2. Magnetometer Probe-type Flowsensors. D. E. Wiegand (Last reported: ANL-7845, p. 3.2)

A third magnetometer flowsensor (MFS-3) was fabricated and is currently being tested in the thimble of the Annular Linear Induction Pump (ALIP) test loop, which has a maximum operating temperature of 1000°F. This flowsensor contains Alnico VIII H magnets, a fluxgate with ceramic-insulated gold wire coils and a strip core of Hiperco 27, and has the dimensions and configuration of an electromagnet-excited sensor for tests at higher temperatures.

In earlier tests on Magnetometer Flowsensor No. 2 (MFS-2) in the ALIP loop (see ANL-7776, p. 17), a high ambient field in the region of the flowsensor was suspected. This was confirmed by observing the changes in field reading as MFS-3 was inserted into the thimble. For example, with the sensor inserted to the end of the thimble, readings of +5.88 and +6.29 G were obtained with the sodium flow on and off, respectively. With the sensor withdrawn 1 in., the corresponding readings were -2.57 and -2.13 G; at 2 in., the readings were -6.82 and -6.39 G.

An attempt was made to compensate for the ambient field in a region of low gradient by adjusting the flowsensor off balance. However, attempts to obtain a null in the net field by adjusting the position of the sensor in the thimble were unsuccessful because of the extreme sensitivity of the adjustment (particularly, with gloved hands).

The ambient fields and gradients are attributed to a permanent-magnet electromagnetic flowmeter located on an adjacent run of pipe within a few inches of the test thimble. Provision of a micrometer adjustment on the magnetometer flowsensor position would not have solved the problem, since small relative motions between the two runs of pipe would cause variations in the unbalanced condition.

The possible effects of the ambient field conditions without compensation are made especially severe because of the low sodium velocity in the

test annulus (2.3 ft/sec under normal conditions) and the small flow area, which result in a flow signal of only 0.22 G. In an extended flow region and sodium velocity of 10 ft/sec, the same sensor would provide a signal of 12 G.

As of July 28, 1971, MFS-3 has accumulated 336 hr of operation, mostly at the maximum loop temperature. The sensor appears to be operating despite a low insulation resistance ($\sim 5000 \Omega$); this is attributed to the deteriorated (aged) ceramic cement employed in fabricating the coil. (A fresh supply of Ceramabond 503 has been purchased and will be used in future coils.)

The ratio of flow-velocity values from MFS-3 to those obtained from the conventional electromagnetic flowmeter in the ALIP loop was found to vary from 1.00 to 1.13. The random nature of the variations indicate their source to be in uncontrolled variables in the equipment, rather than aging changes. The generally higher-velocity values from MFS-3 could be the result of strong ambient field disturbances causing spurious magnetometer flowmeter action, which would be sensed by the fluxgate. While the test method successfully compensated for the balance disturbance of the ambient field, a determination of the spurious magnetometer flowmeter action can be made only after termination of the test and removal of the sensor from the thimble.

C. Neutron-detector Channel Development. G. F. Popper (02-138)

Development under contract with industrial vendors is focused on complete neutron-detection channels, including cabling and circuitry to transmit, process, and display information from high- and low-temperature ionization chambers and self-powered detectors in out-of-core and in-core regions of LMFBFR's. Advanced circuitry for intermediate- and wide-range applications, and high-temperature neutron detectors are procured commercially; vendor tests are administered; and parameter determination and operational tests are performed in ANL and EBR-II nuclear-instrument test facilities.

1. Intermediate- and Wide-range Systems. G. F. Popper (Last reported: ANL-7845, p. 3.3)

Preliminary drafts of RDT Standards C15-10: Logarithmic Count Rate Source Range Channel; C15-6: Logarithmic MSV Intermediate Range Channel; and C15-9: MSV Power Range Channel, have been prepared. These drafts will be forwarded to RDT for review and approval.

2. High-temperature Neutron-detector Cable Technology. A. Hirsch and A. E. Knox (Last reported: ANL-7845, p. 3.4)

A Technical Note describing the results of oven tests on the Westinghouse WX-31353-25 cable assemblies to 850°F has been completed.

Negotiations are continuing with Westinghouse to obtain information relating to failure of cable assemblies attached to the WX-30960 fission chambers.

A tool for the end-trimming of cables has been designed, fabrication drawings prepared, and fabrication started. In addition, a glove dry box is being procured. This will allow both cable cutting and end seal application to be performed in a controlled environment.

Draft RDT Standard F3-39: Testing of High-temperature Cable for Nuclear Detectors, was received from RDT approved, with comments. It will be revised accordingly and issued as a Tentative Standard for trial use.

3. NITF Test Program. V. J. Elsbergas (Last reported: ANL-7845, p. 3.5)

The RSN-286 M402 detector, which was installed in the EBR-II O-1 thimble last month, is performing adequately at 110°F. However, the WX-31384 detector, also installed in the same thimble, evidenced an intermittent external connection in the system and has not yielded any valid data. Although the malfunction now appears to be corrected, data from both detectors are being analyzed in an attempt to ascertain the problem with the WX-31384 detector.

Fabrication of the holders for the WX-30950 Compensated Ionization Chambers to be installed in the EBR-II J-2 thimble is 75% completed. Radiographs indicate that the cables supplied for these detectors are coaxial.

D. Advanced Technology Instrument Development
T. P. Mulcahey (02-096)

New and unique instrumentation is being developed to diagnose performance and detect abnormalities in LMFBR cores. Included are sensors and techniques for acoustical detection of sodium-coolant boiling, monitoring of flow-rate-related phenomena that could detect imbalances between cooling and power, and the measurement of vibrations that might disturb overall reactor stability.

1. Acoustic Surveillance. T. T. Anderson

a. Development of High-temperature Detector. A. P. Gavin (Last reported: ANL-7845, p. 3.5)

Sensors HT-6-2 and HT-6-3 have accumulated 45 days of exposure in an air furnace at 1200°F. During this period, the effects of varying the composition of the internal atmosphere in these units have been evaluated.

After various flushings with helium, argon, and oxygen on July 15, sensor HT-6-2 was pressurized with oxygen to 600 mm Hg abs and the vent tube was valved off. A pressure gauge was attached to the vent tube on the sensor side of the valve, making the total volume of the closed system approximately 5 cc. In 24 hr, the pressure decreased rapidly to 435 mm Hg, and then decreased at a rate of less than 30 mm per day by the end of the month. This test will be continued to determine if the pressure stabilizes before the sensor resistance drops or if a continuous supply of oxygen is required.

The vent tube of sensor HT-6-3 was sealed off without a pressure gauge at the same time that HT-6-2 was sealed. Both units have since retained their maximum resistance and response characteristics at 1200°F (24,000 Ω for HT-6-3 and 34,000 Ω for HT-6-2).

Preparations are being made to conduct similar furnace tests of other sensors at 1000°F.

Fabrication has started on a sensor to be attached to the fuel-assembly holddown member of the CCTL. Plans are to have this sensor in place during testing of the FFTF Mark-IIA fuel assembly.

- b. Development of Acoustic Waveguides. T. T. Anderson (Last reported: ANL-7845, p. 3.6)

A superstructure, consisting of two levels of framework and catwalks, has been added to the 5½-ft-dia, 11-ft-high water-filled tank for the purpose of suspending candidate waveguides into the tank for testing. Checkout of the facility is nearing completion.

By a combination of techniques, sound waves can be produced in the tank for the frequency range 1 to 100 kHz. Low-frequency measurements (100 Hz-1 kHz) can be performed in a USN-type G19 hydrophone calibrator. By using servo-slave techniques, the upper frequency limit has been raised to 10 kHz.

A request for approval in principle for insertion of a waveguide and an acoustic sensor into the bulk sodium of EBR-II has been forwarded to RDT. Design of a shield plug to facilitate this insertion has been initiated.

IV. SODIUM TECHNOLOGY

A. On-line Monitoring and Sampling for Sodium Systems (02-607)

1. National Meter Program. P. A. Nelson (Not previously reported)

Argonne National Laboratory (ANL) is coordinating, as well as participating in, a national program for developing, testing, and establishing commercial availability of meters for use in Fast Fuel Test Facility (FFTF) and in other LMFBR systems. The meters to be developed and characterized in this program are monitors for oxygen, carbon, and hydrogen impurities in sodium and a leak detector for steam generators. Meter modules that provide flow and temperature control are being developed for FFTF.

In preparation for installation of meters and meter modules at FFTF, six RDT standards have been prepared. These have been reviewed by FFTF and potential vendors and have been submitted to the AEC Division of Reactor Development Technology for approval. The standards are as follows: RDT C8-5, Electrochemical Oxygen Meter for Service in Liquid Sodium; RDT C8-6, Hydrogen Meter for Service in Liquid Sodium; RDT C8-7, Diffusion Carbon Meter for Service in Liquid Sodium; RDT C8-8, Specimen Equilibration Device for the Analysis of Nonmetals in Liquid Sodium; RDT E8-13, Oxygen-Hydrogen Meter Module for Service in Liquid Sodium; RDT E8-14, Carbon Meter-Equilibration Module for Service in Liquid Sodium.

2. Oxygen Meters. J. T. Holmes (Last reported: ANL-7825, p. 4.1)

The immediate objective of this program is to establish the performance of an improved, commercially available electrochemical oxygen meter by early FY 1972. The meter, intended for use at FFTF, uses an improved solid electrolyte tube (thoria-7.5 wt % yttria) and a gas reference electrode. ANL is participating in the performance characterization and field testing of these meters and also is responsible for coordinating the efforts of the other contractors in the program, principally HEDL, Westinghouse, and the Zirconium Company of America (Zircoa).

Zircoa had produced 200 electrolyte tubes to HEDL process specifications and had shipped them to HEDL by the end of June 1971. Samples from the first two shipments (70 tubes) have been evaluated and performance-tested by HEDL and Westinghouse and found acceptable. Twenty of these tubes have been selected for use by ANL and Westinghouse Advanced Reactor Division (WARD) in characterizing oxygen-meter performance over an extended period.

The Zircoa tube samples that have been tested in Westinghouse oxygen meters at WARD and Westinghouse Research Laboratories (WRL) have

continued to show better electrical performance than commercial-purity tubes produced by Zircoa. None of the new Zircoa tubes has failed in sodium, and one tube (No. 4086) has been tested for 1800 hr at 700°F.

To provide a statistically significant measure of the calibration stability of the oxygen meter, 20 FFTF-type meters will be tested: 10 at ANL and 10 at WARD. (Selection of electrolyte tubes for these meters was discussed above.) Initial calibration curves at oxygen levels from <1 to 15 ppm will be determined for all meters at 370°C by the vanadium-wire equilibration method, which measures the oxygen activity in sodium. These calibrations will be repeated after three months of continuous operation at 370°C to determine calibration stability. The temperature coefficients of the meters will be measured at intervals during this period. Testing will continue for about a year, under conditions determined by results during the first three months.

Construction of the apparatus on which the 10 meters will be tested at ANL (Oxygen Meter Rig, OMR) is complete except for electrical wiring and the addition of a sodium reservoir with a 30-gal capacity. This work is expected to be complete by the time the oxygen meters are delivered by Westinghouse.

3. Hydrogen Meters. J. T. Holmes (Last reported: ANL-7825, p. 4.2)

The goals of this program are the design, development, and proof-testing of an on-line hydrogen meter for measuring the hydrogen activity in primary and secondary LMFBF sodium systems. A diffusion-type hydrogen-activity meter is being developed for that purpose. The hydrogen meter can be operated in two modes. The first is a static mode, in which the equilibrium hydrogen pressure above the sodium is measured directly and then related to hydrogen concentration in the sodium by Sieverts' law; the second is a dynamic mode, in which the hydrogen flux through the membrane is monitored by an ion pump.

Recent studies conducted in the Sodium Analytical Loop (SAL) have been directed toward determining the Sieverts' law constant for the hydrogen-sodium system. Sieverts' law is expressed by the relation

$$S = KP^{1/2}, \quad (1)$$

where

S = concentration of hydrogen in sodium, ppm,

K = a constant, ppm Torr^{-1/2} or ppm cm^{-1/2},

and

P = hydrogen pressure, Torr or cm.

The constant, K, was measured by adding known quantities of hydrogen to the sodium and measuring the equilibrium pressures before and after the additions. The results indicated a value for the Sieverts' constant of 18.6 ± 1.3 (2 σ) ppm cm^{-1/2} (5.8 ± 0.5 ppm Torr^{-1/2}) at 450°C.

When the hydrogen meter is operated in the equilibrium mode, as in this experiment, equilibrium pressures are achieved within about 10 min. Thus, the hydrogen meter provides a fast, accurate determination of the hydrogen concentration in sodium.

4. Carbon Meters. J. T. Holmes (Last reported: ANL-7825, p. 4.3)

Present work in this area is being directed toward development of a method for relating the carbon-flux output from the UNC diffusion-type carbon meter to the carbon activity of the sodium. Initially, attempts are being made to correlate flux readings with the carbon uptake of metal specimens also immersed in the sodium. Because of the difficulty in controlling the carbon concentration in a flowing-sodium system, these experiments are being made in a stirred vessel. Scouting experiments are in progress to select appropriate metal specimens for these studies. Candidate materials are nickel, iron-8% nickel, stainless steel, and vanadium.

5. Meter Modules for FFTF. J. T. Holmes (Last reported: ANL-7825, p. 4.3)

The objective of this work is to design, proof-test, and establish commercial availability for on-line meter modules to be installed at FFTF. These modules include the meters for monitoring impurities and the flow and temperature controls required for proper meter operation. Two types of modules are being designed and fabricated: (1) an oxygen-hydrogen meter (O-H) module, containing two oxygen meters (in case one should fail) and a hydrogen meter, and (2) a carbon meter-equilibration (C-E) module, which houses either a carbon meter or a device for equilibrating metal specimens for meter-calibration purposes. Proof-testing will be carried out on laboratory sodium systems and on the Radioactive Sodium Chemistry Loop (RSCL) at EBR-II.

The O-H module to be tested at ANL-Illinois has been installed on the Test and Evaluation Apparatus (TEA), and testing has begun. The second O-H module, console, and the components for Cell B subsystems have been sent to EBR-II, and installation is scheduled for completion early in September.

On startup of the O-H module in TEA, one of the electrolyte tubes proved to be defective and was replaced. Since then, both oxygen meters and the hydrogen meter in this module have operated satisfactorily.

The module is being tested at sensor temperatures of 700, 800, and 900°F with an inlet sodium temperature of 700°F. The sodium in TEA has been cold-trapped at oxygen levels in the range of 0.5-15 ppm and hydrogen levels in the range of 0.05-1.5 ppm. Preliminary tests of the hydrogen meter indicate a concentration of ~0.3 ppm hydrogen at a cold-trap temperature of 160°C. This is in agreement with the solubility of hydrogen in sodium at this temperature. The temperature dependency, expressed as activation energy for permeation of hydrogen through the nickel membrane, was found to be ~13,700 cal/mol over the range of 700-900°F.

Two carbon meter-equilibration (C-E) modules and instrumentation consoles have been fabricated. A side view of a module, before installation

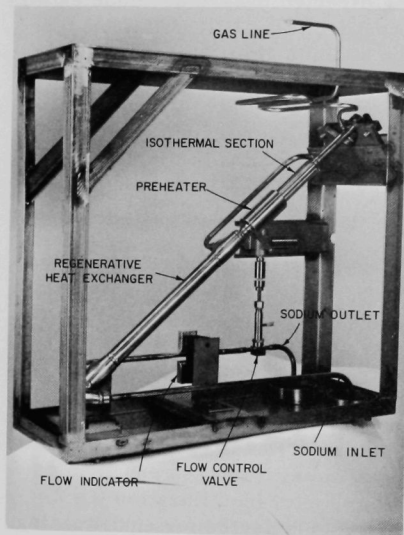


Fig. IV.1. Carbon Meter-Equilibration (C-E) Module--Side View (30 in. high, 32 in. deep, 11 in. wide). ANL Neg. No. 308-2577A.

of heaters and thermocouples, is shown in Fig. IV.1. Final assembly and checkout of the meters and modules are under way. Both units will be used for calibrating oxygen meters by the equilibration of vanadium metal specimens. One will be used on the Oxygen Meter Rig (OMR) at ANL-Illinois (see Sect. IV.A.1); the other will be installed at EBR-II on the RSCL. The data package for installation and testing of the C-E module at EBR-II has been reviewed by an EBR-II safety committee. Installation will begin following approval of the experiment by EBR-II management.

6. Detectors for Leaks in Steam Generators. P. A. Nelson (Last reported: ANL-7825, p. 4.4)

When operated in the dynamic mode, the ANL hydrogen meter can serve as a water-to-sodium leak detector in an LMFBR steam generator. Work has been completed on the fabrication of components for a steam-generator leak detector for the Liquid Metal Engineering Center (LMEC). The sodium hardware, hydrogen-meter vacuum components, and instrument console have been shipped to LMEC. The unit will be installed on the Sodium Component Test Installation at LMEC early in FY 1972.

Before shipment, the instrument console was connected to an argon-hydrogen test system to determine the response of the alarm system to various hydrogen input rates. These tests confirmed that the alarm system operates as expected; i.e., when hydrogen is introduced at a low rate

the alarm set point moves up with the ion-pump signal and no alarm occurs. (The delay time for the set point to follow the ion-pump signal is adjustable.) When hydrogen is introduced at a high rate, the ion-pump signal increases

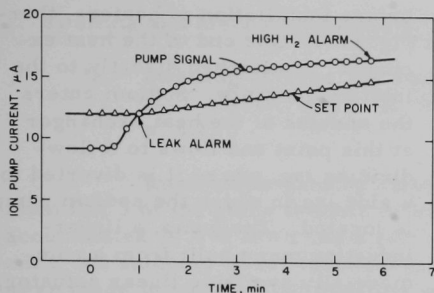


Fig. IV.2. Test of Leak-detector Alarm System (set-point delay: 500-sec time constant)

rapidly and the alarm point is reached before the set point can move upward. Figure IV.2 illustrates an increase in hydrogen level similar to that expected in a steam-generator leak of 5×10^{-4} lb of water per second. The first alarm (leak alarm) occurs when the ion-pump signal exceeds the set point, and the second alarm (high hydrogen alarm) occurs when the ion-pump signal exceeds a fixed-alarm trip point on the recorder (in this example, $16.5 \mu\text{A}$).

A nickel membrane of the

same material and design as the one installed in the leak-detector module has been tested on the Sodium Analytical Loop (SAL) for nearly 2000 hr. Both the membrane and the ion pump have performed as expected for the entire test period. The ion-pump current has been very stable.

Figure IV.3 shows the short-time response of the meter to a rapid change in the system. Since it was not possible to add hydrogen rapidly to SAL, the temperature of the membrane was changed rapidly; such a change would have an effect on the vacuum system similar to that of a rapid change in hydrogen concentration. Increasing the temperature increases the diffusivity of hydrogen, whereas increasing the hydrogen in sodium increases the hydrogen concentration gradient across the membrane. Both mechanisms result in increased hydrogen pressure in the vacuum system.

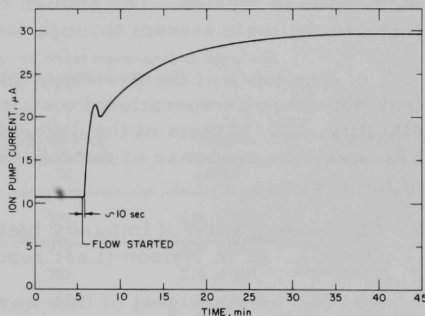


Fig. IV.3. Short-time Response of Leak Detector (temperature, $\sim 450^\circ\text{C}$)

To accomplish the rapid change shown in Fig. IV.3, the sodium flow was stopped for a short time and the upstream temperature (initially 375°C) was raised to 450°C . The flow was then started, and the meter response was recorded. The initial response was almost instantaneous. (The delay of about 10 sec was sodium transit time.) The time required from the initial response to 50% of the total change was about 30-45 sec.

A prototype hydrogen-meter leak detector for the EBR-II secondary sodium system is being installed on the SAL for design-confirmation tests.

The unit consists of a hydrogen-meter membrane and associated vacuum system and a sodium-conditioning system, which includes a heat exchanger, heaters, and a small, linear-induction pump.

The assembled sodium system, before installation of heaters, thermocouples, and insulation, is shown in Fig. IV.4. One end of the heat exchanger is attached directly to the inlet sodium pipe. Sodium enters the annulus of the heat exchanger at this point and flows to a flow-dividing tee, where it is diverted to a side leg in which the sodium pump is located. The pump, a linear-induction pump built from a commercially available linear actuator, has coils capable of operation at 250°C. Flow continues from the pump, back to the flow-dividing tee, and along the annulus to the high-temperature end of the heat exchanger, where the nickel diffusion

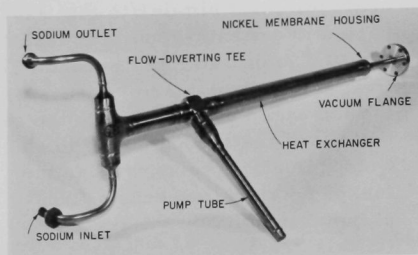


Fig. IV.4. Prototype Leak Detector for EBR-II Secondary Sodium System. ANL Neg. No. 308-2578A.

membrane is located. The sodium then flows past the membrane and returns to the main stream through the center tube of the heat exchanger.

The tests of the prototype unit on SAL will include (1) startup of the leak detector, (2) operational tests to determine thermal performance and stability, and (3) tests of the diffusion of hydrogen through the nickel membrane and the response of the ion-pump to changes in the hydrogen content of the sodium.

7. Characterization of Impurity Meters and Meter Response to Impurity Species. P. A. Nelson (Last reported: ANL-7798, p. 59)

The primary goal of this work is to study the interactions of impurity species and their effects on the impurity-monitoring devices in cold-trapped sodium. The effect of cold trapping on these impurities will be studied as a function of cold-trap operating parameters and procedures. The methods for determining the impurities (O, H, C, and N) in the sodium will be on-line impurity meters, equilibration of metal specimens, and sampling and analysis. Experimental work will be conducted in the Apparatus for Monitoring and Purifying Sodium (AMPS). This sodium system will provide stable but adjustable impurity levels in the sodium fed to the test cold trap.

The design package for AMPS has been completed and reviewed. Some design changes were made as a result of this review, including the addition of pipe anchors, the addition of thermal shields in the dump tank, modification of the trace heating, and reconsideration of the need for thermal protection of the enclosure. Pressure vessels and cold traps are under construction, and system components are being ordered. A detailed test plan for the use of AMPS is being prepared.

V. FUELS AND MATERIALS DEVELOPMENT

A. LMFBR Cladding and Structural Materials1. Swelling and Mechanical Behavior of Cladding Alloys (02-605)

- a. Swelling of Type 304 Stainless Steel. P. R. Okamoto, B. J. Kestel, and S. D. Harkness (Last reported: ANL-7845, p. 5.1)

Immersion-density measurements were performed on samples from flat 3 of the guide thimble of EBR-II safety rod 3A1. The thimble had accumulated 37,490 MWd and a calculated peak total fluence of 1.7×10^{23} n/cm². All samples were electropolished before weighing. Measurements were made in once-boiled distilled water to which Kodak Photo-flo 200 solution was added as a wetting agent. At least four sets of wet and dry weighings were made for each sample. Fractional changes in densities in the irradiated samples were determined on the basis of a density of 7.8991 g for a reference sample located 25.5 in. above the reactor midplane. The results are summarized in Table V.1. The fluence and irradiation temperatures reported are tentative values and are subject to revision upon receipt of additional data.

TABLE V.1. Percent Density Change of Solution-annealed Type 304 Stainless Steel from EBR-II Safety Rod 3A1

| Sample Reference Number | Flat Number | Axial Distance from Reactor Midplane, ^a in. | Irradiation Temperature, °C | Total Fluence, n/cm ² | Density ^b Change, % |
|-------------------------|-------------|--|-----------------------------|----------------------------------|--------------------------------|
| 3A1-238 | 3 | -9.1 | 374 | 6.4×10^{22} | -1.2 |
| 3A1-240 | 3 | -6.1 | 374 | 1.2×10^{23} | -2.0 |
| 3A1-242 | 3 | -3.0 | 385 | 1.6×10^{23} | -3.8 |
| 3A1-245 | 3 | 0.34 | 402 | 1.7×10^{23} | -7.9 |
| 3A1-247 | 3 | 2.7 | 424 | 1.5×10^{23} | -10.5 |
| 3A1-249 | 3 | 5.7 | 440 | 7.4×10^{22} | -8.8 |
| 3A1-251 | 3 | 8.8 | 457 | 3×10^{22} | -3.0 |
| 3A1-253 | 3 | 11.8 | 459 | c | -1.4 |

^aTo center of specimen.

^bBased on a density of 7.8991 determined for a sample located 25.5 in. above the reactor midplane.

^cInsufficient information available.

The maximum observed density decrease was 10.5%, which occurred in a sample 2.7 in. above the reactor midplane. This correlation between the peak in the swelling profile with axial position was also observed in the swelling profile of the guide thimble of EBR-II control rod 5A3 (see ANL-7833, p. 5.1). In both cases, the axial position corresponding to the

maximum density decrease did not correspond to the region of peak fluence, but rather to a region of higher temperature that was exposed to a fluence of about 0.9 of the peak value.

Samples from both safety rod 3A1 and control rod 5A3 have been examined by transmission electron microscopy, and the micrographs are now being analyzed.

b. Theoretical Aspects of Void Formation. S. D. Harkness and Che-Yu Li (Not previously reported)

Recent work on the theoretical aspects of void formation was presented at the Albany Conference on radiation-produced voids. The major points were as follows: (1) The trapping of self-interstitial atoms by substitutional solute atoms may occur at reactor temperatures. Such trapping could sharply reduce void formation and thus help explain the observed sensitivity of swelling to minor solute additions. (2) The swelling rate of a metal is expected to be a maximum when the voids and dislocation structure are equally effective sinks. Cold work, therefore, could increase or decrease swelling rates, although a decrease is more likely. (3) The conditions under which a saturation in void volume occurs have been analyzed for the case in which dislocations intersect the voids. Complete saturation is not expected unless (a) all the dislocations are connected to the voids, (b) the rate of vacancy flow out of the void is sufficiently large to maintain the equilibrium void-dislocation configuration, and (c) the spacing between the voids is sufficiently small to ensure recombination through the dislocation or to limit the extent a dislocation can climb, or both.

Under these conditions, it is expected that the higher the number density of voids the lower the void volume at saturation. Note, however, that this analysis assumes the dislocation loops have unfaulted and glided. Looping unfaulting is calculated to occur in Type 304 stainless steel at about 800 Å, which means that the present analysis is valid for irradiation temperatures in excess of 475°C. Of course, at high doses the analysis should extend to somewhat lower temperatures.

2. Nondestructive Testing Research and Development (02-092)

a. Data-handling System Investigation. C. J. Renken (Not previously reported)

Quality requirements on some fast-reactor components and materials are so strict that nondestructive testing and other quality-assurance procedures account for a considerable portion of the cost of the finished item. Fuel-element jacket tubing can be cited as an example. The direct cost of nondestructive testing of jacket tubing arises from three sources: (1) operating costs of equipment, including labor and maintenance;

(2) capitalization of equipment cost; and (3) cost of "false alarms"--tubing erroneously rejected by the test. Of course, depending upon the method of bookkeeping used, inspection costs included in the purchase price will be much higher than the total of the previously mentioned costs to pay for development and all the fabrication costs necessary to produce some tubing that will pass the nondestructive tests as well as tubing that will not pass. To reduce the cost of nondestructive testing, the equipment should possess the best engineering compromise of the qualities of speed, reliability, accuracy, and simplicity that are possible under the state of the art.

A further reason for high component costs is probably unsophisticated specifications that call for quality levels not necessary for satisfactory service. As additional test data and operating experience become available, specifications should be written that relate to this accumulating knowledge. As an example, current specifications for tubing neglect defect location (inner or outer surface) and orientation with respect to the axis. Rejection is only on the basis of depth; yet steadily accumulating evidence from biaxial-creep burst tests indicates that defect orientation has a pronounced effect on time to failure. If this type of data is eventually reflected in specifications in an effort to reduce cost, nondestructive test equipment will be required that has the capability of recognizing and categorizing a defect according to some function of depth, length, and axial orientation.

Equipment to accomplish this type of test is presently under development. At the current stage of development, the equipment in use is a pulsed electromagnetic system with six channels each using two sample points to produce 12 analog signals with a bandwidth of 0-30 Hz. This six channel system is only used to check the feasibility of the processing routines. Eighteen channels are actually needed to completely inspect a tube at a throughput rate of 2 m/min.

A PDP-8 computer is presently used to accomplish the A-to-D conversion of the analog data to digital form, and, for some simple pre-processing, to increase the effectiveness of the pattern-recognition schemes being used to recognize abnormal conditions in the tubing. The PDP-8 punches out the contents of its memory on paper tape, which is then converted to cards for use in the ANL System 360. Actual pattern recognition is being performed on the large computer, but after an optimum pattern-recognition scheme has been identified for this application, an actual hardware pattern recognizer will be constructed to work in conjunction with the PDP-8.

B. Fuel Properties

1. High-temperature Properties of Ceramic Fuels (02-094)

- a. Plastic Yielding and Fracture of Mixed Oxides. K. J. Daniel and J. T. A. Roberts (Last reported: ANL-7845, p. 5.13)

To date, brittle-fracture data on UO_2 -20 wt % PuO_2 and UO_2 have been obtained with the four-point bend test that uses a rectangular bar-shape specimen.* A more convenient and perhaps more meaningful test would be one that uses a fuel pellet, since fracture data on material representative of that used in irradiation studies are essential to the proof-testing of fuel-performance codes. The so-called "diametral-compression" test** has been used to determine fracture strengths of brittle materials at room temperature. We have extended the useful temperature range of this test to 1000°C using UO_2 pellets.

The diametral-compression test consists of compressing a cylindrical pellet in the direction perpendicular to the axis of the pellet. The stress system generated in the pellet is biaxial. A tensile stress is developed across the loaded diameter and is given by the expression

$$\sigma_1 = \frac{2P}{\pi Dt}, \quad (1)$$

and the minimum compressive stress in the center of the pellet is given by

$$\sigma_2 = \frac{6P}{\pi Dt}, \quad (2)$$

where P is the load, D is the diameter, and t is the thickness of the specimen. To eliminate the possibility of an infinite compressive stress at the point of contact with the pellet, a bearing pad must be used between the pellet and the platens of the compression cage. This distributes the load over a small area without interfering with the maximum tensile stress in the center of the specimen. The correct bearing-pad material (and thickness) must be found experimentally. The criterion used is a correct fracture, i.e., a smooth, straight fracture surface in the center of the specimen.** It was found that different temperature ranges required different pads (see Table V.2).

*R. F. Canon, J. T. A. Roberts, and R. J. Beals, *J. Am. Ceram. Soc.* **54**(2), 105-112 (1971); J. T. A. Roberts and B. J. Wrona, Nature of Brittle-to-Ductile Transition in UO_2 -20 wt % PuO_2 Nuclear Fuel, *J. Nucl. Mater.*, in press.

A. Rudnick, A. R. Hunter, and F. C. Holder, *Mater. Res. Std.* **4, 283-289 (1969).

TABLE V.2. Bearing-pad Materials

| Temperature, °C | Materials |
|--------------------|---|
| RT (25°C) | Computer card (1 thickness) |
| 500-800 | 5-mil-thick copper ^a |
| 800-1000 | 2 sheets of 3-mil-thick nickel ^a |

^aOne-half-mil sheet of mica was inserted between pad and compression cage to prevent reaction with the tungsten.

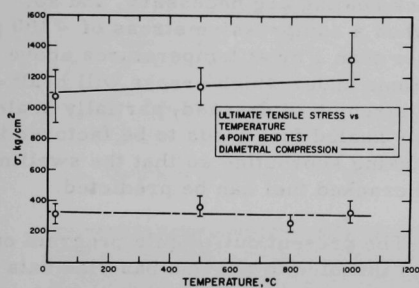


Fig. V.1. Temperature Dependence of Strength of UO_2 . Neg. No. MSD-55270.

The fracture strength of UO_2 pellets (dimensions, 0.25 by 0.25 in.; density, 97% of theoretical; grain size, $\approx 10 \mu$; and O/M = 2.00) was measured from room temperature to 1000°C with a Model TT-DM-L (10,000 kg) Instron testing machine that incorporates a tungsten compression cage. As shown in Fig. V.1, the fracture strength, calculated using Eq. 1, was essentially independent of temperature and was considerably lower than obtained from the four-point bend tests. This

was not unexpected, since it is well documented in the ceramic literature that the brittle-fracture strength is sensitive to the test technique used. Only the tensile test, which is extremely difficult to perform, produces a simple uniaxial stress state in the specimen. The ratio of rupture modulus (obtained from the bend test) to fracture stress (obtained from the diametral-compression test) ranges from 1.3 to 2.9 in other brittle materials.*

It must be concluded, therefore, that the strength of a fuel pellet should be determined using stress conditions similar to those experienced by the fuel in reactor, i.e., a biaxial tensile-stress system, where the hoop stress is the maximum tensile stress. Broughtman *et al.*** have shown that a biaxial tension-compression stress system reduces the brittle strength of alumina and graphite in a manner similar to a biaxial tension-tension stress system. In this respect, the diametral-compression test is more advantageous than the four-point bend test. It is proposed to use this

*A. Rudnick *et al.*, *ibid.*

**L. J. Broughtman, S. M. Krishnakumar, and P. K. Mallek, *J. Am. Ceram. Soc.* 53(12), 649-654 (1970).

technique to determine the relative "tensile" fracture strengths of two types of pellets (closed versus open porosity) fabricated by WADCO.

b. Crack-healing Studies in UO_2 . H. Vander Plas and J. T. A. Roberts (Not previously reported)

Oxide fuels are inherently brittle, and cracking is extensive in reactor as a result of the generation of thermal stresses during startup, shutdown, or power-transient conditions. During steady-state operation, however, cracks heal. For example, Bain* found that cracks deliberately introduced into UO_2 and ThO_2 -2 wt % UO_2 pellets healed in reactor at temperatures $\gtrsim 0.55T_m$ (T_m = melting temperature). The indications were that cracks healed to the limit of the grain-growth region, but the mechanism(s) of crack healing and the influence of temperature, time, stress, and neutron flux were not determined. The problem of crack healing has been made more acute by the recent introduction of a fuel-cracking subroutine into LIFE-II.** Certain conditions for crack healing are necessary, and so, arbitrarily, cracks are made to heal when a compressive stress of $\gtrsim 100$ psi is sustained in the fuel region for longer than 1 hr at temperatures above $0.55T_m$. Obviously the range of conditions under which cracks will heal needs to be evaluated. In addition, the strength of cracked, partially healed, and fully healed fuel needs to be factored into the cracking subroutine so that the swelling rate of cracked fuel can be predicted.

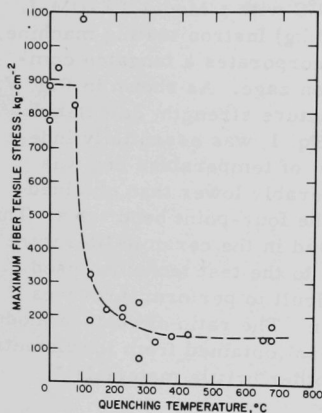


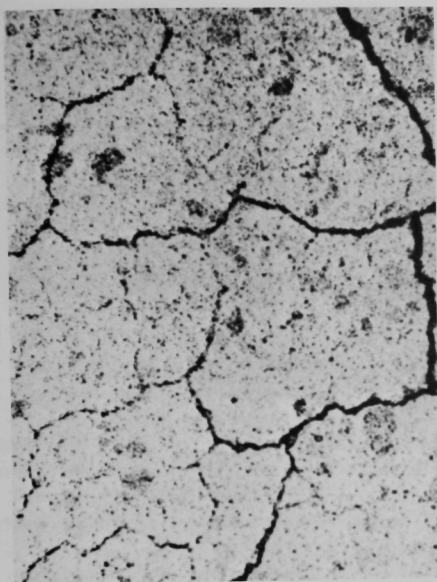
Fig. V.2. Strength as a Function of Quenching Temperature. Neg. No. MSD-55271.

The present out-of-pile program on UO_2 was initiated to provide baseline data on crack healing in oxide fuels that could be used in the design of critical in-pile experiments. The first step was to produce thermal-shock cracks in a bar specimen that could then be tested in four-point bending. The extent of cracking was determined by measuring the bend strength after quenching from various temperatures into water at room temperature. The effect of quenching temperature on strength is shown in Fig. V.2. The behavior of UO_2 is similar to other oxide ceramics such as Al_2O_3 .† The fracture stress of specimens quenched from $\gtrsim 100^\circ\text{C}$ is approximately constant. In the temperature range 125 - 250°C , the fracture strength has a much reduced value, with a minimum at quenching temperatures $\gtrsim 300^\circ\text{C}$. The almost instantaneous decrease in strength corresponds to the first

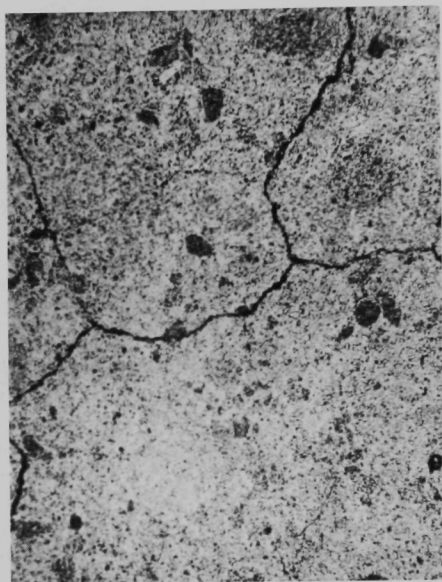
* A. S. Bain, AECL 1827 (1963) and AECL 3008 (1967).

** V. Z. Jankus and R. W. Weeks, "LIFE-II--A Computer Analysis of Fast-reactor Fuel-element Behavior as a Function of Reactor Operating History," to be presented at 1st Intl. Conf. on Structural Mechanics in Reactor Technology, Berlin, Sept 20-24, 1971.

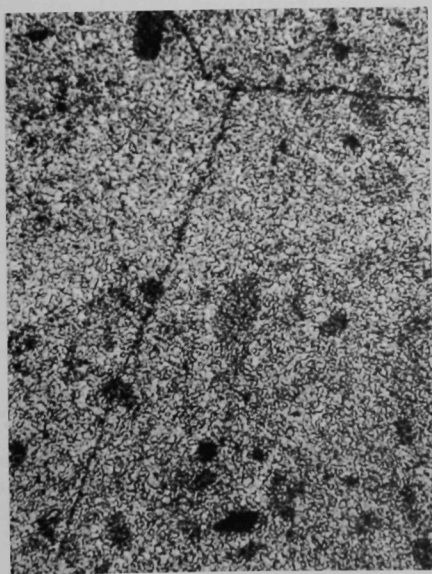
† R. W. Davidge and G. Tappin, Trans. Brit. Ceram. Soc. 66(8), 405-422 (1969).



A. Quenching Temperature = 650°C



B. Quenching Temperature = 425°C



C. Quenching Temperature = 150°C

Fig. V.3

Thermal Shock-cracking Characteristics in UO_2 . Mag. 100X. Neg.
No. MSD-55215.

appearance of cracks in the quenched specimens. The strength is relatively independent of quenching temperature up to 700°C , indicating that the crack depth must remain constant. [Fracture strength is determined by the equation $\sigma_F = (2E\gamma/\pi C)^{1/2}$, where E is Young's modulus, γ is surface energy for fracture, and C is critical crack size.] However, as is shown in Fig. V.3, the number and widths of cracks increase with an increase in quenching temperature. Preliminary healing experiments have shown that the severity of the shock treatment affects the rate at which strength is regained.

2. Thermochemical Properties of Reactor Fuels. A. D. Tevebaugh and P. E. Blackburn, CEN (02-162)

a. U-Pu-O and U-Pu-O-Na Phase Diagram and Kinetic Studies. P. E. Blackburn (Last reported: ANL-7825, p. 5.24)

The study of the U-Pu-O phase diagram is being delayed so that a study can be made of the reaction of liquid sodium with uranium-plutonium mixed oxides. Because of the possible inadvertent reaction of sodium coolant with reactor fuel, it is important to determine the potential severity of the problem and whether it can be avoided.

The initial studies are being made with mixed oxides with a Pu/(U+Pu) ratio of 0.20. The product of the reaction at 900°C was previously identified as Na_3MO_4 , where M represents $\text{U}_{1-y}\text{Pu}_{1-y}$ (see ANL-7825, p. 5.24). Because the Na_3MO_4 phase is only about half as dense as the mixed-oxide phase, the formation of Na_3MO_4 can cause swelling. An example of this is shown in Fig. V.4, a photomicrograph taken of the interior of a sintered pellet which had been exposed to sodium at 900°C . It is apparent that sodium penetrated the pellet along a preexisting crack and reacted with the adjacent mixed oxide to form Na_3MO_4 . Apparently, this process expanded and lengthened the crack, thus spreading the reaction.

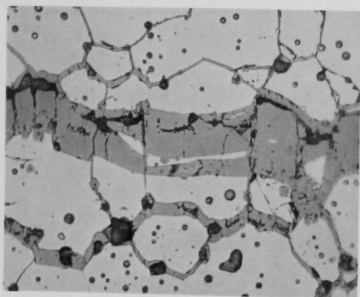


Fig. V.4. Na_3MO_4 Phase Formed along Crack in Interior of Mixed-oxide Pellet Exposed to Sodium at 900°C for 2 days; As-polished. Mag. 300X. ANL Neg. No. 308-2571.

When the pellets are relatively dense and free of cracks, the reaction product has been observed to form almost entirely at and near the surface of the pellets. An example of a surface reaction layer formed at 900°C is shown in Fig. V.5. Similar reaction layers have been observed at the surfaces of pellets exposed to sodium at 500, 600, 700, and 800°C . A further study of the kinetics of the reaction of sodium with sintered mixed-oxide pellets is being made.

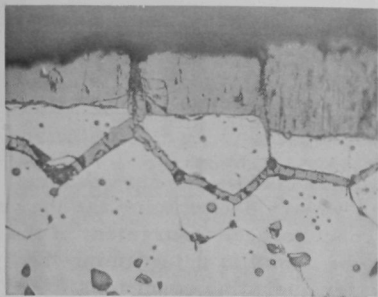


Fig. V.5

Na_2MoO_4 Layer Formed on Surface of Mixed-oxide Pellet Exposed to Sodium at 900°C for 2 days; As-polished. Mag. 300X. ANL Neg. No. 308-2572.

are examined by X-ray diffraction, and the lattice parameter of the product mixed-oxide phase is determined. From a previously established calibration graph of lattice parameter versus O/M composition for the mixed-oxide phase, the O/M composition of the mixed-oxide phase in the product mixture is established. The data obtained to date under presumably equilibrium conditions are shown in Fig. V.6. The reaction times used at these temperatures were 0.17 day at 1100°C , 3 days at 900°C , and 7 days at 800°C ; to reach equilibrium at 500°C , a capsule was first held at 900°C for 3 days and then held at 500°C for 14 days. Some data, which obviously represented nonequilibrium conditions, were obtained in single-stage runs below 800°C . For example, after a reaction of 8 days at 600°C , the O/M composition of the product mixed-oxide phase was 1.987. The data shown in Fig. V.6 indicate that the equilibrium O/M ratio is not very temperature-dependent.

Additional studies are being made with mixed oxides with $\text{Pu}/(\text{U} + \text{Pu})$ compositions of 0.10 and 0.30. After the reaction of the powders with sodium, data analogous to that shown in Fig. V.6 will be established by the lattice-parameter method.

The O/M composition of the mixed-oxide phase, $\text{Pu}/(\text{U} + \text{Pu}) = 0.20$, in equilibrium with sodium and the Na_2MoO_4 phase is being determined. This is important to establish, because mixed oxide with an O/M composition equal to or less than the equilibrium value could not react with sodium that has a low oxygen content. For this study, the initial mixed oxide has an O/M composition of 1.99₅ and is in the form of a fine powder, 43% of which is -270 mesh. The powder is reacted with sodium at various temperatures in welded-shut nickel capsules. After the reactions, the capsules are cut open and the free sodium is removed by dissolution in ethyl alcohol. Portions of the powders

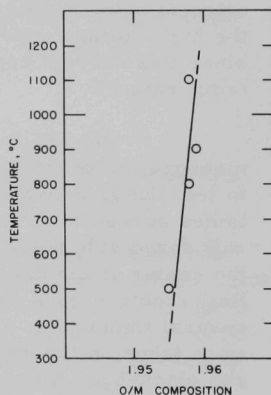


Fig. V.6

O/M Composition of Uranium-Plutonium Mixed-oxide Phase, $\text{Pu}/(\text{U} + \text{Pu}) = 0.20$, from Lattice Parameter Measurements, after Reaction with Sodium in Nickel Capsules

3. Physical and Chemical Studies--Molten Fuel, Cladding, and Coolant.
A. D. Tevebaugh and M. G. Chasanov, CEN (02-175)

a. Thermal Diffusivity for Solid and Liquid Reactor Materials.
M. G. Chasanov (Last reported: ANL-7825, p. 5.25)

To aid in evaluating means of safely cooling the core of an LMFBF in the event of a meltdown incident, we are determining the thermal diffusivity of UO_2 in the liquid state. Our concurrent measurement of the thermal conductivity of liquid UO_2 will also be useful in determining the temperature distribution in the clad fuel under operating conditions.

The thermal diffusivity will be determined from the phase change in a thermal wave produced by heating the sample with a sinusoidally modulated electron beam. Recent work has been directed toward preparation of samples and testing of the electron-beam guns. A tungsten cell has been welded successfully with a UO_2 disk inside. The defective deflection system (due to shorts in the wire leads to the upper electron gun) has been repaired. Three bridge-type rectifiers have been received, and two have been installed and tested. One is being used in the grid-modulation circuit; the other is being used in the lower-gun grid control. A change was made in the high-voltage trip-out circuit to allow both guns to operate at 300 mA, since this current capability is necessary to obtain the higher sample temperatures.

Several tungsten disks were used to test the electron guns and measure temperature profiles. One disk was used with the top gun only to test the grid-modulation procedure. The thermal-diffusivity value obtained agreed favorably with the literature. A tungsten black-body disk with three side holes was prepared; the holes, two of which extended to the center of the disk, were used to determine the true surface temperature. Both electron guns were used to provide uniform heating of the disk at several temperatures. Simultaneous readings, using two optical pyrometers, were taken on the upper surface and at one of the holes to relate the surface and black-body temperatures. A window correction was applied to the pyrometer readings to obtain the black-body temperature.

The results of several temperature-profile measurements indicated that the empty diffusivity cell could be tested up to 2500°C . The thickness of the 1-in.-dia, 0.155-in.-thick empty cell had increased by 3%. Above 2500°C , a significant temperature spread developed. The temperature spread was decreased by increasing the peripheral-scan dwell time with a Zener-diode clipping circuit. In a subsequent test, at 2962°C , convex buckling occurred on top and bottom surfaces, which increased the center thickness about 33%.

To achieve the temperature necessary for testing the diffusivity cell, both guns were operated at 300 mA, which is the maximum meter

reading per gun. The maximum center sample temperature may have to be about 3200°C in order to obtain a completely molten UO_2 sample. At the higher temperatures (2500-3200°C), the cell diameter will be reduced from 1 to 0.75 in. This will decrease the radiating surface by 43%, allowing operation with an improved temperature spread and also at a lower power level. The decreased temperature differential will decrease the buckling forces on the surface, and the smaller size will have greater surface strength for the same wall thickness.

Concurrent with the experimental activities, a theoretical examination of the thermal-conductivity experiment is being made. The first step in the analysis is the evaluation of Cowan's work,* and the substitution of our boundary conditions in his equations. New equations will be developed to describe our two-gun system with a composite tungsten- UO_2 sample since Cowan's work was an idealized treatment of a one-component system. A computer program has been written for the solution of Cowan's equations and will give the phase shift and amplitude as a function of position in the sample. The objective is to determine the minimum temperature spread for the cell, which will result in a negligible interfering phase shift due to peripheral tungsten conduction. This information will allow optimization of cell design and provide reliability for the experimental measurements.

C. Fuel Elements

1. Behavior of Reactor Materials (02-086)

- a. Oxide-fuel Swelling Mechanisms and Models. B. J. Makenas and R. B. Poeppel (Last reported: ANL-7833, p. 5.8)

The Gas Release And Swelling Subroutine (GRASS) code has been used to calculate the behavior of fission gas in irradiated mixed-oxide fuel following an accident in which the sodium coolant is lost. The model is initially supplied with normal operating conditions and a density corresponding to a given atomic-percent burnup. Fuel porosity is assumed to consist entirely of free bubbles with radii of approximately 100 Å, which is characteristic of the unrestructured region. The surface temperature is then instantaneously increased, while the linear power is simultaneously decreased. GRASS then calculates the isothermal behavior of the fuel. Percent swelling is computed as a function of time following coolant loss.

Fuel irradiated to both 2 and 3 at. % burnup and with surface temperatures elevated to 2500, 2700, 2900, and 3200°C was modeled. At the two highest temperatures, the fuel was assumed molten. For molten fuel, GRASS assumes a lower hydrostatic stress and neglects consideration of dislocations and grain boundaries.

*R. D. Cowan, LA-2460 (1960).

In addition to the isothermal calculations, GRASS was also used to compute swelling during the temperature-transient type of accident (typical of a flow coastdown) for fuel at 2 at. % burnup. In this case, the surface temperature was allowed to increase from 750 to 3000°C in about 13 sec. Material above 2800°C was assumed molten. Fuel temperatures and temperature gradients, as a step function of time supplied to the model as data,* were used instead of the values normally calculated by the fuel-temperature subroutine. Total percent swelling was computed by GRASS at each temperature step of the coastdown. Comparisons were also made using various values of hydrostatic stress in the material.

Fuel swelling for both of these studies is shown as a function of time in Fig. V.7. Each is for a fuel at 2 at. % burnup. A hydrostatic stress of 10 atm was used for solid fuel and 2.5 atm for fuel above the melting point.

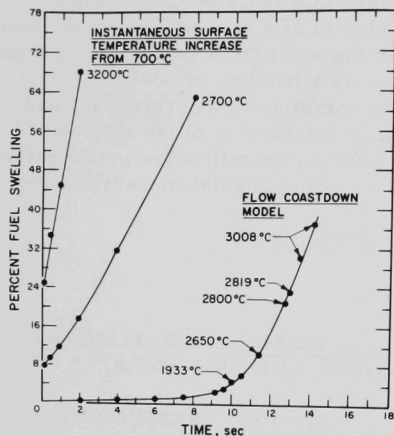


Fig. V.7. Percent Fuel Swelling as Predicted by GRASS Code for a 2 at. % Burnup vs Time, following Sodium-coolant Loss, Neg. No. MSD-55330.

- b. Fuel-Fission-product-Cladding Interactions.
P. S. Maiya, D. E. Busch, and J. E. Sanecki (Last reported: ANL-7833, p. 5.9)

Previously it has been shown (see ANL-7833) that the depth of penetration of stainless steel cladding by cesium depends strongly on the oxygen potential of the cesium. Inasmuch as the oxygen potential can be related directly to the oxygen-to-metal (O/M) ratio of the fuel, it is observed that enhanced cladding penetration occurs at a critical oxygen potential corresponding to a fuel O/M ratio of 2.002. Little cladding penetration by cesium is expected in

a fuel whose O/M ratio is ≤ 2.001 . Several of the assumptions made in relating the oxygen potential of cesium to that of the oxide fuel remain to be examined. These observations and also the reported increase in the oxygen content of irradiated Type 304 stainless steel cladding (see ANL-7825, p. 5.34) are consistent with the mechanism proposed earlier (see ANL-7825, p. 5.28).

Another important variable expected to influence the rate of fission-product-cladding attack is the quantity of volatile fission products that collect at the fuel-cladding interface. A series of experiments has

*Data obtained from W. R. Bohl, ANL (Reactor Analysis and Safety Division).

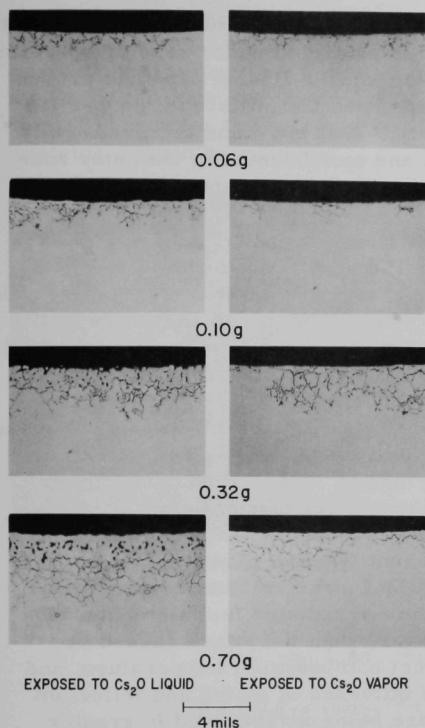
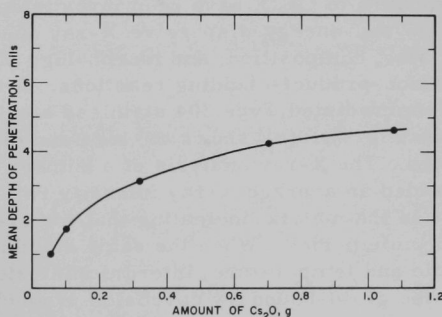


Fig. V.8. Effect of Different Amounts of Cesium Oxide on the Depth of Penetration in 20% Cold-worked Type 316 Stainless Steel. Exposed for 120 hr at 690°C . As-polished. Neg. No. MSD-55122.

been performed in which 20% cold-worked Type 316 stainless steel was exposed to different amounts of Cs_2O for 120 hr at 690°C . Intergranular penetration occurred in cladding exposed to both liquid Cs_2O and its vapor. Figure V.8 shows a series of cladding microstructures after exposure to Cs_2O and its vapor. It was observed that the depth of penetration increases with an increase in the amount of Cs_2O introduced into the test capsule, which had a volume of 1 cm^3 . A plot of mean penetration of the austenitic stainless steel exposed to liquid Cs_2O versus amount of Cs_2O (see Fig. V.9) shows a correlation between the depth of attack and the amount of Cs_2O . The explanation for this penetration dependence on the amount of Cs_2O , when the amount of Cs_2O is small, appears to be due to the formation of stable chromates or molybdates that lower the activity of Cs_2O . The rate of cladding attack shown in Figs. V.8 and V.9 is greater than in mixed-oxide fuel elements irradiated in EBR-II. This is expected, because the total quantity of cesium produced per 10 at. % burnup in a 12-in. column of mixed-oxide fuel (total volume $\approx 7.3\text{ cm}^3$) is

Fig. V.9

Intergranular Penetration of 20% Cold-worked Type 316 Stainless Steel Exposed to Different Amounts of Cesium Oxide at 690°C for 120 hr. Neg. No. MSD-55082.



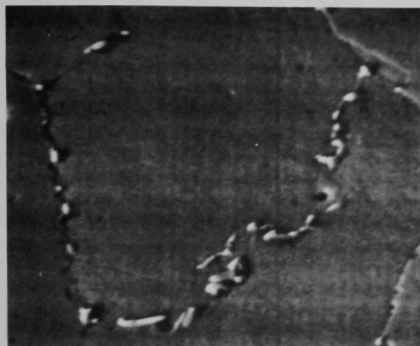
approximately 0.33 g. Also, the oxygen potential of cesium obtained in out-of-pile experiments is higher than that encountered under reactor operating conditions. Furthermore, the quantity of volatile fission products present at the fuel-cladding interface may depend upon the initial fuel properties such as fuel density. It has been reported* that low-density mixed-oxide fuels contain 10 times as much cesium and molybdenum in the outer zone adjacent to the cladding than the high-density fuel operated at comparable power densities.

The postirradiation examination of fuel elements at ANL has established the presence of both cesium and molybdenum at the fuel-cladding interface and in the grain boundaries of the cladding. The X-ray intensity ratios of molybdenum to cesium have been measured in several regions of fuel element C-11, which was irradiated at a peak linear power rating of 12 kW/ft to 10.9 at. % burnup. The results show that the relative composition of cesium and molybdenum in the phases at the fuel-cladding interface and in the Type 316L stainless steel grain boundaries varied from almost pure cesium oxide to almost pure molybdenum oxide. Two preliminary corrosion tests made on Type 316 stainless steel cladding (20% cold-worked), one exposed to MoO_3 and another exposed to Cs_2O -50 wt % MoO_3 for 120 hr at 690°C , have revealed different types of cladding attack. The type of cladding attack by Cs_2O -50 wt % MoO_3 was both uniform and intergranular, similar to that observed in some irradiated fuel elements. The rate of attack in both cases was less severe than the attack caused by Cs_2O alone. The effect of fission-product composition, temperature, and oxygen partial pressure, as well as the influence of iodine and tellurium on the reaction rate and mechanisms, are being investigated in greater detail.

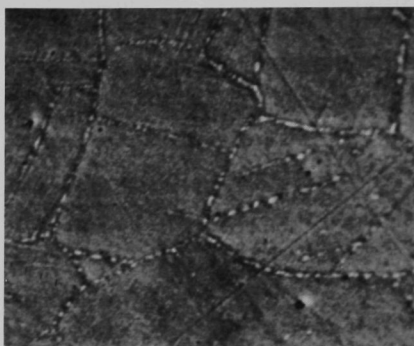
Precipitation reactions occur in austenitic stainless steel (Types 304 and 316) at normal cladding operating temperatures, and the steel becomes sensitized with time. The grain-boundary phases in Type 304 stainless steel (EBR-II grade) annealed at 690°C for 72 hr, with and without exposure to Cs_2O , have been investigated by using scanning electron microscopy and energy-dispersive X-ray analysis to establish the possible roles of size, composition, and morphology of the precipitates in influencing the fission-product-cladding reactions. A typical scanning electron micrograph of unirradiated Type 304 stainless steel cladding aged at 690°C for 72 hr [see Fig. V.10(a)] shows the size and distribution of intergranular precipitates. The X-ray analysis of a number of grain-boundary precipitates yielded an average X-ray intensity ratio of $\text{Cr}/\text{Fe} = 1.1$, compared with 0.6 in the matrix, indicating that the grain-boundary precipitates are chromium-rich. When the same cladding was exposed to Cs_2O for the same time and temperature, intergranular attack occurred. The X-ray analysis of the grain-boundary corrosion product that contained cesium yielded a

*C. E. Johnson and C. E. Crouthamel, Fuel-Clad Interactions in Mixed-oxide UO_2 - PuO_2 Fuel, Trans. Am. Nucl. Soc. **14**(1), 173 (1971).

Cr/Fe intensity ratio of 1.0, compared with 0.5 in the adjacent matrix. Thus, there appears to be some chromium depletion both in the penetrated grain-boundary region and the adjacent cladding matrix following attack by Cs_2O . Such chromium depletion could result, for example, from the oxidation of chromium to chromium oxide both in the cladding matrix and the austenitic grain boundaries.



(a) Type 304 Stainless Steel
Aged at 690°C for 72 hr



(b) 20% Cold-worked Type 316 Stainless
Steel Aged at 690°C for 120 hr

Fig. V.10. Scanning Electron Micrographs of Precipitates in Austenitic Stainless Steel. Mag. 2000X. Neg. Nos. MSD-55074 and MSD-55079.

In 20% cold-worked Type 316 stainless steel cladding annealed at 690°C for 120 hr, the precipitation is intergranular, but it also occurs along twin boundaries [see Fig. V.10(b)]. The intergranular precipitates in Type 316 stainless steel are smaller than those in Type 304 stainless steel. Analysis of a few precipitates revealed the presence of molybdenum-rich phases. Whether one can relate the less rapid attack of Type 316 by Cs_2O (compared with Type 304) to the difference in composition is not yet known, based on this preliminary study. However, further work should be useful in understanding the interrelationships between the size, composition, and morphology of various precipitate phases and the fission-product-cladding interactions.

- c. Experimental Studies of Swelling Mechanisms. S. R. Pati and H. C. Stevens* (Last reported: ANL-7825, p. 5.31)

(1) Re-resolution of Gaseous Fission Products in Oxide Fuels. UO_2 specimens with three enrichments will be irradiated in CP-5 at fission rates of 10^{13} , 5×10^{13} , and 10^{14} fissions/ cm^3 sec, at 200, 600, 1000, and 1500°C . Specimens will be irradiated to four burnups to determine the effect of burnup on the kinetic solubility of gaseous fission products.

*Engineering and Technology Division.

An irradiation capsule has been designed to study the above variables with a minimum number of in-pile experiments. The principal features of the capsule (shown in Fig. V.11) are: (1) The capsule design allows approximately uniform temperatures to be maintained in specimens that have an order-of-magnitude variation in fission rate, and (2) the capsule can accommodate multiple specimens of each enrichment for irradiation to different burnups. Specimens reaching the target burnup can be removed without changing the position of the other specimens in the reactor. Thus, the effects of irradiation temperature, burnup, and fission rate can be investigated using only four capsules, each of which is designed to operate at a fixed temperature.

The external appearance of the four irradiation capsules will be identical. The capsule consists of an outer aluminum tube that occupies the same volume and position in the reactor vessel as the D₂O thimble used in reactor positions VT-18 and VT-19. Thus no major revisions are necessary in the reactor design to accommodate the capsule.

As shown in Fig. V.11, the capsule has three major internal components: an insulated TZM* heat distributor that positions the specimen containers; a Zircaloy intermediate tube that separates the gas heat-transfer systems; and the three clustered guide tubes that provide access to the specimen capsule positions and the top of the reactor. The UO₂ specimens are contained in an externally threaded TZM container having an outside diameter of 7/16 in. Specimens are fitted closely in the container by properly designed molybdenum shims that allow conduction of heat to the container wall. The container is threaded into the heat distributor, which provides intimate contact for efficient heat transfer to the distributor. During irradiation, specimens reaching target burnups may be removed and replaced with dummy specimens to provide adequate fission heat for maintaining irradiation temperature. Removal of a specimen requires unscrewing of the specimen container from the threaded heat distributor and withdrawal into a shielded container at the top of the reactor.

Instrumentation for the capsule consists of six permanent Chromel-Alumel or tungsten-rhenium thermocouples located in the heat distributor, one replaceable thermocouple located on a specimen capsule, and two neutron detectors located adjacent to the outer aluminum wall. In addition, two tubes, which are used for admitting gas, extend into the bottom of the inner and outer gas chambers. Twelve specimen containers comprise the starting load for each irradiation experiment. Heat generated by fuel and gamma heating is used to maintain the internal temperature of the irradiation rig.

Approximately 2100 W are produced in the UO₂ specimens, and gamma heating adds about 400 W for a total of approximately 2500 W of

*Molybdenum alloy with a nominal composition of 0.5 wt % Ti-0.08 wt % Zr.

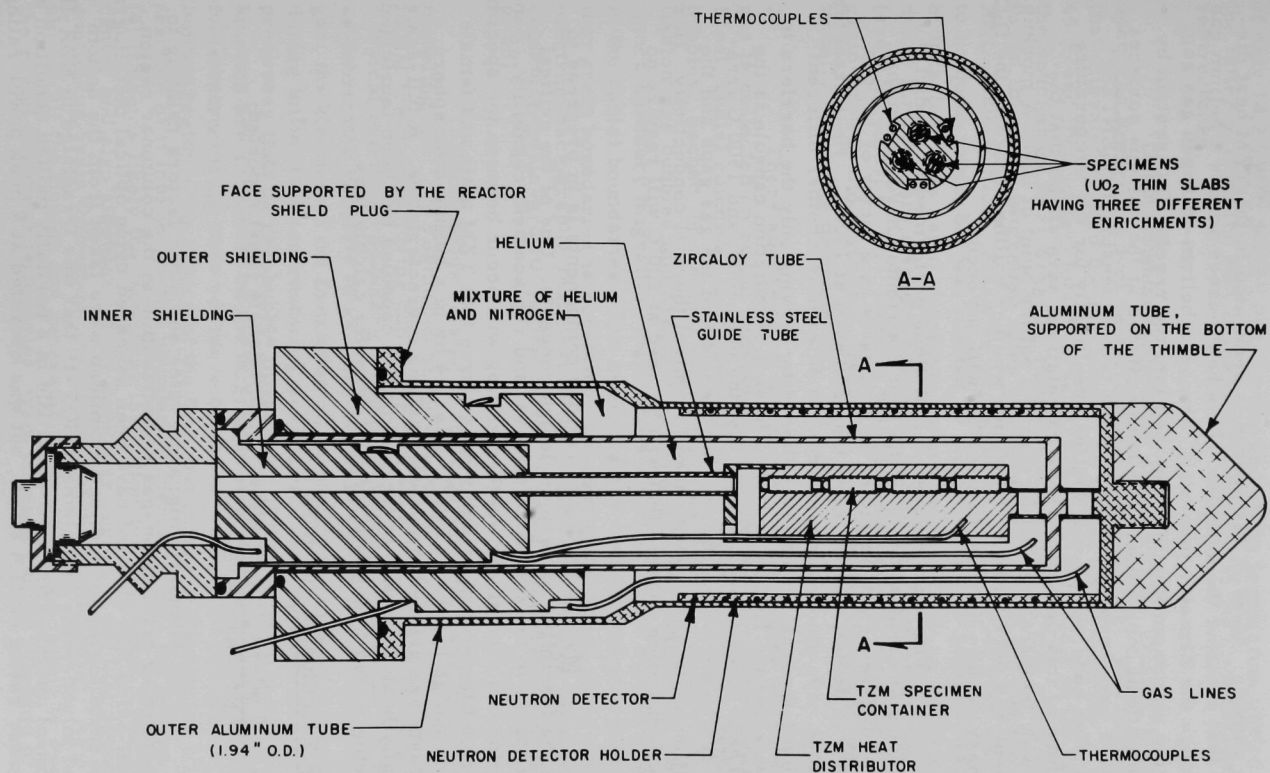


Fig. V.11. Irradiation Capsule for the Study of Re-solution of Gaseous Fission Products. Neg. No. MSD-55169.

heat per capsule. Most of this energy is generated in the TZM heat distributor that contains the samples. This heat passes across a helium gas gap, through the Zircaloy tube wall, across a helium-nitrogen gas gap, through the aluminum thimble, and then into the reactor D_2O system by means of natural convection. The temperatures at the various surfaces of the tubes have been determined by the two-dimensional "GENTEM" heat-transfer code, which was written specifically for the temperature calculations of this capsule. These calculations have shown that the outside-wall temperature will be near the boiling point of D_2O . A mockup experiment was performed to determine whether boiling occurs in the D_2O ; preliminary results indicate that boiling will not occur.

The heat-transfer calculations performed to predict the temperatures at various points in the heat distributor have shown that, in spite of differences in specimen fission rates by a factor of 10, the temperatures do not vary by more than 2%, even at $1500^\circ C$. Heat-transfer calculations have also been performed to determine whether different irradiation temperatures can be obtained by varying only the barriers to heat flow, since the fission heat load in each irradiation capsule is the same. These calculations indicate that the 600, 1000, and $1500^\circ C$ irradiations can be performed by varying the width of the gas gaps and the composition of the gas mixture used to control thermal conductivity. However, the irradiation capsule that will be used at $200^\circ C$ will require no gas gap.

Mockup testing of various components is in progress to evaluate the feasibility of various design concepts. One of the critical design features is the specimen removal and replacement capability. Bench tests performed to evaluate whether galling will occur between the specimen container and the heat distributor have shown that TZM male and female threads do not gall, even at $1500^\circ C$ after 24 hr in a helium atmosphere. Longer tests are planned to evaluate galling characteristics. A full-scale electrically heated mockup of the irradiation capsules has been fabricated and is being tested to confirm the heat-transfer calculations.

2. Oxide Fuel Studies (02-005)

a. Fuel-swelling Studies. L. C. Michels (Last reported: ANL-7845, p. 5.26)

Grain-boundary migration rates and other factors relating to fuel restructuring and fission-gas redistribution in the columnar region of a mixed-oxide fuel element have been assessed using optical metallography. The metallographic sections examined were taken from the bottom portion of mixed-oxide fuel element HOV-15 that was irradiated in EBR-II. This element operated for most of its life in a partially molten condition at a peak power rating of 21.4 kW/ft, but was operated at a peak power rating

of only 14.2 kW/ft for 29.75 hr at the end of the irradiation period. During the latter period, the fuel in the central portion of the element partially restructured.

Grain-boundary migration of some of the existing boundaries occurred toward the fuel centerline and also sidewise. The boundaries that migrated toward the fuel centerline moved with velocities of at least 65 \AA/sec (562 \mu/day) to 136 \AA/sec (1175 \mu/day), in spite of the fact that the boundaries were dragging fission-gas bubbles. These rates are five to ten times the migration rates previously measured for gas bubbles (see ANL-7825, p. 5.38). Sidewise migration of radial boundaries also appeared to be quite rapid, but was limited by competition with adjacent migrating boundaries. The rapid migration rates observed here, in addition to evidence for boundary migration found in specimens from other fuel elements (see ANL-7669, p. 112), indicate that boundary migration in the columnar-grain-growth and transition regions of operating fuel elements is a continually recurring phenomenon.

There appear to be two possible mechanisms whereby fission gas is collected on radial boundaries in the columnar-grain-growth region. First, radial columnar boundaries migrating sidewise collect fission-gas bubbles. Second, boundaries migrating toward the fuel centerline collect fission-gas bubbles that are carried along with the boundaries. With continued boundary migration, the bubbles move off to the sides and are left in the radial boundaries. The sweeping and redistribution of fission gas into grain boundaries is consistent with the observation, using replica electron fractography, that most of the fission-gas bubbles present in the columnar-grain-growth region reside on grain boundaries (see ANL-7798, p. 68).

Conclusions related to fuels performance and fuel-element modeling are: (1) Formation of the columnar-grain-growth region during initial fuel restructuring can occur in a short time ($1\frac{1}{2}$ -3 days), assuming a typical maximum boundary migration distance of 0.060 in. (2) When the as-fabricated porosity in an oxide pellet is closed and contains insoluble gas, the kinetics of the formation of the columnar-grain-growth region during initial fuel restructuring are dependent more on boundary-migration processes than on gas-bubble migration. If the porosity is open, the kinetics are dependent on the migration of lenticular-shape voids. (3) Initial fuel restructuring does not move all the as-fabricated porosity in the columnar region to the center of the fuel, but rather redistributes a large fraction of it into the radial boundaries formed during the restructuring. (4) It seems likely that boundary formation and migration, toward the fuel center and also sidewise, in the columnar region of the fuel occur on a continuing basis throughout the lifetime of the fuel element. As a result, almost all the fission gas generated in the columnar region is swept into the radial columnar boundaries, from which it can be released to the central void.

- b. Fuel-element Performance. L. A. Neimark, W. F. Murphy, and E. M. Butler (Last reported: ANL-7833, p. 5.13)

(1) Group O-3, Void Deployment. Microprobe analysis of the matrix reaction layer found in the Type 304H stainless steel cladding of Element SOPC-3 confirmed that this layer was the result of oxidation of the cladding by the fuel (see ANL-7833). The analysis showed that the layer contained oxygen, with the highest content in the cladding adjacent to the fuel and then tapering to a minimum at the inner edge of the layer. The chromium within the layer was partitioned between two phases, with the higher content in the darker phase, which gave the layer its dark appearance. The chromium was depleted immediately adjacent to the fuel. The layer contained less than 1% cesium uniformly distributed.

Microprobe analysis of what appeared to be a vapor-deposited layer of fuel on the inside diameter of the cladding of SOVG-17 (see ANL-7833) indicated that the layer had the same uranium and plutonium content as adjacent fuel spheres. This result precludes the idea of a vapor-deposited uranium-rich layer that may have protected the cladding. The small metallic particles in this layer proved to be iron-nickel.

A fourth element (SOV-15) in this group has been examined. This element contained vibratorily compacted Dynapak powder in 20-mil-thick Type 304H stainless steel cladding (compared with 15-mil cladding in the other Group O-3 elements). The maximum cladding diameter change was $0.2\% \Delta D/D$, but, as in the other Group O-3 elements, there was no distinct region of peak diameter increase. Rather, there was a general increase in diameter over the bottom half of the element. The maximum calculated cladding temperature was 610°C toward the top of the fuel column, which would correlate with the peak cladding-swelling region being below this temperature in the bottom half of the element. Fission-gas release from the element was 75.8% of the total generated, based on a calculated peak burnup of 3.4 at. % and a gas yield of 24.6%. This release is somewhat higher than that from the other elements in Group O-3: SOPC-1, 68.6%; SOPC-3, 62.6%; SOPC-5, 55.5%; and SOVG-17, 59.5%. Also, the xenon/krypton ratio in SOV-15 was 6.99, compared with an average of 6.58 for the pellet elements and 6.61 for the sol-gel element.

The metallographic examination of SOV-15 revealed neither matrix nor intergranular attack of the Type 304H stainless steel cladding. At the midplane of the element, where fuel temperatures were the hottest, what appeared to be a vapor-deposited layer of fuel was adhering tightly to the inside diameter of the cladding. A few small rivulets of metallic particles from the cladding protruded into this fuel layer, as shown in Fig. V.12. Thus, the Dynapak fuel behaved similarly to the sol-gel spherical particles. The metallography also showed that, in at least two locations at the top of the fuel column in what was generally the equiaxed grain-growth

region next to the cladding, extensive localized columnar grain growth occurred, as shown in Fig. V.13. The reason for this is not readily apparent, although its form is similar to that of a healed crack, also shown in Fig. V.13. A porous agglomerate of fuel and metallic fission products was found at the base of the central void, indicating significant inward migration of fission products during this burnup period.

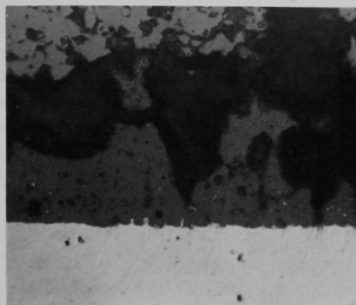


Fig. V.12. Fuel-Cladding Interface at Midplane of SOV-15, Showing Absence of Attack within Cladding. Note minor protrusions of metallic particles into the fuel. Mag. 450X. Neg. No. MSD-161382.

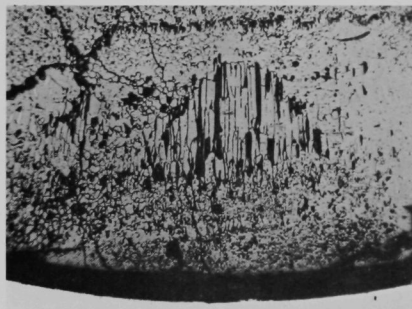


Fig. V.13. Fuel-Cladding Interface in SOV-15, Showing Localized Columnar Grain Growth and at Least One Healed Crack. Mag. 60X. Neg. No. MSD-161386.

The 13 ANL Group O-3 and the five NUMEC Group B mixed-oxide fuel elements being irradiated in EBR-II Subassembly X113 have accumulated an additional 1 at. % burnup. The peak burnup for Group O-3 is now ~4.5 at. %, and for the NUMEC Group B it is ~10.7 at. %.

D. Core Materials Applications

1. Core Design Technology

- a. Empirical Assessment of Swelling and Creep Correlations.
P. R. Huebotter and T. R. Bump, Program Coordination (Last reported: ANL-7833, p. 5.20)

Contemporary LMFBR core design requires reliable expressions for fast-neutron-induced swelling and radiation-enhanced creep of stainless steel, as well as an understanding of integral swelling-creep effects on core structural components. Existing correlations involve considerable uncertainty and are based on controlled experiments to a fluence that is a small fraction of FTR and LMFBR Demonstration Plant targets.

Core components removed from EBR-II, at fluences now approaching these targets, exhibit deformations that are attributable to a

combination of swelling and creep. These deformations are being analyzed to ascertain the reliability of existing swelling and creep correlations and to gain further insight into the response of stainless steel, in typical core structural applications, to the LMFBR environment. The EBR-II Project provides the neutron fluxes, temperatures, and nondestructive measurements employed in the analyses. Destructive measurements are obtained from EBR-II and other projects within ANL and from other participating United States laboratories.

(1) Fuel-element Bow (T. R. Bump). To test the sensitivity of CRASIB* calculations to the creep correlation employed, a calculation was repeated using one-fifth as much creep as before. The calculation considered fuel element ANL-025 in Assembly X040A, with modified temperature distribution (see ANL-7825, p. 5.40). The creep reduction had almost no effect on the calculated transverse displacements. An inspection of the computer output indicated that the maximum cladding strain was almost entirely due to swelling. These findings suggested that the excessive calculated displacements obtained from using the reference temperatures (high gradient across peripheral elements) might be due to excessive calculated creep, rather than to excessive temperature gradient.

Accordingly, displacements were calculated for a number of elements from both Assemblies X040A and X054, using the GROW code that considers swelling** only. Reference temperatures were used throughout. Table V.3 compares measured and calculated bows. As can be seen, the agreement is quite good for Assembly X040A, and fairly good for the X054 elements toward the core vertical centerline. However, the agreement deteriorates for the X054 elements away from the core centerline, particularly in the case of the second-row-in element. (Note that the calculated concave bow of elements away from the core centerline is due to temperatures above the temperature of peak swelling; the hot cladding is swelling less than the cold cladding, according to the calculations.) Actually the results and other fuel-element-bow data suggest that significant creep may have occurred in the X054 elements and not in the X040A elements, a condition that is hard to explain. Little creep in X040A would appear to contradict the evidence that considerable creep occurs in wrapper tubes, both to keep them straight and to cause moat formation near the spacer pads (see below). The disagreement between the behavior of the X040A and X054 elements indicates that more assemblies should be studied, simply to determine typical assembly behavior. Only then should extensive attempts be made to modify temperatures, creep correlations, and swelling correlations (and possibly even fluxes and restraints) so that the best overall correlation between calculated and measured bows can be obtained. For example, the large bows of second-row-in elements away from the core

*W. H. Sutherland and V. B. Watwood, Jr., BNWL-1362 (June 1970).

**H. R. Brager et al., WHAN-FR-16, 11 (Dec 1970).

centerline in X054 (i.e., PNL-5-16) contradict behavior, not only of corresponding X040A elements, but also of X051 and X059 elements.

TABLE V.3. Comparison between Measured^a and Calculated Fuel-element Bows, Assuming No Creep

| Assembly Number | Fuel-element Number | Fuel-element Row | Fuel-element Orientation, deg ^b | Measured Concave ^c Bow, d in. | Calculated Concave ^c Bow, d in. |
|-----------------|---------------------|------------------|--|--|--|
| X040A | ANL-025 | Peripheral | 0 | 0.56 | 0.62 |
| X040A | ANL-024 | Second-row-in | 15 | 0.38 | 0.37 |
| X040A | GE-B-5 | Peripheral | 180 | 0.18 | 0.14 |
| X040A | GE-B-16 | Peripheral | 165 | 0.13 | 0.14 |
| X040A | GE-B-2 | Second-row-in | 180 | Small | Small |
| X054 | PNL-5-28 | Peripheral | 15 | 0.55 | 0.36 |
| X054 | PNL-5-30 | Peripheral | 15 | 0.45 | 0.36 |
| X054 | PNL-5-31 | Second-row-in | 0 | 0.13 | 0.11 |
| X054 | PNL-5-32 | Peripheral | 75 | 0.45 | 0.36 |
| X054 | PNL-5-19 | Peripheral | 165 | 0.47 | 0.14 |
| X054 | PNL-5-17 | Peripheral | 165 | 0.36 | 0.14 |
| X054 | PNL-5-16 | Second-row-in | 180 | 0.39 | -0.04 |

^aR. V. Strain and R. D. Phipps, ANL (EBR-II Project), private communications (Feb and May 1971).

^b0° means on side of assembly toward core vertical centerline; 180° means on side of assembly away from core vertical centerline.

^cWith respect to assembly centerline.

^d"Bow" is maximum transverse displacement between element centerline and a straight line through the centers of the cladding ends.

(2) Moat Formation near Spacer Pads (T. R. Bump). Displacement measurements near the spacer pads of safety-rod thimble 3A1 indicate that once again the distance across the spacer pads remained essentially unchanged, even though nearby the thimble (equivalent of wrapper tube) was dilating dramatically. In this case, relative movement between pad surface and thimble corner, due to creep or some other mechanism, was about 30 mils.* This thimble had a peak exposure of about 1.7×10^{23} nvt (total). Since the nominal clearance between assemblies is 30 mils, the relative movement was approximately sufficient to take the loads off the pads. This value of relative movement is reasonably consistent with the 12-mil relative movement observed in the Assembly XA08 wrapper tube that had a total peak fluence of about 8.5×10^{22} nvt (see ANL-7798, p. 76). The analysis of the XA08 pad deformations indicated that a pad load of ~60 lb would be sufficient to produce the deformations; because the deformations are approximately proportional to both fluence and stress, according to the creep correlation used, a 60-lb load evidently can also be associated with the 3A1 deformations.

*R. D. Phipps, ANL (EBR-II Project), private communication (July 1971).

PUBLICATIONS

Ultrasonic Imaging

H. Berger

Encyclopedic Dictionary of Physics, Vol. 4 (Suppl.), Ed. J. Thewlis.
Pergamon Press, Oxford, 1971, pp. 1-5

Chemical Engineering Division Reactor Safety and Physical Property Studies
Semiannual Report, January-June 1971

M. G. Chasanov, J. Fischer, D. R. Fredrickson, S. D. Gabelnick,
L. Leibowitz, A. D. Tevebaugh, and R. C. Vogel
ANL-7820 (July 1971)

Fission Product Element Distribution in Irradiated Oxide Fuels

I. Johnson, C. E. Johnson, and C. E. Crouthamel
162nd Am. Chem. Soc. Nat. Mtg., Washington, D.C., September 13-
17, 1971. Abstracts of papers, NUCL-45

Temperature Gradient Vacuum Furnace for Diffusion Studies to 2000°C

R. O. Meyer and J. C. Vogelwede
Rev. Sci. Instr. 42, 993-995 (July 1971)

Interaction between Helium Bubbles and Migrating Grain Boundaries in
Copper

S. R. Pati and P. S. Maiya
Acta Met. 19, 807-813 (Aug 1971)

VI. FUEL CYCLE

A. Molten-metal Decladding of LMFBR Fuels

R. D. Pierce (02-173)

A decladding procedure for fast-reactor fuels is being developed in which the stainless steel cladding is dissolved in liquid zinc at 800°C. After removal of the zinc-stainless steel solution from the decladding vessel, the fuel oxide is reduced to metal by contacting it with a Zn-Mg-Ca reduction alloy and a salt containing CaCl_2 . This is followed by distillation, whereby the reduction alloy is removed and the uranium-plutonium metal is concentrated to a form suitable for feeding to an aqueous dissolver.

1. Engineering Development (Last reported: ANL-7845, p. 6.2)

a. Zinc Decladding

An investigation is being made to evaluate the feasibility of using a simplified zinc-decladding process to prepare long-cooled reactor fuel for aqueous processing. The objective would be to replace sodium cleaning, some fuel-disassembly operations, shearing, and voloxidation with zinc dissolution of the stainless steel shroud and cladding. One possible application would be to long-cooled $\text{UO}_2\text{-PuO}_2$ fuel from early breeder operations, and current experiments are being performed to evaluate a procedure for such fuel. The steps in this procedure, which omits the reduction step, are as follows: (1) the cladding is dissolved in zinc, (2) the bulk of the stainless steel-zinc solution is poured off at 800°C, and (3) the residual material and fuel oxide are removed in a second pour to form ingots for charging to an acid dissolver. No overlying salt layer is included in this process because the presence of chloride would necessitate modifications in the subsequent aqueous-processing steps.

Six experiments were performed with no agitation and with mild agitation of the melt at temperatures between 800 and 890°C. Results show that some kind of mechanical agitation will be necessary to obtain a melt sufficiently uniform to pour freely from a crucible in which the stainless steel had been dissolved in zinc.

During these decladding runs under an argon atmosphere at about 15 psig, evaporation of zinc in the absence of a salt cover was not an operating problem.

2. Process Demonstration Experiments (Last reported: ANL-7845, p. 6.4)

a. Irradiated-fuel Experiments

Experimental apparatus has been installed in the Chemical Engineering Division's Senior Cave to investigate the reference liquid-zinc, head-end

process with ~100 g quantities of highly irradiated fuel. Samples from an earlier run with unirradiated UO_2 pellets (see ANL-7845) have been analyzed. Results showed that the decladding step was successful; less than 0.1% of the uranium was lost to the decladding alloy. Reduction of the UO_2 pellets appeared to be complete after 3 hr of agitation (no oxide visible), but the uranium content of the reduction alloy reached a steady value, which was equivalent to only 83% of the uranium charged. The reduction step will be repeated to clarify the reasons for this poor material balance.

In an experiment to determine the behavior of active species formed by irradiation of stainless steel, an irradiated stainless steel rod was dissolved in zinc under a cover of CaCl_2 -10 mol % CaF_2 at 800°C. The activation products detected in significant amounts in the rod and the liquid-metal solution were ^{60}Co and ^{54}Mn . About 30% of the manganese transferred to the salt phase (probably as MnCl_2), and 0.1 to 1% was volatilized from the melt. The oxidation of manganese is thought to have been caused by an oxidizing impurity in the salt used in this experiment. No measurable amounts of cobalt were found in the salt or in the off-gas trap.

B. LMFBR Reprocessing--Plutonium Isolation A. A. Jonke (02-159)

1. Plutonium Valence Adjustment. M. J. Steindler (Last reported: ANL-7833, p. 6.3)

The adjustment of plutonium valence in high-plutonium solutions during the plutonium isolation (and partitioning) steps of the Purex process by an on-stream electrolytic method is being assessed. An electrolytic method for adjusting plutonium valence would be a substitute for chemical methods. Disadvantages of the chemical methods include the need to dispose of large quantities of high-level wastes owing to the large amount of chemical reductant required. Expected advantages of electrolytic reduction are process stability, safety, and economy.

Our current design concept for an electrolytic cell consists of an anode and a cathode in individual compartments, separated by a diaphragm that is permeable to ions but prevents mixing of bulk liquids in the two compartments. The cathode has the configuration of stacks of wire-mesh screen.

The cell design and process parameters that affect the magnitude of the electric current, and thus the reduction rate, in a continuous-electrolysis cell have been identified,* and a mathematical equation for the reduction rate has been developed. Basically, the rate of an electrolytic reduction is limited by the rate at which ions can be transported from the solution to the

*D. S. Webster et al., Chemical Engineering Division Fuel Cycle Technology Quarterly Report: January, February, March 1971, ANL-7799 (July 1971).

electrode surface. For a one-square-centimeter area of the electrode, the rate is equal to the mass-transport coefficient, k . For flowing media,

$$k \equiv \frac{i_L}{NF} = \frac{AcD_{jk}^{(1-n)}V^m}{L^{(1-m)}v^{(m-n)}} \quad (1)$$

where

k = mass-transport coefficient, mol/(sec)(cm²),

i_L = limiting current density, A/cm²,

N = electrical equivalents per mole of ions,

F = Faraday constant, A-sec/equiv,

c = concentration, mol/cm³,

D_{jk} = diffusion coefficient, cm²/sec,

V = linear flow velocity, cm/sec,

L = characteristic electrode dimension, cm,

and

ν = kinematic viscosity of electrolyte, cm²/sec.

The value for the constant n is taken as 0.33, which is the coefficient of the Schmidt number (ν/D_{jk}) derived from mass-transfer results. The constant A depends on the electrode geometry, whereas the constant m is the exponent of the Reynolds number (LV/ν) in mass-transfer correlations; both constants must be determined experimentally for any electrode shape and any given range of flow rates.

Our recent work has been directed toward measuring A and m for the conceptual wire-screen cathodes in the flow range of 1-20 cm/sec. The $\text{Fe}^{3+} + e^- \rightleftharpoons \text{Fe}^{2+}$ reaction has been used as a stand-in for the $\text{Pu}^{4+} + e^- \rightleftharpoons \text{Pu}^{3+}$ reaction. The system chosen was an equimolar solution of potassium ferri-cyanide and potassium ferrocyanide in 0.5M sodium hydroxide, because diffusion coefficients and viscosities for this system had been determined previously by Arvia *et al.**

The apparatus used (see ANL-7776, p. 89) measures the limiting current density of a wire in a stream of electrolyte, over a range of flow velocities. The electrolyte is pumped past a gold-wire cathode, and the potential of the cathode is measured against that of a reference electrode while the current between the cathode and anode is increased. In separate tests with

*A. J. Arvia, J. C. Bazan, and J. S. W. Carrozza, *Electrochim. Acta* **13**, 81 (1968).

three gold-wire cathodes, the limiting currents and limiting current densities were determined with the electrolyte at 25°C, nominal flow velocities of 0.45-28.8 cm/sec, and Reynolds numbers (Re) of 1-100. Values of m (the slopes of log-log plots of limiting current density versus flow velocity) were 0.17, 0.19, and 0.24 for wire cathodes having diameters of 1.2×10^{-2} , 2.4×10^{-2} , and 4.8×10^{-2} cm, respectively. Limiting current densities for a 60-mesh ($d = 1.8 \times 10^{-2}$ cm) gold-plated wire screen were similarly measured, and a value of 0.33 was obtained for m .

The limiting currents were expressed as dimensionless Sherwood numbers (kL/D_{jk}) and the velocities as Reynolds numbers. In accordance with usual practice the Sherwood and Reynolds numbers were combined into the j -factor, which is a simple function of the Reynolds number

$$j = A \text{Re}^{(m-1)} \quad (2)$$

A plot of $\log j$ versus $\log \text{Re}$ has an intercept equal to A ; the value of A found for the wire screen was 0.86, and that for the wires was 1.3.

To compare our results with results in the literature, our mass-transfer data were correlated with heat-transfer data obtained at the same Reynolds numbers. (The j -factors for heat transfer and mass transfer have been found to agree very well at the same Reynolds numbers.) Plots for heat transfer to water for $0.1 < \text{Re} < 10$, obtained by Piret et al.,* correlate excellently with our wire-screen data.

These results show that Eq. 1 accurately describes the mass transport for the particular electrode geometry tentatively designated for reduction cells. Although this work was done with ferricyanide and ferrocyanide solutions rather than plutonium solutions, it was done at the low Reynolds numbers at which the electrolytic cells will be operated, and the results are believed applicable from a process standpoint. The time required to reduce 50% of the plutonium in a cell** with a surface-to-volume ratio of 9 and a linear flow velocity of 2 cm/sec is 5 sec if these values for A and m are used in the mathematical equations describing the reduction process.

C. LMFBR Fuel Refabrication--Analyses and Continuous Processing A. A. Jonke and M. J. Steindler (02-158)

The development of in-line nondestructive methods for analysis of critical fuel properties is necessary to lower the fuel-fabrication costs for the large number of fuel subassemblies expected to be fabricated for the LMFBR program. The specifications of $\text{UO}_2\text{-PuO}_2$ fuel properties

*E. L. Piret, W. James, and M. Stacy, Ind. Eng. Chem. **39**, 1098 (1947).

**D. S. Webster et al., Chemical Engineering Division Fuel Cycle Technology Quarterly Report: January, February, March 1971, ANL-7799 (July 1971)

(and the associated precisions) for the Fast Fuel Test Facility (FFTF) projects have been selected as the starting criteria for evaluating methods of analysis. The originally defined specification for core fuel--a plutonium content that is $20.0 \pm 0.1\%$ of the actinide content--imposes a relative precision of 0.5% on the analysis.

1. Plutonium/Uranium Ratio in Fuel. (Last reported: ANL-7845, p. 6.7)

X-ray fluorescence (XRF) analysis is being developed as an in-line analytical method for determining the Pu/U ratio in $\text{PuO}_2\text{-UO}_2$ fuel materials during fuel fabrication. Experiments are being done to determine whether variations in powder properties prevent attainment of the necessary precision and accuracy. In this work, samples of $\text{UO}_2\text{-ThO}_2$ of selected composition are being used as stand-ins for $\text{UO}_2\text{-PuO}_2$. Earlier, five XRF measurements were made on each of four pellets of each of four compositions ($\text{ThO}_2\text{-10 wt \% UO}_2$, $\text{ThO}_2\text{-20 wt \% UO}_2$, $\text{ThO}_2\text{-30 wt \% UO}_2$, and UO_2) to determine, by an analysis of variance, the functional reproducibility of the XRF measurements (see ANL-7845). Five measurements of each of three samples of $\text{ThO}_2\text{-30 wt \% UO}_2$ powder also were made, and an analysis of variance similar to that for pellets was performed on these results.

It was determined that the variability in the results due to errors attributable to the XRF method was adequately low. It was observed, however, that the variability of results obtained in the analysis of $\text{ThO}_2\text{-30 wt \% UO}_2$ powder samples of the same nominal composition was larger than the variability of results for pellets of the same nominal composition.

Currently, the effects of particle size and bulk density on the XRF signal are being evaluated to determine the precision obtainable for powders under various conditions. The particle-size distribution of a UO_2 powder was determined with an Allen Bradley Sonic Sifter and was found to be within FFTF specifications; therefore, this powder was considered a suitable material for measurement of bulk-density and particle-size effects on XRF signals. In a recently completed series of experiments, samples of this UO_2 of narrow particle-size ranges (-10, 10-20, 20-30, and 37-44 μm) were compacted to densities between 24 and 36% of theoretical, and their fluorescence intensities were measured. Two trends were observed: (1) XRF intensity increased with decreasing particle size, and (2) XRF intensity increased with increasing bulk density. Further evaluation of the effects of particle size and bulk density on the analytical precision is in progress to determine if XRF measurements on powders are applicable for routine, in-line use.

PUBLICATION

Chemical Engineering Division Fuel Cycle Technology Quarterly Report,
January, February, March 1971

D. S. Webster, A. A. Jonke, G. J. Bernstein, N. M. Levitz, R. D. Pierce,
M. J. Steindler, and R. C. Vogel

ANL-7799 (July 1971)

VII. REACTOR PHYSICS

A. ZPR Fast Critical Experiments

1. Fast Critical Facilities; Experiments and Evaluation--Illinois. C. E. Till (02-179)

a. Clean Critical Experiments. R. A. Lewis (Last reported: ANL-7845, p. 7.1)

(1) Control-rod Experiments in Assembly 7: Control-rod Reactivity Worths and Reaction-rate Distributions in the Vicinity of the Control Rod (J. F. Meyer, E. M. Bohn, and W. R. Robinson). A series of control-rod experiments has begun in ZPR-6 Assembly 7.* The measurements have been planned to completely characterize the effect of a single, simulated-LMFBR-type, B_4C control-rod assembly on the important physics parameters of the core. The initial set of experiments, control-rod reactivity worths, and reaction-rate distributions in the vicinity of the control rod has been completed. Four configurations of the control-rod assembly were loaded at the center of Assembly 7 with the High-240 plutonium zone (see ANL-7833, p. 7.1). They were:

1. A simulated control rod consisting of a single ZPR-6 drawer containing 63 wt % sodium canned in stainless steel and 37 wt % B_4C (natural boron); the control rod extends completely through the core axially.
2. The control rod described in configuration 1 surrounded by BeO .
3. A sodium channel of the same dimensions as the control rod in configuration 1.
4. The sodium channel described in configuration 3 surrounded by BeO .

Configurations 1 and 2 represent "control in" geometry, and configurations 3 and 4 represent "control out" geometry.

Figures VII.1 and VII.2 show the B_4C control-rod and the B_4C - BeO control-rod configurations, respectively, as they were loaded at the center of the core. The sodium channel would appear the same as the B_4C control rod in Fig. VII.1 with the B_4C replaced with sodium. Similarly, the sodium- BeO configuration is the same as the B_4C - BeO control rod in Fig. VII.2 with the B_4C replaced with sodium. Table VII.1 lists the homogeneous compositions of the various configurations.

*E. M. Bohn, L. G. LeSage, R. A. Lewis, and C. E. Till, ANL internal memorandum (July 1970).

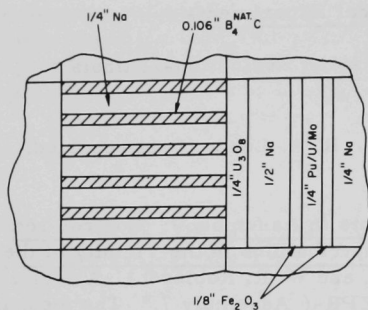


Fig. VII.1

B₄C Control Rod at Center of HPu Zone in ZPR-6 Assembly 7. (Axially the rod extends 220.68 cm through the entire core--152.4 cm through the Pu/U/Mo core and 68.28 cm through two depleted-uranium axial reflectors.)

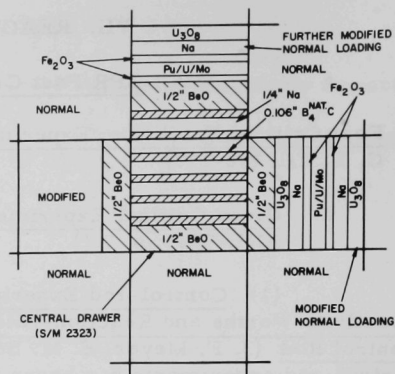


Fig. VII.2

B₄C Control Rod Surrounded by BeO Loaded at Center of HPu Zone in ZPR-6 Assembly 7. (Axially the rod and the BeO annulus extend 220.68 cm through the entire core.)

TABLE VII.1. Homogeneous Compositions in Simulated Control-rod-configuration Regions^a

| Isotope | Atoms/cc $\times 10^{-24}$ ^b | | |
|-----------------|---|-----------------------------|-----------------------|
| | Na Channel | B ₄ C-Na Channel | BeO Ring |
| Na | 1.797×10^{-2} | 1.015×10^{-2} | - |
| ¹⁰ B | - | 3.800×10^{-3} | - |
| ¹¹ B | - | 1.42×10^{-2} | - |
| C | - | 4.76×10^{-3} | - |
| Be | - | - | 5.32×10^{-2} |
| ¹⁶ O | - | - | 5.32×10^{-2} |
| Fe | 9.54×10^{-3} | 1.03×10^{-2} | 6.67×10^{-3} |
| Ni | 1.46×10^{-3} | 1.34×10^{-3} | 8.04×10^{-4} |
| Cr | 3.19×10^{-3} | 2.90×10^{-3} | 1.86×10^{-3} |
| Mn | 1.90×10^{-4} | 2.10×10^{-4} | 1.35×10^{-4} |

^aThe Na channel and B₄C-Na channel occupy one drawer in the matrix (i.e., one unit-cell in volume). See Figs. VII.1 and VII.2. The area of one drawer (including matrix) is 30.5201 cm². Thus, when the control-rod channel is loaded at the center of the core, its effective circular radius is 3.117 cm. The BeO loaded in the drawers around the control-rod channel (see Fig. VII.2) occupies an annular volume around the control-rod channel with inner radius 3.117 cm and outer radius 4.448 cm. The concentrations for each configuration include the SS 304 contributions from the drawer and matrix.

^bThe atom densities are precise (2σ confidence) to the number of digits indicated.

The worth of each configuration was determined by measuring the change in excess reactivity of the core or the subcriticality of the core as each configuration was loaded in the core. Subcriticality was measured using four methods: inverse kinetics,* multiplication, noise cross-correlation,** and rod-drop flux profile analysis.† The control-rod worths are summarized in Table VII.2. The BeO annulus enhances the worth of the B₄C control rod. This result is due primarily to the softening of the spectrum by the BeO in the vicinity of the control rod.

TABLE VII.2. Measured Reactivity Worths of the Simulated B₄C Control Configurations in ZPR-6 Assembly 7

| Configuration | Experimental Method ^a | Worth Versus Void Channel, ^b 1h | Worth Versus Na Channel, ^b 1h | Worth Versus Fuel Drawer, ^b 1h |
|----------------------|----------------------------------|--|--|---|
| B ₄ C | Rod Drop: Inverse Kinetics | -440.1 ± 13.5 | -444.4 ± 11.9 | -577.9 ± 12.7 |
| | Rod Drop: Flux Profile Analysis | | -441.5 ± 3.5 | |
| | Multiplication | | -435.7 ± 7.3 | -577.7 ± 8.6 |
| | Noise | | -468.2 ± 12.8 | -610.5 ± 13.7 |
| B ₄ C-BeO | Rod Drop: Inverse Kinetics | -569.0 ± 17.3 | -573.3 ± 16.1 | -706.8 ± 16.7 |
| | Rod Drop: Flux Profile Analysis | | -577.7 ± 16.0 | |
| | Multiplication | | -566.7 ± 7.4 | -708.7 ± 8.7 |
| | Noise | | -627.4 ± 11.5 | -769.7 ± 12.5 |
| Na | Rod Drop: Inverse Kinetics | +4.3 ± 6.3 | | -133.5 ± 4.5 |
| | Multiplication | | | -142.0 ± 4.6 |
| | Noise | | | -142.3 ± 4.9 |
| Na-BeO | Rod Drop: Inverse Kinetics | 23.2 ± 7.4 | | -114.6 ± 5.9 |
| | Multiplication | | | -123.1 ± 6.0 |
| | Noise | | | -123.4 ± 6.2 |
| | Excess | | 18.9 ± 3.8 | |

^aThe worth values reported in this table were determined by comparing subcriticality measurements with other subcriticality measurements or excess measurements. The experimental method refers to the method of subcriticality measurement.

^bThere are 1022 1h per % Δk/k.

*C. E. Cohn, ANL internal memorandum (Dec 1970).

**C. E. Cohn, Experience with Subcriticality Determination by Noise Techniques in the FTR Engineering-Mockup Critical Experiment Program, submitted for presentation at the Winter ANS Meeting, Miami Beach, Florida (Oct 1971).

†E. F. Bennett, ANL internal memorandum (May 1971).

Radial reaction-rate mappings in the vicinity of each control-rod configuration were obtained by foil irradiations at the reactor midplane. ^{238}U , ^{235}U , and ^{239}Pu foils were placed between the Fe_2O_3 plate and the fuel plate in the drawers along column 23 from the edge of the control rod at the core center to the outer boundary of the core. Fission rates in ^{239}Pu , ^{238}U , and ^{235}U as well as the capture rate of ^{238}U were measured and are reported here in Figs. VII.3-VII.6 for each of the four configurations. The effect on the reaction-rate distributions of the presence of B_4C and BeO is clearly indicated in these figures.

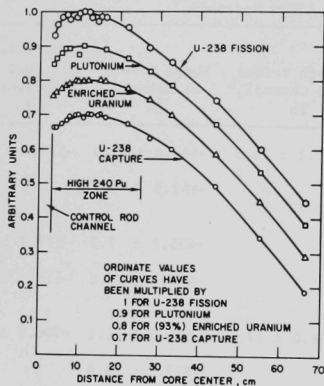


Fig. VII.3. Radial Reaction-rate Mappings in the Vicinity of the B_4C Control Rod

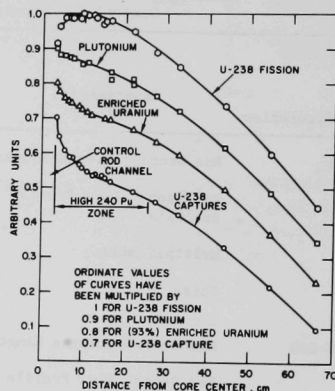


Fig. VII.4. Radial Reaction-rate Mappings in the Vicinity of the B_4C - BeO Control Rod

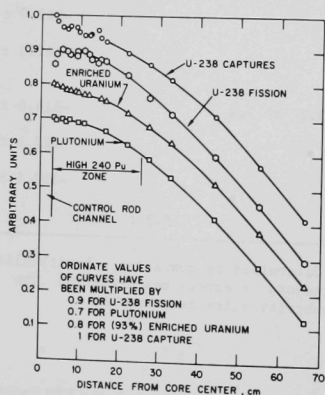


Fig. VII.5. Radial Reaction-rate Mappings in the Vicinity of the Sodium Channel

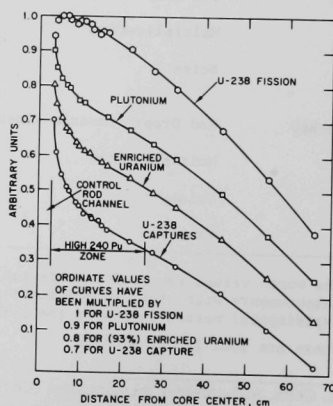


Fig. VII.6. Radial Reaction-rate Mappings in the Vicinity of the Sodium- BeO Channel

- b. Mockup Critical Experiments. J. W. Daughtry (Last reported: ANL-7845, p. 7.4)

(1) Radial Reaction-rate Distributions in the FTR Engineering Mockup Critical (EMC) (A. B. Long). The objective of this experiment was to measure radial reaction-rate distributions of special interest for the FTR design. Of primary interest was the power distribution in the reactor. The measurements were made in a configuration of the Engineering Mockup Critical (EMC) that simulated approximately the Beginning-of-Life (BOL) conditions in the FTR.

Radial reaction-rate distributions of $^{239}\text{Pu}(n,f)$, $^{238}\text{U}(n,f)$, and $^{10}\text{B}(n,\alpha)$ were measured along a traverse hole located approximately 1.75 in. back from the interface of the two reactor halves and extending from matrix position S23-21 to S23-39 (see Fig. VII.7). The traverses hole had a 1.125-in. diameter.

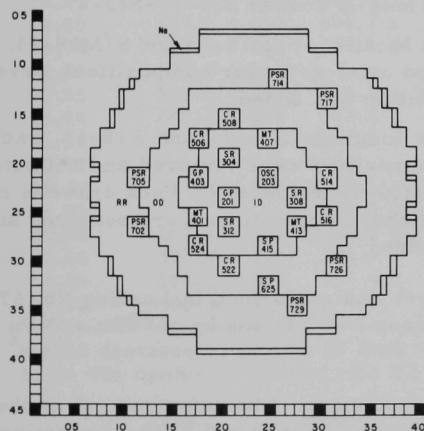


Fig. VII.7

FTR-EMC Core Map for Stationary Half of ZPR-9. ANL Neg. No. 116-744.

(a) Core Configuration. Figure VII.7 shows the core map of the front face of ZPR-9 Assembly 27 which is the FTR-EMC. The identification letters in the figure are defined as follows:

| | |
|--------------------------|-------------------------------|
| ID--Inner driver | SP--Special purpose loop |
| OD--Outer driver | MT--Material test subassembly |
| RR--Radial reflector | SR--Safety rod |
| OSC--Oscillator | CR--Control rod |
| GP--General purpose loop | PSR--Peripheral shim rod |

The numbers within the squares identify corresponding subassemblies in the FTR.

The configuration of the core for the reaction-rate experiment is described below:

- a. OSC 203, withdrawn position.
- b. GP 201, 403 inserted.
- c. SP 415, 625 inserted.
- d. MT 401, 507, 413 inserted.
- e. SR 304, 308, 312 withdrawn position.
- f. CR 506, 514, 522 fully withdrawn.
- g. CR 508, 516, 524 fully inserted.
- h. PSR 702, 714, 726 inserted.
- i. Autorod mounted in matrix position 23-14.
- j. Traverse hole in drawer S23-21-S23-29.
- k. At matrix locations S/M16-15 and S/M18-13, front drawers containing outer-driver and axial-reflector compositions were removed and radial-reflector composition was added.

1. At matrix locations S16-15 and S18-13, back drawers containing axial-shield composition were removed and reflector-shield composition was added. At M16-15 and M18-13, back drawers containing core plenum and handling socket compositions were removed and reflector-shield composition was added.

This experiment was performed in Loading No. 67 of ZPR-9 Assembly 27. The fissile mass was 531.486 kg of ^{239}Pu + ^{241}Pu and 5.057 kg of ^{235}U .

(b) Experimental Technique. The experimental method used to record and correct the $^{239}\text{Pu}(n,f)$, $^{238}\text{U}(n,f)$ and $^{10}\text{B}(n,\alpha)$ reaction-rate data was described for a previous experiment (see ANL-7737, pp. 18-19). The traverse detectors were the same as those used previously. They were placed at the end of the radial sample-changer tube without any stainless steel plugs and traversed through the void hole. A reduction in the background of the ^{10}B spectrum was realized in these measurements by using an argon- CO_2 gas in the counter and thus reducing proton recoils.

The data were recorded in these measurements "on-line" using the SEL-840 computer and immediately corrected for dead-time and background. New Ortec Model 486 Amplifier Pulse Height Analyzers were used giving a more reliable constant dead-time of 1.8 μsec per pulse.

(c) Results. The results of the $^{239}\text{Pu}(n,f)$, $^{238}\text{U}(n,f)$, and $^{10}\text{B}(n,\alpha)$ reaction-rate distributions are given in Table VII.3 and plotted in Figs. VII.8-VII.10. The results are only relative, not having been corrected for foil mass or reactor power.

TABLE VII.3. Radial Reaction-rate Distributions Measured near the Core Midplane in the BOL Configuration of the FTR-EMC

| Relative Reaction Rates | | | | |
|-------------------------------|------------------------|-------------------------------|-------------------------------|-----------------------|
| Relative Reaction Rates | | | Relative Reaction Rates | |
| Position, ^a in. | ²³⁹ Pu(n,f) | ¹⁰ B(n, α) | Position, ^a in. | ²³⁸ U(n,f) |
| 0.00 | 910.2 \pm 4.7 | 854.1 \pm 4.6 | 0.00 | 103.76 \pm 1.15 |
| 2.18 | | 867.6 \pm 13.1 | 2.18 | 98.27 \pm 1.33 |
| 2.22 | 912.5 \pm 6.8 | | 2.54 | 97.17 \pm 0.96 |
| 4.36 | 902.0 \pm 5.1 | 846.8 \pm 14.7 | 4.72 | 94.33 \pm 1.40 |
| 6.53 | 872.6 \pm 4.6 | 833.7 \pm 8.3 | 6.89 | 89.09 \pm 1.06 |
| 8.71 | 830.8 \pm 5.1 | 799.2 \pm 7.5 | 9.07 | 84.00 \pm 1.11 |
| 10.89 | 791.2 \pm 4.4 | 747.9 \pm 8.3 | 11.25 | 80.66 \pm 1.29 |
| 13.07 | 718.6 \pm 4.0 | 669.9 \pm 4.0 | 13.43 | 77.34 \pm 1.42 |
| 15.24 | 652.1 \pm 3.2 | 605.1 \pm 7.3 | 14.52 | 73.85 \pm 1.36 |
| 17.42 | 594.2 \pm 3.6 | 558.5 \pm 3.4 | 16.69 | 68.98 \pm 1.51 |
| 19.60 | 547.9 \pm 4.0 | 523.7 \pm 1.5 | 17.79 | 66.75 \pm 1.32 |
| 21.78 | 513.8 \pm 2.6 | 537.9 \pm 7.8 | 19.96 | 61.95 \pm 1.50 |
| 22.86 | 517.2 \pm 3.8 | | 22.14 | 53.50 \pm 1.27 |
| 23.95 | 541.6 \pm 3.3 | 680.3 \pm 35.7 | 24.32 | 37.86 \pm 1.16 |
| 25.04 | 602.8 \pm 4.1 | 823.8 \pm 2.9 | 26.49 | 18.69 \pm 0.62 |
| 26.13 | 708.9 \pm 4.1 | 1037.5 \pm 3.5 | 30.85 | 4.33 \pm 0.25 |
| 27.21 | 755.7 \pm 5.1 | | 33.03 | 2.15 \pm 0.13 |
| 28.30 | 753.4 \pm 4.0 | 1237.5 \pm 44.2 | 35.20 | 1.06 \pm 0.07 |
| 29.40 | | 1136.0 \pm 2.3 | 37.38 | 0.56 \pm 0.03 |
| 30.48 | 601.1 \pm 4.1 | 1001.9 \pm 1.8 | 39.56 | 0.48 \pm 0.08 |
| 32.66 | 397.7 \pm 2.9 | 675.9 \pm 2.6 | | |
| 34.84 | 224.1 \pm 2.0 | 366.4 \pm 2.8 | | |
| 37.02 | 136.8 \pm 1.4 | | | |

^aRadial distance along Row 23 from the axis of the assembly, which is at the center of matrix tube 23-23.

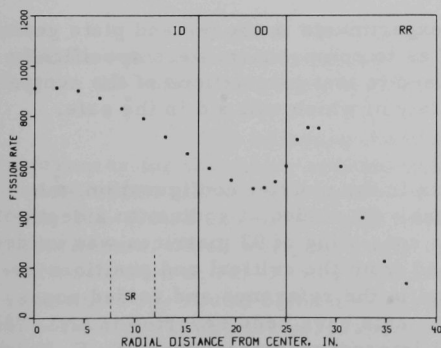


Fig. VII.8. ²³⁹Pu Fission-rate Radial Traverse

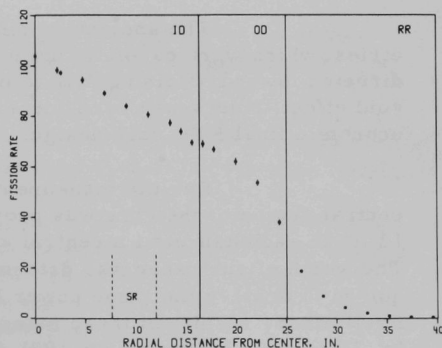


Fig. VII.9. ²³⁸U Fission-rate Radial Traverse

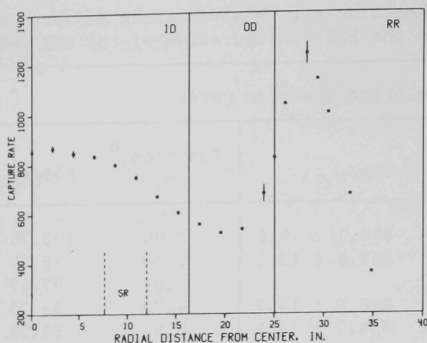


Fig. VII.10
 $^{10}\text{B}(n,\alpha)$ Reaction-rate
 Radial Traverse

2. Fast Critical Facilities; Experiments and Evaluation--Idaho. W. G. Davey (02-181)

a. Coolant-reactivity Experiments. P. I. Amundson (Not previously reported)

(1) FTR-requested Sodium Worth Measurements in ZPPR-2 (J. C. Young and A. L. Hess). The sodium-voiding experiments in support of Phase C of the FTR program have been completed in both the pin and plate central inner-core environment.*

The purpose of these experiments is to provide information to enable the designer to make corrections (if necessary) to the basic data obtained in the plate-type critical to make it correspond to the particular pin geometry of the FTR. In the absence of pins of composition and geometry identical to that of the FTR, the approach adopted was a program of measurements to isolate the effects of the two local geometries (pin and plate) with as few complicating differences as possible.

The sodium-voiding experiments in the pin and plate geometries, which were carefully matched as to composition, were specifically directed toward obtaining data to be used to test calculations of the central void effect, a decrease in the uncertainty of which will aid in the safe, economic final FTR core design.

For the measurements in the platelet configuration, the central region of the core was progressively voided of sodium to a depth of 12 in. in each half until a central zone consisting of 93 matrices was voided. The worth of each zone was determined from the critical rod positions required to achieve the same power level in the reference and voided zones. Preliminary results of these measurements have been reported in ANL-7825 (p. 7.13) and in a January 20, 1971 ANL internal memorandum by R. E. Kaiser (p. 27). These results have been refined and are given in Table VII.4.

*W. G. Davey and C. E. Till, ANL internal memorandum (Feb 10, 1970).

TABLE VII.4. FTR Sodium-void Measurements in ZPPR Assembly 2

| Zone | Void Length (in.) | Sodium Removed (kg) | | Total Worth (Ih) | | Specific Worth (Ih/kg) | |
|-----------------------|-------------------|---------------------|-------------|-------------------|-------------------|------------------------|-----------------|
| | | Platelet Config. | Pin Config. | Platelet Config. | Pin Config. | Platelet Config. | Pin Config. |
| Central Matrix | - 6 to 0 | 0.165 | 0.165 | 0.840 \pm 0.090 | 0.815 \pm 0.054 | 5.11 \pm 0.54 | 4.94 \pm 0.33 |
| | -12 to 0 | -- | 0.330 | -- | 1.066 \pm 0.050 | -- | 3.23 \pm 0.15 |
| | -18 to 0 | -- | 0.495 | -- | 0.668 \pm 0.059 | -- | 1.35 \pm 0.12 |
| | -12 to +12 | 0.660 | -- | 2.5 \pm 0.8 | -- | 3.8 \pm 1.2 | -- |
| 9 Matrices (3x3) | - 6 to + 6 | 2.971 | -- | 14.6 \pm 0.8 | -- | 4.9 \pm 0.3 | -- |
| | -12 to +12 | 5.942 | 5.943 | 17.0 \pm 0.8 | 19.4 \pm 0.8 | 2.9 \pm 0.1 | 3.3 \pm 0.1 |
| | -18 to +18 | -- | 8.911 | -- | 14.0 \pm 0.8 | -- | 1.6 \pm 0.1 |
| | -12 to +12 | 13.866 | 13.876 | 45.4 \pm 0.8 | 46.3 \pm 0.8 | 3.27 \pm 0.06 | 3.33 \pm 0.06 |
| 45 Matrices (7x7 wcm) | -12 to +12 | 29.714 | 29.710 | 95.2 \pm 0.8 | 98.4 \pm 0.8 | 3.20 \pm 0.03 | 3.31 \pm 0.03 |
| 61 Matrices (9x9 wcm) | -12 to +12 | -- | 40.280 | -- | 137.1 \pm 0.8 | -- | 3.4 \pm 0.02 |
| 69 Matrices (9x9 wcm) | -12 to +12 | 45.562 | 45.560 | 147.0 \pm 0.8 | 154.1 \pm 0.8 | 3.23 \pm 0.02 | 3.38 \pm 0.02 |
| 93 Matrices | -12 to +12 | 61.410 | -- | 198.1 \pm 0.8 | -- | 3.23 \pm 0.01 | -- |

^awcm = with corners missing.

Following the substitution of pin calandria for plate drawers in the central 69-matrix zone, corresponding sodium-void measurements were made in the pin configuration. Again the voiding proceeded in steps until a 69-matrix zone was voided to a depth of 12 in. in each reactor half. The construction of a 93-matrix pin zone was not possible, due to the limited amount of calandria available at the time of the pin experiments. For the single-matrix and nine-matrix zones, additional measurements were made for voids axially extending 6 and 18 in. into each half. With the exception of the single-matrix zone, the worths of the voided zones were determined from comparison of critical rod positions, as was done for the measurements in the platelet configuration. For the worth measurements in the single-matrix zone, an experimental drive was employed to oscillate the calandria in matrix position 237-37, and the worths were obtained by inverse-kinetics methods. The worths of the voided zones in the pin configuration are also given in Table VII.4.

Figures VII.11 and VII.12 show the 69- and 93-matrix-position void zones superimposed on the Half 1 loading diagram of Loading 90, the reference core for ZPPR Assembly 2.

The following modifications to Loading 90 were made for the references for the major sodium-voiding experiments: In the plate configuration, radial blanket was substituted for core material in matrix positions 126-49 and 226-49 for both zone sizes. For the pin sodium-voiding experiments, which were done only in the 69-matrix-position case, the control rod shown at 141-39 was relocated to 144-43 and core material was substituted for radial blanket material in matrix positions 123-29, 123-45, 151-45, 148-49, and the corresponding positions in Half 2.

A possible alternative to zone-voiding measurements that has been considered involves integration of perturbation-sample traverse

measurements. To compare the two methods, a correlation was made of sodium worths in the FTR voiding configurations in the plate core with zone sodium worths derived by integration of worth profiles previously obtained by traversing a small sodium sample. Four radial traverses were run through penetrations at the axial locations of 3, 11, 14, and 22 in. from the midplane. The centerline worths from these measurements gave a four-point axial traverse. An overall axial-worth profile was adapted to the four axial points based on the shape of the axial-worth distribution given by a perturbation-theory calculation (using 2-D diffusion theory in R-Z geometry). The radial profiles in the region of interest (to 11-in. radius) were much less critical, decreasing at most by about 10% from the centerline values.

Using the assumed experimental axial-worth profile and smoothed curves from the radial-worth traverses, a sodium-worth mapping was established. This map was then used to calculate worths of sodium in 6-in. axial lengths in each of the matrix positions involved in the FTR

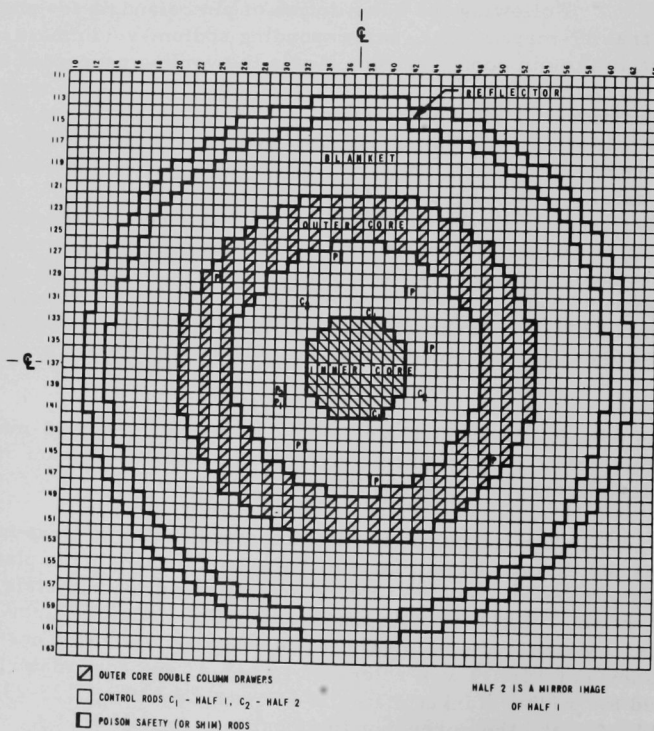


Fig. VII.11. ZPPR Assembly 2, 69-matrix Void Zone

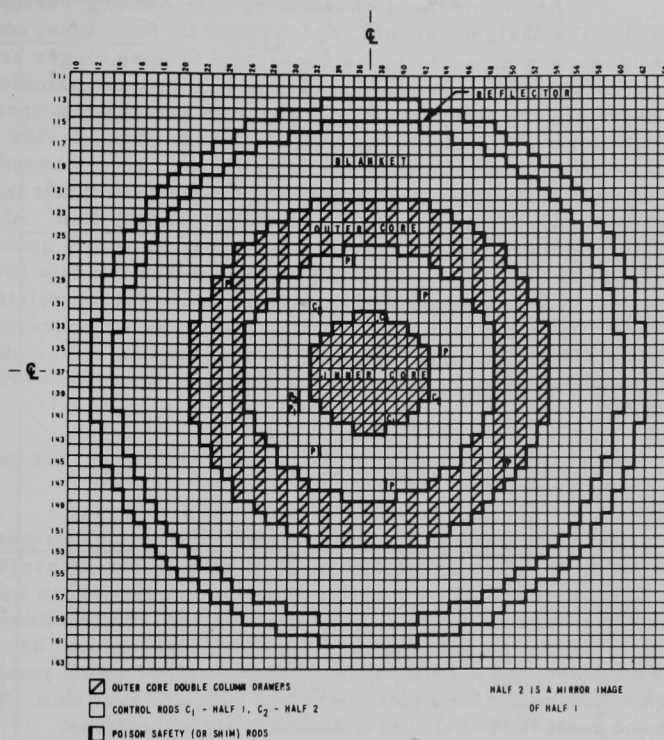


Fig. VII.12. ZPPR Assembly 2, 93-matrix Void Zone

voiding experiments. Table VII.5 compares the results of the worth integrations for the various zone sizes with corresponding results of the direct voiding experiments.

TABLE VII.5. Comparison of FTR Voiding Experiments in Plate Core with Voiding Worths Derived from Small-sample Traverses

| Voided Zone Size | Void Length (in.) | Plate Sodium Removed, kg | Measured Zone Voiding Worth, Ih | Zone Voiding Worth by Integration of Traverse Worths, Ih | Specific Worth, Ih/kg for Na replaced by Void | |
|------------------------------------|-------------------|--------------------------|---------------------------------|--|---|------------------------|
| | | | | | Zone Voiding | Average From Traverses |
| Central Matrix | - 6 to 0 | 0.165 | 0.84 ± 0.09 | 0.74 ± 0.03 | 5.11 ± 0.54 | 4.48 ± 0.20 |
| | -12 to +12 | 0.660 | 2.5 ± 0.8 | 2.09 ± 0.13 | 3.8 ± 1.2 | 3.17 ± 0.20 |
| 9 Matrices (3x3) | - 6 to + 6 | 2.971 | 14.6 ± 0.8 | 13.25 ± 0.59 | 4.9 ± 0.3 | 4.46 ± 0.20 |
| | -12 to +12 | 5.942 | 17.0 ± 0.8 | 18.8 ± 1.2 | 2.9 ± 0.1 | 3.16 ± 0.20 |
| 21 Matrices (5x5 wcm) ^a | -12 to +12 | 13.866 | 45.4 ± 0.8 | 43.6 ± 2.8 | 3.27 ± 0.06 | 3.14 ± 0.20 |
| 45 Matrices (7x7 wcm) | -12 to +12 | 29.714 | 95.2 ± 0.8 | 92.3 ± 5.8 | 3.20 ± 0.03 | 3.11 ± 0.20 |
| 69 Matrices (9x9 wcm) | -12 to +12 | 45.562 | 147.0 ± 0.8 | 139.5 ± 8.8 | 3.22 ± 0.02 | 3.06 ± 0.20 |
| 93 Matrices | -12 to +12 | 61.410 | 198.1 ± 0.8 | 185. ± 12 | 3.23 ± 0.01 | 3.01 ± 0.20 |

The two methods of obtaining zone-voiding worths are seen to agree within the assigned errors, which might be fortuitous, considering the change in spectra incurred in the successive voiding stages as compared to the constant spectra that would exist in the small-sample perturbation experiments. The comparison thus suggests that the traverse data can be integrated to provide zone-voiding worths (for restricted-size zones), provided that the accuracy (a relatively constant percentage based on the precision of central perturbation worths) is acceptable and that the second-order effects (spectrum changes) are considered unimportant. Although the zone and integrated perturbation measurements agree within quoted errors, a definite shape is observed in the integrated perturbation data (within the absolute errors of the measurement). This implies that the relative shapes are better than the error limits would imply, and that the zone-voiding measurements showing a constant worth with increasing radius should be used with caution relative to generation of radial differential-worth distributions.

b. Heterogeneity Measurements. P. I. Amundson (Not previously reported)

(1) Central-zone Plate/Pin Heterogeneity Measurements in ZPPR Assembly 2 (W. K. Lehto and W. P. Keeney). The measured central-zone heterogeneity effects of a pin- for plate-zone substitution was previously reported (see ANL-7845, p. 7.9) to be -76.1 lh. Corrections for the compositional mismatch, inherent in the matching procedure, have been made. As reported, the substitution was done in steps which resulted in four intermediate zones for which corrected data are available. These zones are the central 21-, 41-, 61-, and 69-matrix locations.

Corrections were made for the compositional mismatch in the stainless steel constituents, ^{238}U , and in the fissile plutonium content due to ^{241}Pu decay. Since the ^{239}Pu content was essentially exactly matched, the corrections reported for fissile plutonium are those due to ^{241}Pu mismatch. Furthermore, no mismatch in sodium or oxygen was recognized, because of the exacting matching procedure. A small imbalance between the plate and pin drawers exists in the oxygen content in the first 6 in. of the axial blanket and has been ignored because of its negligible reactivity effect. The full-zone average number densities are listed in Table VII.6.

The matching was done on a three-subzone-per-drawer basis for each half of the core. These zones were the first 12 in. of inner core, the next 6 in. of inner core, and the first 6 in. of axial blanket. This resulted in 126, 246, 366, and 414 matching subzones for the 21-, 41-, 61-, and 69-matrix-size zones, respectively. Average material worths were calculated for each subzone using measured small-sample reactivity traverses. An exception to this was the manganese worth, which was calculated. The correction term is dominated by the inherent mismatch in stainless steel and by the fissile material differences due to ^{241}Pu decay.

TABLE VII.6. Average Compositions of 69-drawer Calandria Regions and Matching Plate Region

| Material | Region Compositions, 10^{22} atoms/cm ³ | | | |
|-------------------|--|------------------------|---|------------------------|
| | Inner Core (0 to 18 in. Axially in Both Halves) | | Axial Blanket (18 to 24-in. Axial Section in Both Halves) | |
| | PuO ₂ -UO ₂ Pins in Calandria | Matching Plate Loading | UO ₂ Pins in Calandria | Matching Plate Loading |
| ²³⁸ Pu | 0.00007 | 0.00006 | - | - |
| ²³⁹ Pu | 0.08438 | 0.08439 | - | - |
| ²⁴⁰ Pu | 0.01126 | 0.01118 | - | - |
| ²⁴¹ Pu | 0.00168 ^a | 0.00148 ^b | - | - |
| ²⁴² Pu | 0.00016 | 0.00018 | - | - |
| ²⁴¹ Am | 0.00020 ^a | 0.00035 ^b | - | - |
| ²³⁵ U | 0.00126 | 0.00123 | 0.00135 | 0.00153 |
| ²³⁸ U | 0.55636 | 0.55530 | 0.65630 | 0.69326 |
| O | 1.30821 | 1.31287 | 1.31650 | 1.26518 |
| Na | 0.88779 | 0.89116 | 0.88779 | 0.88486 |
| Fe | 1.16899 ^c | 1.22672 ^c | 1.16601 ^c | 1.11237 ^c |
| Cr | 0.33592 | 0.25996 | 0.33542 | 0.31088 |
| Ni | 0.15300 | 0.11847 | 0.15277 | 0.13968 |
| Mn | 0.02510 | 0.02186 | 0.02507 | 0.02569 |
| Si | 0.01604 | 0.01301 | 0.01604 | 0.01532 |
| Mo | 0.02312 | 0.02356 | 0.00150 | 0.00240 |
| Cu | 0.00245 | 0.00287 | 0.00245 | 0.00362 |
| Co | 0.00078 | 0.00036 | 0.00078 | 0.00069 |
| Al | 0.00029 | 0.00034 | 0.00029 | 0.00024 |
| Ta | 0.00002 | - | 0.00002 | - |
| Ti | 0.00017 | - | 0.00012 | - |
| Nb | 0.00053 | - | 0.00053 | - |
| C | 0.00297 | 0.00292 | 0.00297 | 0.00405 |
| P | 0.00061 | 0.00045 | 0.00061 | 0.00064 |
| S | 0.00030 | 0.00016 | 0.00030 | 0.00027 |

^aNot corrected for ²⁴¹Pu decay, analysis date presently unknown.^bCorrected for ²⁴¹Pu decay to date of July 1, 1971.^cIncludes minor impurities in claddings, pins, and sodium and unaccountables in steel analyses.

The uncertainty in the correction term was also calculated. This uncertainty is due to (1) errors in the measured reactivities, (2) the error in material matching due to imprecise knowledge of the actual mass of each material involved, and (3) half-closure errors.

Tables VII.7-VII.10 present the results for the four zones: ΔM is the material mismatch; σ_1 is the error due to imprecise knowledge of the mass of each material; σ_2 is the error due to uncertainties in the material-worth measurements; σ is the overall error on the correction term and is equal to $(\sigma_1^2 + \sigma_2^2)^{1/2}$. Table VII.11 summarizes the experimental results, the corrections, and the errors, and lists the reactivities with the uncertainty for each of the four pin- for plate-zone substitutions.

TABLE VII.7. Compositional Correction Terms and Associated Imprecisions for Central 21 Matrix Locations

| Material | ΔM (Plate-Pin), kg | ρ , Ih | σ_1 , Ih | σ_2 , Ih | σ , Ih |
|-------------------------------------|----------------------------------|----------------|--------------------|--------------------|------------------|
| $^{239}\text{Pu} + ^{241}\text{Pu}$ | -0.029 | -2.58 | 1.09 | 0.007 | 1.09 |
| ^{235}U | 0.011 | -0.32 | 0.0 | 0.01 | 0.01 |
| ^{238}U | 0.55 | 0.74 | 1.0 | 0.22 | 1.02 |
| Mo | -0.01 | 0.03 | 0.005 | 0.003 | 0.006 |
| Fe, Ni, Cr, Mn and Impurities | -5.49 | <u>4.81</u> | <u>0.12</u> | <u>1.25</u> | <u>1.26</u> |
| | | 2.68 | 1.48 | 1.28 | 1.95 |

TABLE VII.8. Compositional Correction Terms and Associated Imprecisions for Central 41 Matrix Locations

| Material | ΔM (Plate-Pin), kg | ρ , Ih | σ_1 , Ih | σ_2 , Ih | σ , Ih |
|-------------------------------------|----------------------------------|----------------|--------------------|--------------------|------------------|
| $^{239}\text{Pu} + ^{241}\text{Pu}$ | -0.058 | -4.99 | 2.14 | 0.014 | 2.14 |
| ^{235}U | 0.022 | -0.62 | 0.0 | 0.019 | 0.019 |
| ^{238}U | 1.07 | 1.42 | 1.96 | 0.43 | 2.0 |
| Mo | -0.022 | 0.067 | 0.011 | 0.006 | 0.012 |
| Fe, Ni, Cr, Mn and Impurities | -10.74 | <u>9.29</u> | <u>0.27</u> | <u>2.84</u> | <u>2.85</u> |
| | | 5.16 | 2.91 | 2.87 | 4.08 |

TABLE VII.9. Compositional Correction Terms and Associated Imprecisions for Central 61 Matrix Locations

| Material | ΔM (Plate-Pin), kg | ρ , Ih | σ_1 , Ih | σ_2 , Ih | σ , Ih |
|-------------------------------------|----------------------------------|----------------|--------------------|--------------------|------------------|
| $^{239}\text{Pu} + ^{241}\text{Pu}$ | -0.087 | -7.36 | 3.59 | 0.021 | 3.19 |
| ^{235}U | 0.032 | -0.91 | 0.0 | 0.029 | 0.029 |
| ^{238}U | 1.57 | 2.1 | 3.27 | 0.63 | 2.99 |
| Mo | -0.033 | 0.1 | 0.019 | 0.009 | 0.018 |
| Fe, Ni, Cr, Mn and Impurities | -15.99 | <u>13.66</u> | <u>0.42</u> | <u>4.42</u> | <u>4.43</u> |
| | | 7.49 | 4.85 | 4.46 | 6.27 |

TABLE VII.10. Compositional Correction Terms and Associated Imprecisions for Central 69 Matrix Locations

| Material | ΔM (Plate-Pin), kg | ρ , Ih | σ_1 , Ih | σ_2 , Ih | σ , Ih |
|-------------------------------------|----------------------------------|----------------|--------------------|--------------------|------------------|
| $^{239}\text{Pu} + ^{241}\text{Pu}$ | -0.098 | -8.24 | 3.19 | 0.023 | 3.59 |
| ^{235}U | 0.035 | -1.07 | 0.0 | 0.033 | 0.033 |
| ^{238}U | 1.80 | 2.34 | 2.91 | 0.71 | 3.33 |
| Mo | -0.035 | 0.11 | 0.017 | 0.01 | 0.02 |
| Fe, Ni, Cr, Mn and Impurities | -17.98 | 15.29 | 0.49 | 4.49 | 4.51 |
| | | 8.43 | 4.34 | 4.54 | 6.65 |

TABLE VII.11. Summary of ZPPR Pin-Plate Heterogeneity Experiments

| Zone Size | Measured Reactivity, Ih | Correction for Com- positional Mismatch, Ih | Calculated Error of Correction, Ih | Half Clo- sure Error, Ih | Actual Reactivity, Ih |
|--------------|-------------------------------|---|--|--------------------------------|-----------------------------|
| 21 | -22.8 | 2.68 | 1.95 | 0.8 | 20.12 \pm 2.1 |
| 41 | -44.1 | 5.16 | 4.08 | 1.13 | 38.9 \pm 4.2 |
| 61 | -67.2 | 7.49 | 6.22 | 1.38 | 59.7 \pm 6.37 |
| 69 | -76.1 | 8.43 | 6.65 | 1.60 | 67.7 \pm 6.83 |

- c. Measurement of Shielding and Neutron Streaming. G. G. Simons
(Last reported: ANL-7753, p. 36)

(1) ZPPR-2 Dose Traverse. A traverse measurement of absorbed dose was completed at a few axial and radial positions in ZPPR-2. The dosimeter capsules used consisted of 1-in.-long \times 1/8-in.-dia (0.035-in.-wall) stainless steel sleeves, each containing three ^7LiF extruded TLD rods. As-loaded sleeves in Drawers 137-41, 137-47, 137-52, and 137-57 are shown in Fig. VII.13. The resulting data (see Table VII.12) are presented in terms of instrument readout in nanocoulombs (nC) and dose (rads) relative to the stainless steel jacket around the TLD. Conversion from nC to rads was completed using a calibrated ^{60}Co source.

Plutonium-239 foils, located 2.75 in. from the interface but near the vertical centerline of matrix drawer 139-37, and the TLD rods were exposed simultaneously for a nominal 892 watt-hours (W-h). The $^{239}\text{Pu}(n,f)$ reaction rate was $1.018 \times 10^8 \pm 1.3\%$ reactions/(g)(W-h).^{*} The absolute foil reaction rates at the radial positions which contained TLD rods can be derived from the above reaction rate and the ^{239}Pu counter traverse for the reference core loading. The standard deviation for the batch of TLD rods was 5.8%; thus, using an average readout of three rods per capsule, the standard deviation on the reported instrument readouts will be 3.5%. However, the reported doses will have a larger error, depending upon the variation of the W parameter between the calibration-source energy (1.25 MeV) and the gamma-ray spectra in the reactor.

^{*}D. W. Maddison, ANL, private communication.

| | | | | |
|--------|-------|-------|-----|------|
| No | U3 Oa | U3 Oa | No | VOID |
| Fa3 O3 | Na | Na | S S | |
| Pu | SS | SS | S S | |
| Fa3 O3 | U3 Oa | U3 Oa | S S | |
| No | U3 Oa | U3 Oa | S S | |
| Na | U3 Oa | U3 Oa | S S | |
| U3 Oa | Na | Na | Na | |

| | | | |
|---------|---------|-----|------|
| U3 O8 | U3 O8 | Na | VOID |
| U238 | U238 | | |
| Na | Na | | |
| Na | Na | | |
| U3 O8 | U3 O8 | S S | |
| U3 O8 | U3 O8 | | |
| U238 | U238 | Na | |
| Na2 CO3 | Na2 CO3 | | |

Fig. VII.13. TLD Capsules Positioned on Top of the ZPPR Matrix Drawers for the ZPPR-2 Reference Core Dose Traverse Measurements. ANL Neg. No. 103-A11878.

TABLE VII.12. Absorbed Dose Measurements in ZPPR-2
Using Stainless Steel Encapsulated ^7LiF TLD Rods

| Capsule Tag | Matrix Drawer | Axial Position From Core C_L , in. | TLD Readout, ^a nC | Dose Relative to Steel, ^b rad |
|-------------|---------------|--------------------------------------|------------------------------|--|
| L | 137-41 | 0 | 243.3 | 2082 |
| M | | 3 | 249.9 | 2123 |
| N | | 7 | 209.2 | 1841 |
| O | | 11 | 202.1 | 1789 |
| P | | 14 | 153.6 | 1423 |
| Q | | 16 | 142.7 | 1339 |
| R | | 18 | 99.1 | 988 |
| S | | 20 | 53.8 | 569 |
| T | | 22 | 37.6 | 404 |
| U | | 26 | 24.7 | 270 |
| V | | 30 | 16.1 | 180 |
| A | 137-47 | 0 | 215.1 | 1883 |
| B | | 3 | 203.6 | 1799 |
| C | | 7 | 188.6 | 1726 |
| D | | 11 | 163.1 | 1496 |
| E | | 14 | 140.1 | 1318 |
| F | | 16 | 122.9 | 1177 |
| G | | 18 | 78.0 | 808 |
| H | | 20 | 39.7 | 427 |
| I | | 22 | 29.2 | 316 |
| J | | 26 | 20.7 | 228 |
| K | | 30 | 12.2 | 139 |
| W | 137-52 | 0 | 149.3 | 1391 |
| X | | 3 | 149.2 | 1381 |
| Y | | 7 | 137.5 | 1297 |
| Z | | 11 | 119.0 | 1151 |
| 1 | | 14 | 93.8 | 941 |
| 2 | | 16 | 80.9 | 837 |
| 3 | | 18 | 49.9 | 528 |
| 4 | | 20 | 25.5 | 279 |
| 5 | | 22 | 18.6 | 207 |
| 6 | | 26 | 12.1 | 138 |
| 7 | | 30 | 7.9 | 92 |
| 8 | 137-57 | 0 | 14.9 | 167 |
| 9 | | 3 | 15.6 | 175 |
| 10 | | 7 | 13.7 | 155 |
| 11 | | 11 | 12.2 | 140 |
| 12 | | 14 | 10.1 | 116 |
| 13 | | 16 | 9.13 | 106 |
| 14 | | 18 | 7.71 | 89 |
| 15 | | 20 | 6.98 | 82 |
| 16 | | 22 | 5.75 | 68 |
| 17 | | 26 | 4.01 | 48 |
| 18 | | 30 | 2.62 | 32 |

^aStandard deviation $\pm 3.5\%$.

^bStandard deviation dependent on gamma-ray spectra $\geq 3.5\%$.

B. Support of ZPR Fast Critical Experiments

1. Fast Critical Experiments; Theoretical Support--Illinois. C. E. Till (02-134)

a. Supplementary Analytical Interpretation of Integral Data (Last reported: ANL-7798, p. 99)

(1) A Multiregion, Perturbation, Integral Transport Formulation for the Analysis of Central Sample-worth and Doppler-effect Measurements (P. H. Kier and M. Salvatores). A computer code, based on perturbation theory and integral transport theory, is being written to aid in the analysis of sample-worth measurements and Doppler-effect measurements made in the center of ZPR assemblies. The code essentially computes the reactivity worth of substituting a test zone for void in the center of the assembly. In contrast to an earlier code[†] in which the test zone was restricted to be a single region, this code permitted the test zone to be an arbitrary number of annular regions and therefore includes the effects of the immediate environment on the worth of a sample or its Doppler effect.

Actually, the required reactivity is obtained from the difference of two reactivities. For sample worth, in the first pass the transfer tube and sample holder would be located in the test zone, while in the second pass the transfer tube, sample holder, and sample would be located in the test zone. From the difference in reactivity between the two passes, the worth of the sample is obtained. Similarly, for the calculation of the Doppler effect, in the first pass, the buffer, oscillator drawer, and cold sample are located in the test zone, while in the second pass, the buffer, oscillator drawer, and hot sample are located in the test zone. Also the test zone should include a portion of the core.

The formulation uses broad-group real and adjoint fluxes, $\phi_{0,k}$ and $\phi_{0,k}^*$, obtained from diffusion calculations in which the center of the assembly contains core material. From the unperturbed flux, a primary surface source of neutrons impinging on the test zone and the primary-collision rates in the test zone regions $C_{1,i,k}$ are obtained. Those collisions that are scattering or fission events form the source for the second-collision generation. In general, the source in region i and group k for neutrons suffering their n th collision in the test zone, $S_{n,i,k}$ is given by

$$S_{n,i,k} = \sum_{j=1}^K \Sigma_{j \rightarrow k,i} \phi_{n-1,i,j} + \chi_k \sum_{j=1}^K (\nu \Sigma_f)_{i,j} \phi_{n-1,i,j} \quad (1)$$

[†]C. E. Till, "Fissile Doppler Effect Measurement of the Effects of Thermal Expansion," Reactor Physics Division Annual Report: July 1, 1966 to June 30, 1967, ANL-7310, pp. 143-151 (Jan 1968).

where the first term is the contribution from scattering, and the second term the contribution from virgin fission neutrons. The corresponding flux is

$$\phi_{n,i,k} = \left(\sum_{j=1}^I P_{k,i,j} S_{n,i,k} \right) / \Sigma_{i,k}, \quad (2)$$

where $P_{k,i,j}$ is the probability that neutrons appearing in group k in region j suffer their first collision in region i . Not all neutrons will suffer their next collision in the test zone, as some will leak into the core. This leakage rate for the n th generation is given by

$$L_{n,i,k} = \sum_{i=1}^I h_{k,i} S_{n,i,k}, \quad (3)$$

where $h_{k,i}$ is the probability that neutrons appearing in group k in region i escape into the core without an intervening collision in the test zone.

The reactivity effect of the test zone for the k th group is the net leakage of neutrons into the core from the test zone weighted by the unperturbed adjoint flux. Since the net leakage out of the core for primary neutrons is the same as the primary collision rate in the test zone, the reactivity can be expressed as

$$\rho_k = \frac{1}{D} \sum_{i=1}^I \left(\sum_{n=2}^{\infty} L_{n,i,k} - C_{1,i,k} \right) \phi_{u,i,k}^*, \quad (4)$$

where D is the perturbation denominator. For the first pass, the appropriate unperturbed adjoint fluxes to be used in Eq. 4 are clearly the diffusion-theory fluxes $\phi_{0,k}^*$. However, for subsequent passes, the appropriate $\phi_{u,i,k}^*$ are the perturbed adjoint fluxes from the first pass. These perturbed adjoint fluxes are readily obtained from Bitelli and Salvatores'[†] integral transport formulation for the importance function. The n th-generation adjoint flux is then given by

$$\phi_{n,k,i}^* = \sum_{j=1}^I P_{k,j,i} \left[\sum_{\ell=1}^K \left(\chi_{\ell} \nu \Sigma_{f,k,j} + \Sigma_{k \rightarrow \ell, j} \right) \phi_{n-1, \ell, j}^* \right], \quad n > 1, \quad (5)$$

and for the first generation,

[†]G. Bitelli and M. Salvatores, Neutron Flux and Importance Distribution by Collision Method Starting from a Generalized Source, Nucl. Sci. Eng. 36, 309 (1969).

$$\phi_{1,k,i}^* = \sum_{\ell=1}^K h_{k,i} \left(\chi_{\ell} \nu \Sigma_{f,k} + \Sigma_{k \rightarrow \ell} \right) \phi_{0,\ell}^* \quad (6)$$

where the cross sections are for core material.

2. Fast Critical Experiments; Theoretical Support--Idaho. W. G. Davey
(02-010)

a. ZPR Heterogeneity Method Development. R. G. Palmer
(Last reported: ANL-7825, p. 7.19)

(1) VIM-I Monte Carlo Code (F. L. Fillmore). Two VIM-I Monte Carlo calculations were made for the ZPPR-2 critical assembly using a library based on the ENDF/B Version-II cross-section data. One of the calculations was for a heterogeneous model of the assembly containing over 40,000 zones; the other was for a homogeneous model, which was formed by homogenizing the core and blanket regions of the heterogeneous model. There were 100,000 neutron histories in each calculation. Some of the results and their comparison with experiment are presented in Tables VII.13 and VII.14. Standard deviations were not calculated for the central fission ratios, but it is estimated that they are about 0.5% or better.

Results from a completely homogeneous 2D diffusion-theory calculation give $k = 0.9524$. After a transport-theory correction of 0.0024 is added to this, it is apparent that the VIM result is about 2% lower than the multigroup result. The reason for such a large discrepancy is not understood. The heterogeneity effect obtained with VIM is $\Delta k = 0.0143 \pm 0.0054$, which is consistent with the value of about 0.012 that is expected with multigroup methods.

TABLE VII.13. ZPPR-2 Results Using ENDF/B Version-II Data

| Quantity | Homogeneous | Heterogeneous | Experiment |
|-------------------------|--------------|---------------|------------|
| Computing Time | 5.78 hr | 8.08 hr | -- |
| Collisions/history | 55.1 | 54.9 | -- |
| k | 0.9322 | 0.9465 | 1.0006 |
| Standard deviation | ± 0.0038 | ± 0.0038 | -- |
| Central F_{28}/F_{25} | 0.0209 | 0.0195 | 0.0201 |
| Central F_{49}/F_{25} | 0.9278 | 0.9201 | 0.9372 |
| Central F_{40}/F_{25} | 0.1830 | 0.1739 | 0.1704 |
| Central F_{41}/F_{25} | 1.345* | 1.385 | -- |
| Central A_{28}/F_{25} | 0.1756 | 0.1790 | -- |

TABLE VII.14. ZPPR-2 Flux Spectrum at Core Center

| Group | E _{min} keV | VIM Heterogeneous | VIM Homogeneous | Standard Deviation | 2Da Diffusion | Exper. ^b |
|-------|-------------------------|----------------------|--------------------|-----------------------|------------------|---------------------|
| | 6065.0 | 0.0033 | 0.0032 | 0.0003 | 0.0031 | - - |
| | 3679.0 | 0.0131 | 0.0123 | 0.0005 | 0.0127 | - - |
| | 2231.0 | 0.0293 | 0.0300 | 0.0010 | 0.0313 | - - |
| | 1353.0 | 0.0427 | 0.0446 | 0.0012 | 0.0455 | 0.0387 |
| | 820.9 | 0.0540 | 0.0554 | 0.0015 | 0.0544 | 0.0594 |
| | 497.9 | 0.1027 | 0.1020 | 0.0024 | 0.1018 | 0.0922 |
| | 302.0 | 0.0965 | 0.0945 | 0.0022 | 0.0986 | 0.0946 |
| | 183.2 | 0.1200 | 0.1212 | 0.0025 | 0.1243 | 0.1190 |
| | 111.1 | 0.1288 | 0.1302 | 0.0024 | 0.1296 | 0.1264 |
| | 67.4 | 0.1112 | 0.1107 | 0.0022 | 0.1103 | 0.1245 |
| | 40.9 | 0.0905 | 0.0912 | 0.0019 | 0.0868 | 0.0978 |
| | 24.8 | 0.0650 | 0.0635 | 0.0013 | 0.0609 | 0.0661 |
| | 15.0 | 0.0704 | 0.0701 | 0.0016 | 0.0673 | 0.0644 |
| | 9.11 | 0.0490 | 0.0474 | 0.0012 | 0.0500 | 0.0473 |
| | 5.53 | 0.0279 | 0.0290 | 0.0008 | 0.0285 | 0.0284 |
| | 3.35 | 0.0169 | 0.0167 | 0.0006 | 0.0177 | 0.0177 |
| | 2.04 | 0.0069 | 0.0063 | 0.0002 | 0.0064 | 0.0084 |
| | 1.23 | 0.0177 | 0.0172 | 0.0007 | 0.0180 | 0.0149 |
| | 0.75 | 0.0124 | 0.0107 | 0.0005 | 0.0122 | - - |
| | 0.45 | 0.0073 | 0.0060 | 0.0004 | 0.0073 | - - |
| | 0.28 | 0.0037 | 0.0026 | 0.0003 | 0.0032 | - - |
| | 0.17 | 0.0013 | 0.0011 | 0.0002 | 0.0023 | - - |
| | 0.10 | 0.0005 | 0.0004 | 0.0001 | 0.0003 | - - |

^aArne P. Olson, ANL, private communication.^bG. G. Simons, ANL, private communication.

The central neutron spectra shown in Table VII.14 are normalized over groups 4-18. The VIM standard deviations are about 2% over most of the experimental range. The agreement between the two VIM spectra above 3.3 keV is good. Below this energy, the heterogeneous spectrum, which is an average over the cell, is higher than the homogeneous spectrum as expected, since the heterogeneous self-shielding of resonances is stronger than the homogeneous self-shielding. The agreement between the diffusion theory and the VIM spectra are generally satisfactory, although there are small discrepancies in a few of the groups. The agreement with experiment is less satisfactory; this is not surprising, since there are deficiencies in the basic cross-section data that were used.

- b. Supplementary Analytical Interpretations of Integral Data.
R. G. Palmer (Last reported: ANL-7825, p. 7.18)

(1) Heterogeneity Correction for a Central B₄C Mockup Control Rod in ZPPR Assembly 2 (J. P. Plummer). Massive control rods in ZPPR Assembly 2 are mocked up by four drawers in a two-by-two square array. Each drawer has a central plate, 2 by 0.5 in. in cross section, of natural B₄C. The remainder of the 2.277 x 2.175-in. matrix tube is filled with sodium plus the structural stainless steel. The calculational procedure throughout the Assembly 2 preanalysis has been to homogenize uniformly over the matrix tube all the contents, i.e., boron, carbon, sodium, and stainless steel. A similar procedure was followed for the simulated tantalum control rods. An investigation was made to determine the extent of the error incurred by making this approximation, which preserves the total number of ¹⁰B atoms, N, but does not preserve $N\bar{\ell}$, where $\bar{\ell}$ is the mean chord length of the boron-containing region.

Certain idealizing assumptions were incorporated into the calculational model, chief of which was that loading 90 has a plane of symmetry along each centerline and that the centerlines pass between drawers, not bisecting a row of drawers as, in fact, is the case. The effect of these simplifications was that two-dimensional, x-y geometry calculations could be made for a central four-drawer bundle by mocking up only one quadrant of the reactor. Although not the best for comparison with experiment, this model was certainly realistic enough for a calculation of the heterogeneity correction. The cross sections were group-collapsed from the base 27-group set to seven groups as a concession to economy. This was performed by the code CCSX, using option 2 (see ANL-7518, pp. 7-11) to collapse the transport cross section for use in transport calculations. A different set of seven-group cross sections was prepared for ensuring diffusion-theory calculations, the difference being that option 4 was used to collapse the transport cross section.

The first conclusion reached was that diffusion theory would not be adequate, failing particularly in the heterogeneous-rod case. This was evident when diffusion theory predicted the heterogeneous four-drawer bundle to be worth 7¢ more than the homogenized bundle. Clearly, the effect of lumping the boron should be to reduce its worth as a neutron absorber.

Turning to transport theory, the two-dimensional S_N code DOT was used. The mesh, for both homogeneous- and heterogeneous-rod cases--as well as the normal-core reference calculation--was one interval per drawer, except for the central rod drawer and its immediate neighbors. The intervals per drawer in either the x or y direction, starting at the center and going out, were 7, 2, and the rest 1's.

The calculations were done with angular order 8. The convergence was such that a crude estimate of the corresponding error in rod

worth placed it at 1%. The results were that homogenizing the rod increased its worth by 2.7%.

A further result was that the transport correction, between calculations of the homogenized-rod worth by 2-D transport and diffusion theory, was 7.6%, the diffusion-theory worth being the greater. This compared favorably with a previous one-dimensional transport correction for a central B_4C bundle of 6.7%.

3. Fast Critical Experiments; Experimental Support--Illinois (02-013)

a. Development of Techniques for Critical Experiments.

E. F. Bennett (Last reported: ANL-7825, p. 7.20)

(1) ^{10}B Reaction Rates (T. J. Yule). The development of a small back-to-back proportional counter to measure fission and boron reaction rates was reported in ANL-7640, pp. 16-17. Both halves of the counter are operated as flow counters and standard argon-10% methane mixture (P-10) has been used as the flow gas.

For boron reaction-rate determinations, about $15 \mu\text{g}/\text{cm}^2$ of enriched metallic boron was deposited on a section of one side of the center plane. Because of the high "background" observed for the boron side when the counter was placed in a fast-neutron field, the other side of the center plane has been left blank and its half of the counter used to obtain the background (see ANL-7688, pp. 9-10).

Tests were made to determine if the background problem could be reduced by using as a flow gas one that does not contain hydrogen.

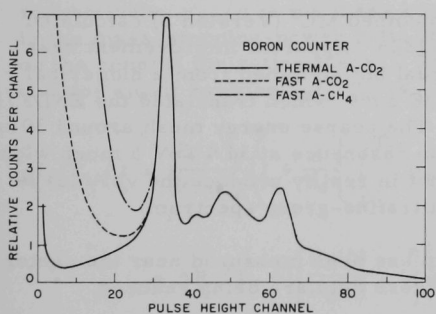


Fig. VII.14

Pulse-height Spectra from a Back-to-Back Boron Counter in a Thermal-neutron Flux and in a Fast-neutron Flux for an Argon-Carbon Dioxide Flow Mixture and an Argon-Methane Mixture

Figure VII.14 shows the response of the boron counter in a thermal-neutron flux and a fast-neutron flux for two different flow gases--the argon-methane mixture and a mixture of argon and 2% carbon dioxide. The thermal-neutron response (solid line) was the same for both gases, and only the response with the argon-carbon dioxide mixture is shown. The peak between channels 30 and 40 is associated with ^7Li recoils. Because the track lengths of these recoils are short compared with the counter dimensions and because the average energy loss in the boron film is small, the pulse-height distribution shows a well-defined peak.

The alpha particles, whose track lengths are comparable with the counter dimensions, produce a pulse-height distribution that is rather spread out because of the dependence of the pulse height on the track orientation. The upturn in the distribution below channel 5 results from the gamma-ray sensitivity of the counter.

When the counter is placed in a fast-neutron environment, the responses for both gas fillings are almost identical to the thermal response on Fig. VII.14. The fast-neutron environment was that within a block of depleted uranium with a natural uranium front face driven by thermal neutrons (Snell block). The neutron spectrum within the block is similar to that in a fast reactor; however, there are considerably fewer high-energy neutrons. Below the ${}^7\text{Li}$ peak, the dependence of the "background" on the flow gas is evident. The response for the argon-methane mixture (dot-dashed line) shows the influence of argon, carbon, and hydrogen recoils. Because of the low boron reaction rate, relative to the elastic scattering rate in the gas, the recoil distribution introduces a significant background. Hydrogen with its large elastic scattering cross section and its ability to assume the full neutron energy dominates the recoil distribution at higher energies. The response for the argon-carbon dioxide mixture (dashed line) indicates a significantly improved low-energy response and points out the desirability of using such a mixture for boron-rate measurements in a fast reactor.

4. Fast Critical Experiments; Experimental Support--Idaho.
S. G. Carpenter (02-011)

a. Neutron Spectroscopy. G. G. Simons (Last reported:
ANL-7825, p. 7.22)

An error existed in the smoothed MC² (Version 2) calculated spectrum shown in Fig. VII.4 of ANL-7825. Apparent improvement near 30 keV using Version 2 data was not real but stemmed from a numerical inaccuracy in the output from the ETOE code, which translated the ENDF/B data into the form required for MC². The coarse energy mesh around 30 keV selected in the ETOE run gave the iron resonance at 34.1 keV a much wider Γ than the actual 36 eV, which could not in reality produce the very large flux depression observed in the MC² ultrafine-group spectrum.

The fast-neutron spectrum has been measured near the center of ZPPR-2 in the pin configuration. These data are being reduced.

b. Development of Techniques for Critical Experiments.
S. G. Carpenter (Last reported: ANL-7688, p. 9)

(1) Gamma-ray Dose Measurements (G. G. Simons). An evaluation of the utility of using ${}^7\text{LiF}$ thermoluminescent rods (1 x 6 mm) to measure gamma-ray absorbed doses in ZPPR resulted in the adoption of a general

ionization theory which removed the cavity-size restriction characteristic of the Bragg-Gray type cavity-ionization theories.* It is therefore theoretically possible to relate the absorbed dose in a solid-state thermoluminescent dosimeter (TLD) cavity to the absorbed dose in the wall material irrespective of the cavity size, atomic number of the cavity, or the composition of the wall. The general ionization theory can be applied in the design of a dosimeter capsule to achieve a gamma-ray-sensitive device which has a good energy response. The energy response can also be estimated for any capsule, provided electron equilibrium is established in the sleeve and the gamma-ray spectrum is known. Based on this theory, it is possible to estimate the magnitude of systematic errors inherent in dose measurements made within the critical, provided TLD rods encased in different sleeve materials are calibrated with a standard ^{60}Co source and then exposed in fast-reactor-type gamma-ray spectra.

If the composition of the TLD and the sleeve possessed identical gamma-ray absorption coefficients, as well as the same atomic stopping power for electrons, a matched cavity condition would exist. Under these conditions, the absorbed dose in the cavity would equal the absorbed dose in the sleeve. In practice, the matched-cavity concept cannot be used in designing dosimeters for measurements in criticals. Hence, it is necessary to evaluate the wall effect for each type of sleeve material. The response of the TLD cavity relative to a TLD where there is no wall effect is

$$W = \frac{(\mu_{\text{en}}/\rho)_z}{(\mu_{\text{en}}/\rho)_c} Bf_z(T_0),$$

where the subscripts c and z refer to the TLD cavity and sleeve material, respectively, μ_{en}/ρ is the mass energy absorption coefficient, and $Bf_z(T_0)$ is the mass-stopping-power ratio for a cavity, relative to the sleeve based on the general ionization theory. Relative to the Spencer-Attix prescription for small cavities, $Bf_z(T_0)$ is

$$Bf_z(T_0, \Delta) = \frac{(Z/A)_c}{(Z/A)_z} \left(1 + \frac{d}{T_0} \left\{ \int_{-\Delta}^{T_0} R_z(T_0, T) \left[\frac{B_c(T)}{B_z(T)} - 1 \right] dT \right. \right. \\ \left. \left. + \Delta R_z(T_0, \Delta) \left[\frac{B_c(\Delta)}{B_z(\Delta)} - 1 \right] \right\} + (1-d) \left[\frac{(\mu_{\text{en}}/\rho)_c (Z/A)_z}{(\mu_{\text{en}}/\rho)_z (Z/A)_c} - 1 \right] \right),$$

where the terms are as defined by Burlin.*

Values of $Bf_z(T_0)$ for Teflon, aluminum, iron, and tantalum sleeve materials relative to LiF based on both the Laurence and Spencer-Attix theories are listed in Table VII.15. Figure VII.15 shows the energy

*T. E. Burlin, A General Theory of Cavity Ionization, Brit. J. Radiol. **39**, pp. 727-734 (1966).

TABLE VII.15. Mass Stopping Power Ratios Relative to LiF for Selected Materials

| T_o , MeV | B^f_z | | | |
|-----------------------------|---------|----------|--------|----------|
| | Teflon | Aluminum | Iron | Tantalum |
| <u>Laurence Theory</u> | | | | |
| 0.15 | 0.9644 | 0.8194 | 0.3105 | 0.1150 |
| 0.25 | 0.9664 | 0.9338 | 0.6971 | 0.1817 |
| 0.4 | 0.9714 | 0.9743 | 0.9438 | 0.424 |
| 0.6 | 0.9767 | 0.9935 | 1.0177 | 0.724 |
| 1.00 | 0.9844 | 1.0214 | 1.0794 | 1.107 |
| 1.50 | 0.9931 | 1.0402 | 1.1095 | 1.290 |
| 2.00 | 0.9974 | 1.0482 | - - | - - |
| <u>Spencer-Attix Theory</u> | | | | |
| 0.327 | 0.966 | 0.961 | 0.861 | - - |
| 0.654 | 0.980 | 0.994 | 1.027 | - - |
| 1.308 | 0.993 | 1.028 | 1.073 | - - |

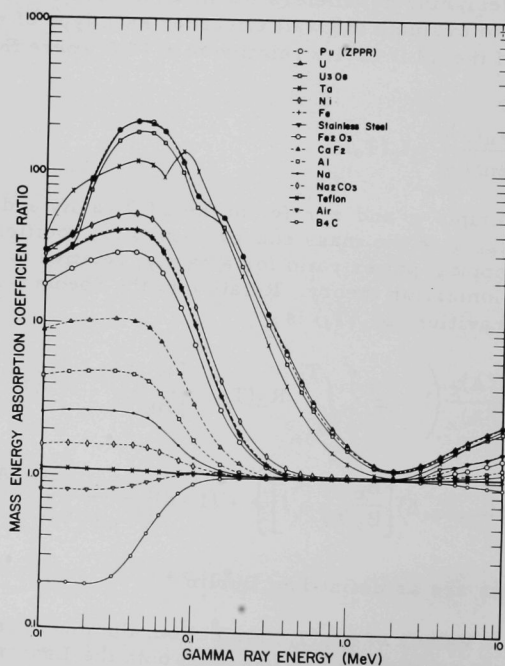


Fig. VII.15. Ratios of Mass Energy-absorption Coefficients Relative to LiF. ANL Neg. No. 103-A11870

dependence of the ratios of several mass energy absorption coefficients relative to LiF. These tabulated and plotted quantities can be used to evaluate the energy response of the dosimeter capsule.

Gamma-ray-induced excitation in dosimeter capsules containing extruded ^7LiF rod cavities and different sleeves were measured. Several capsule types were irradiated in three gamma-ray fields. Each field had a different characteristic spectrum. The TLD thermoluminescence (TL) variation as a function of sleeve type, sleeve-wall thickness, and gamma-ray energy were recorded. These experiments tested the sensitivity of the measured TL upon the capsule configuration and exposure environment. They also allowed a preliminary evaluation of the ability to predict the change in TL for different sleeves using the general ionization theory.

Table VII.16 lists the various materials, sleeve-wall thicknesses, and gamma-ray sources used, along with the resulting relative TL values. All the TL values shown in Table VII.16 are reported relative to the 0.894-g/cm^2 Teflon sleeve. It can be concluded from these data that when TLD rods with standard deviations of at least 5.8% were used, the TL read-outs were the same for individual sleeve materials, independent of the wall thickness selected for this study for each of the gamma-ray sources. Some of the TL values did vary between sources. These results do not show that the TL values are independent of sleeve thickness in general. That is, the minimum wall thickness in each case was generally at least half the range of the most energetic electrons generated in the wall by the incident gamma rays. Moreover, the maximum sleeve thicknesses were not great enough to significantly attenuate the major ^{60}Co or ^{226}Ra gamma rays. This type experiment will be performed again using TLD's with nominal standard deviations of 3%. These data may show variations as a function of the sleeve-wall thickness.

TABLE VII.16. Relative ^7LiF Response for Selected Sleeves and Gamma-ray Sources

| Sleeve Type | Sleeve Diameter in. | Sleeve Wall Thickness in. (g/cm ²) | | TLD Response Relative to 0.894-g/cm ² Teflon Sleeve | | | |
|------------------|---------------------|--|-------|--|-------------------|-------------------|-------------------|
| | | | | ^{226}Ra | ^{60}Co | ZPPR-2 | |
| | | | | | | Loading 157 | Loading 158 |
| Air | ∞ | ∞ | ∞ | - | 1.064 ± 0.090 | - | - |
| B ₄ C | 1/8" plate | 0.125 | 0.762 | - | 0.990 ± 0.084 | | |
| Teflon | 0.250 | 0.098 | 0.548 | 1.008 ± 0.086 | 1.015 ± 0.086 | 0.993 ± 0.084 | 0.896 ± 0.076 |
| | 0.375 | 0.160 | 0.894 | 1.000 ± 0.085 | 1.000 ± 0.085 | 1.000 ± 0.085 | 1.000 ± 0.085 |
| Al | 0.1875 | 0.066 | 0.453 | 1.029 ± 0.087 | 1.057 ± 0.089 | - | - |
| | 0.250 | 0.098 | 0.672 | 1.044 ± 0.089 | 1.035 ± 0.088 | - | - |
| | 0.3125 | 0.129 | 0.885 | 1.007 ± 0.085 | 1.008 ± 0.086 | - | - |
| | | | Avg: | 1.027 ± 0.087 | 1.035 ± 0.088 | | |
| SS ^a | 0.09375 | 0.020 | 0.400 | 1.104 ± 0.094 | 1.063 ± 0.090 | 1.027 ± 0.087 | 0.978 ± 0.083 |
| | 0.125 | 0.035 | 0.700 | 1.052 ± 0.089 | 1.027 ± 0.087 | 1.125 ± 0.096 | 1.038 ± 0.088 |
| | 0.1875 | 0.066 | 1.320 | 1.012 ± 0.086 | 1.057 ± 0.089 | - | - |
| | 0.250 | 0.098 | 1.959 | 1.025 ± 0.087 | 1.039 ± 0.088 | 1.067 ± 0.091 | 0.913 ± 0.078 |
| | 0.3125 | 0.129 | 2.579 | 1.007 ± 0.085 | 1.040 ± 0.088 | - | - |
| | | | Avg: | 1.040 ± 0.088 | 1.045 ± 0.089 | 1.073 ± 0.091 | 0.976 ± 0.083 |
| Ta | 0.1875 | 0.074 | 3.120 | 1.128 ± 0.096 | 1.285 ± 0.109 | 1.624 ± 0.138 | 1.531 ± 0.130 |

A preliminary evaluation of the general ionization theory was made using the data in Table VII.16. The response of a TLD in a capsule of wall material Z, relative to a TLD in a wall material Y, is

$$F = \frac{(\mu_{en}/\rho)_Z B^f_Z(T_0)}{(\mu_{en}/\rho)_Y B^f_Y(T_0)}$$

Thus the ratio of the TLD readouts for different sleeve materials should also equal F. Calculated F values were compared to the measured TL ratios of TL_Z/TL_{Teflon} (see Table VII.17).

TABLE VII.17. Theoretical and Experimental Ratios of the Effect of Sleeve Material on Cavity Excitation

| Sleeve Material | F | F Spencer-Attix | TL_Z/TL_{Teflon} |
|-----------------|----------|--------------------|--------------------|
| | Laurence | $\Delta = 81.8$ | |
| Aluminum | 1.048 | 1.041 | 1.033 ± 0.088 |
| Iron | 1.080 | 1.055 | 1.045 ± 0.089 |
| Tantalum | 1.380 | --- | 1.285 ± 0.109 |

The experimental results are in agreement with the calculated F values for all three materials. The accuracy in the tantalum F value is worse than for either iron or aluminum, since the nuclear parameters used to calculate B^f_Z for tantalum were not as precise.

The utility of using stainless steel-encased TLD dosimeters in ZPPR is reported in Sect. VII.A.2.c above.

5. Production of Materials for ZPR Experiments (02-019)

- a. Special Measurement Elements. J. E. Ayer (Not previously reported)

(1) Manufacture of Clad Fissionable Foils for ZPR Measurements (A. G. Hins). Ongoing and proposed studies of reaction rates in heterogeneous fast reactors* require thousands of clad fissionable foils for experiments conducted in the ANL-operated zero-power reactors. Circular and rectangular foils, used in conjunction with plate-type elements, are

*R. A. Karam, G. S. Stanford, and R. Robinson, Anisotropic Effects in a 4000-liter UO₂ Fast Core, ZPR-6 Assembly 6A, Annual Mtg. Am. Nucl. Soc., Boston, Mass., June 13-17, 1971; R. A. Lewis, L. G. LeSage, C. E. Till, J. E. Marshall, E. M. Bohn, M. Salvatores, and G. S. Stanford, LMFBR Demonstration Reactor Benchmark Critical Experiments Program--Initial Plate-Rod Heterogeneity Measurements, Mtg. Am. Nucl. Soc., Boston, Mass., June 13-17, 1971.

preferred for physics studies at ambient temperature, whereas circular foils inserted between oxide-rod elements are used in variable-temperature, rodded-zone experiments.

It is desired to determine the amount of the major isotope in each foil to an accuracy of 99%. Therefore, homogeneous fuel materials and high-precision fuel weighing and analytical methods are necessary to meet the uncertainty limits. Because the fissionable foils are handled by the experimenter in unprotected surroundings, the fuel cladding must be leaktight, corrosion-resistant, and tolerant to extensive handling. Some of the foils are used repeatedly over long periods of time, demanding long-term integrity of the fuel and containment. Traceability necessitates individual permanent identification and cross reference to records of fuel content.

An activation-measurement foil consists of a fuel core sandwiched between two aluminum disks. The cladding is sealed around the periphery of the fuel by a pressure-cold-welded rim. The pressure-welded rim is about 0.004 in. thick resulting from an optimum 60% reduction of the original cladding double thickness. Cladding and core components and foils in two stages of assembly are shown in Fig. VII.16.



Fig. VII.16
Foil Components and Assemblies.
Neg. No. MSD-55128.

Foil assemblies are of three major dimensions and of two nominal thicknesses. A typical foil assembly is 1/2 in. in diameter and 0.018 in. thick. The fuel cores are 0.005 or 0.0005 in. thick and consist of eight major isotopes: ^{239}Pu , ^{240}Pu , ^{241}Pu , ^{242}Pu , ^{233}U , ^{235}U , ^{238}U , and ^{232}Th . Uranium and thorium are fabricated in the unalloyed state, but plutonium is delta-stabilized with 1.3 wt % aluminum before fabrication.

The isotopes of plutonium were procured as metal in unalloyed form or as prealloyed Pu-Al. Uranium and thorium materials were received in sheet form and required only subsequent rolling to final thickness. The plutonium alloys were melted in a vacuum-induction furnace and gravity-cast into graphite molds as 6- by 2- by 0.1-in. plates. ^{240}Pu and

^{242}Pu isotopes were alloyed with 1.3 wt % aluminum in a small arc-melting furnace. Alloy homogeneity was established by alternately melting, stirring, and solidifying the buttons through four cycles.

Foil was produced by rolling castings on a two-high Stanat mill. Plutonium plates or buttons preheated to 350°C in a resistance furnace were reduced to 0.025-in. sheet by rolling through rolls heated to 300°C . Approximately 25 passes were required to obtain the 75% reduction. The rolled sheet was trimmed and reheated to 350°C , after which rolling continued for 15-20 passes until the rolls were essentially closed. At this point, the foil was 0.007 in. thick, having been reduced 93% during primary rolling.

The plutonium-alloy thickness was further reduced by using 4- by 6-in. stainless steel packets. A stainless steel sheet was folded, the fuel material inserted, and the packet assembly warmed to 90°C and passed through rolls heated to 100°C . Cross rolling, necessary on narrow strips of fuel, was accomplished by turning the foil inside the packet before rolling. Typically, 15 passes were required to produce 0.005-in.-thick finished foils.

To produce 0.0005-in.-thick foils, the rolling operation was continued for an additional 35 passes. A 100°C roll temperature was maintained throughout, and intermediate or final annealing of the Pu-1.3 wt % Al alloy was not required.

Fuel cores produced by punching the rolled foil were visually inspected for edge burrs, tears, cracks, and other defects. Samples of the perforated foil residue were selected for chemical analysis. To obtain sufficient sample weight, large foil areas were required, resulting in good "averaging" of the fuel materials and eliminating the need to select numerous minute specimens for statistical sampling. Samples were analyzed for the major constituent, isotopic content, oxygen, carbon, nitrogen, hydrogen, and minor metallic impurities. Fuel-core weight was determined on a Mettler microbalance.

The aluminum cladding was procured in 0.005-in.-thick sheets. After the cladding was washed in acetone and alcohol and air-dried, 6- by 1-in. strips were cut from the sheet. After the oxide was removed from one surface by power wire brushing, blanks were stamped from the cladding strip with a die that contained steel and rubber platens. Concurrent with the blanking operation, a 0.003-in.-deep cavity to seat the fuel was formed in the cladding.

Foil components were loaded directly into the pressure-welding die. A cladding disk was seated, abraded side up, on the welding rim of the die base. The fuel core was removed from the storage tray,

using a vacuum pipette, and was placed in the cladding cavity. After the upper cladding disk was positioned on the fuel and the die was assembled and placed in a hydraulic press, a 20,000-lb force was applied to produce the weld. A shear ring mounted in the upper die was actuated to trim the cladding flashing, the die was opened, and alpha contamination, when present, was detected with a gas proportional probe.

Five dummy test welds were made each production day, three before assembly began and two after completion. On long production runs, a test weld was made after each 10 foils were assembled. Acceptance of the production batch of foils was contingent upon results of the test-weld examination.

Completed assemblies were removed from the glovebox and surveyed for alpha contamination on the surfaces. After each foil was identified by affixing an electroetched numeral atop the assembly, the assemblies were inspected for conformance to specifications, and foil weights were taken. Two surface surveys were made one week apart with a proportional counter to measure the alpha activity on the surface of the foils. Leakers, indicated by an increase in alpha activity, were rejected, and 50 completed foils were placed in a single holder for storage or shipment.

During the past 12 months, 1054 activation-measurement foils were produced. Foils of three elements were fabricated in the following quantities: 598 plutonium, 327 uranium, and 129 thorium. One hundred forty, or 13.3% of the foils, were rejected during assembly and inspection. Major causes for rejects were (1) excessive alpha contamination, (2) fuel misalignment in the jacket, (3) massive alpha contamination at the loading station, and (4) swelling of foil assemblies after long-term storage.

Table VII.18 shows calculated results of fuel-core content and isotope-weight uncertainty of foils selected from various production

TABLE VII.18. Isotope Content of Activation-measurement Foil

| Foil Type | Major Isotope | Fuel Core Weight, mg | Isotope Weight, mg | 2 σ Weight Uncertainty, \pm mg |
|-----------|-------------------|----------------------|--------------------|---|
| D49K | ^{239}Pu | 165.92 | 154.96 | 0.37 |
| D49N | ^{239}Pu | 24.23 | 22.54 | 0.11 |
| D49N | ^{239}Pu | 14.39 | 13.39 | 0.07 |
| VL49K | ^{239}Pu | 100.14 | 93.55 | 0.25 |
| D40K | ^{240}Pu | 159.93 | 154.05 | 0.37 |
| D42K | ^{242}Pu | 172.06 | 155.82 | 0.65 |
| D25K | ^{235}U | 170.41 | 158.50 | 0.12 |
| VL25K | ^{235}U | 90.07 | 83.78 | 0.07 |
| D28K | ^{238}U | 240.29 | 238.96 | 0.02 |
| VL28K | ^{238}U | 130.29 | 129.57 | 0.02 |
| | ^{232}Th | 141.92 | 141.55 | 0.04 |

batches shipped to the Applied Physics Division. The fuel weights range from 14 mg for 0.0005-in.-thick ^{239}Pu cores to 240 mg for 0.005-in.-thick, large-diameter uranium cores. The weight uncertainty of the major isotope varies from ± 0.65 mg in the ^{242}Pu alloy to ± 0.02 mg in the high-purity uranium material.

A 95% confidence interval may be calculated for each foil type to show weight uncertainty in percent of the major isotope present. The calculated confidence intervals, which varied from 0.02 to a maximum 1.04%, were shortest for the uranium and thorium foils. Calculated weight uncertainties for 0.005-in.-thick plutonium foils were generally from 0.5 to 0.8%, whereas 0.0005-in.-thick foils showed weight uncertainties near 1%. A portion of the uncertainty difference in the latter foils is a result of the relatively larger weighing error that occurs when weighing the 14-25-mg cores. On the basis of the 0.0005-in. plutonium foils, all production batches of activation-measurement foils met the desired 99% weight accuracy.

C. Fast Reactor Analysis and Computational Methods

1. Reactor Code Center. M. Butler, P. Henline, and M. Legan, AMD (02-085; last reported: ANL-7845, p. 7.21)

In August, 11 program packages were reviewed and placed in the Argonne Code Center library for distribution. Seven of these are program acquisitions, three are replacement packages for existing library programs, and one is an additional machine version of a library program.

The seven new programs include ACC No. 479, the FREADM-1 code* supplied by General Electric, Sunnyvale, a fast-reactor multichannel accident analysis program, which simulates a reactor transient before core disassembly. This code written in FORTRAN IV is restricted to accidents for which the assumption of radial symmetry is valid. Events, such as the mode of fuel failure or voiding, may be initiated deterministically based on selected computed variables exceeding preset levels during the accident. A second GE 635 program package received from General Electric, Sunnyvale, is the FUMBLE program (ACC No. 480). FUMBLE** is a fast-reactor fuel-burnup and management calculation. Burnup calculations carried out include the evaluation of reactivity effects, breeding (or depletion) and fuel inventories, and fuel costs for varying economic assumptions and fuel compositions throughout the reactor lifetime.

Battelle's Pacific Northwest Laboratory submitted the REPP† program (ACC No. 483), a one-dimensional heat-transfer code written for

*D. D. Freeman, E. G. Leff, D. J. Bender, and W. G. Meinhardt, The FREADM-1 Code: A Fast Reactor Excursion and Accident Dynamics Model, GEAP-13608 (Sept 1970).

**P. Greebler and C. L. Cowan, FUMBLE: An Approach to Fast Power Reactor Fuel Management and Burnup Calculations, GEAP-13599 (Nov 1970).

†R. M. Hiatt and C. Bromley, Jr., REPP: A Thermal Hydraulic Design Code for Water-Cooled Reactors, BNWL-1013 (Mar 1969).

designing boiling-water and pressurized-water reactor cores. This program can be used to determine a range of rod sizes and lattice spacings optimizing heat removal within the core. The design limits are total reactor power, burnout heat flux, and fuel centerline temperature. This code is written in FORTRAN IV for the UNIVAC 1108.

Three of the August acquisitions are written for the IBM 360. ACC No. 487 is a set of FORTRAN double-precision subprograms for calculating the properties of steam and water according to the 1967 ASME tabulations, contributed by the Baltimore Gas and Electric Company. ACC No. 489, TRIFIDO,* is a FORTRAN IV code written at the Comision Nacional de Energia Atomica, Buenos Aires, to process data from pulsed-neutron experiments calculating reactivity by the Garelis-Russell, Gozani, and Sjostrand methods. MOD-5** is a FORTRAN IV calculation of neutron time-energy distributions in the slowing-down region prepared at the U.S. Naval Postgraduate School, Monterey. A discrete Markov slowing-down model is used.

The National Neutron Cross Section Center, BNL, contributed the RAMP-1 program for the CDC-6600, which calculates scattering, capture, fission, and total cross sections according to the Reich-Moore formalism using ENDF/B Version II data.

Replacement packages have been received from the originators for the Bettis Atomic Power Laboratory's PDQ-7 program (ACC No. 275), the Idaho Nuclear Corporation's CONTEMPT (ACC No. 297) and CONTEMPT-CONPS (ACC No. 433) programs, and the Battelle Pacific Northwest Laboratory's HRG-3 (ACC No. 467) code. The new BAPL PDQ-7 version is written for the CDC-6600 computer and the SCOPE 3 Operating system. It may be used to solve, in addition to the four problem types of the earlier version (eigenvalue, boundary value, one iteration, and fixed source), additive fast-source and simplified P_L problems as well as the three-dimensional synthesis eigenvalue problem. Control searches, thermal feedback, and xenon feedback are optional. The CONTEMPT-PS package will be ACC No. 433, and ACC No. 297 will be deleted, since the new version provides the capabilities of both earlier versions and contains improvements including a factor of three in execution speed. The HRG-3 program package replacement includes some corrections, and the addition of BCD library data and an auxiliary routine for converting from the BCD library data-tape format to the binary format.

In addition, a UNIVAC 1108 version of the LEOPARD program (ACC No. 279) was received from the Jersey Nuclear Company.

*F. Difilippo and N. Pironi, TRIFIDOCodigo para calcular parámetros cinéticos en experiencias con neutrones pulsados, CNEA-Re 44 (Aug 1970).

**T. J. Williamson, MOD-5: A Computer Code for Calculations of Neutron Time-Energy Distributions in the Slowing Down Region, NPS-61WN71061A (June 1971).

PUBLICATIONS

A Neutron Spectrum Map at JANUS--A Fast Neutron Facility for Biological Exposures

E. F. Bennett, N. A. Frigerio, and T. J. Yule
Radiat. Res. 47, 353 (July 1971) Abstract

Experimental Studies of the Polarization Produced by Elastic Scattering of Neutrons in the Vicinity of 1 MeV

S. A. Cox and E. E. D. Whiting
Polarization Phenomena in Nuclear Reactions, Proc. 3rd Int. Symp.,
Madison, 1970, Ed. H. H. Barschall and W. Haerberli. Univ. of
Wisconsin Press, Madison, 1971, pp. 631-632

Analysis of Intermediate Structure in Fission Cross Section of ^{239}Pu

Yasuyuki Kikuchi
ANL-7814 (May 1971)

Analysis of Intermediate Structure in Fission Cross Section of ^{241}Pu

Yasuyuki Kikuchi
ANL-7815 (May 1971)

The ARC System Cross-section Homogenization and Modification Capabilities

E. A. Kovalsky, J. Zapatka, H. Henryson II, J. Hoover, and P. M. Walker
ANL-7714 (June 1971)

A Glass Ampoule Sealer

G. J. Pokorny and A. D. Paulsen
Nucl. Technol. 12, 141-143 (Sept 1971) Note

Group Transfer Matrices and Their Relation to Basic Cross Section Data

M. Segev
Nucl. Sci. Eng. 45, 269-278 (Sept 1971)

Space- and Energy-Dependent Neutronics in Reactor Transient Analysis

W. M. Stacey
Reactor Technol. 14(2), 169-197 (1971)

VIII. REACTOR SAFETY

A. Coolant Dynamics. H. K. Fauske
(02-114 and 02-614)1. Sodium Superheat. R. E. Henry, R. E. Holtz, and R. M. Singer
(Last reported: ANL-7833, p. 8.1)a. Single-pin Superheat Tests with Loss of Flow and Boiling Detection (Last reported: ANL-7833, p. 8.1)

During the past several years, a number of sodium-boiling experiments have been conducted. Most of these have involved the detection of incipient boiling. Several different techniques have been used, such as voltage taps, eddy-current coil pairs, pressure transducers, accelerometers, and thermocouples. Each technique had certain advantages and disadvantages, depending on the detailed application. Our experiences are summarized here.

(1) Thermocouple. To use thermocouples for the detection of incipient boiling, it is desirable to locate the thermocouple junction as close as possible to the region where boiling is expected to occur. In practice, this results in the installation of a number of thermocouples distributed over the most probable boiling region. The junctions can be located within the liquid, at the interface of the heated wall and liquid, within the heated wall, or attached to a structure that is in intimate contact with the liquid. The response of the thermocouples to a temperature change caused by boiling is maximized by using the first two locations and is somewhat less for the latter two. The actual response times depend on the proximity of the thermocouple to the point of inception and on the size and construction of the unit (i.e., bare wire, clad, ungrounded, etc.).

The type of signal emanating from a thermocouple at inception of boiling depends strongly on the thermodynamic state of the liquid at the time, i.e., whether the liquid is subcooled, saturated, or superheated. If the liquid is superheated at incipient boiling, the liquid temperature will drop rapidly to the saturation level as vaporization starts. This sudden decrease is detected easily and provides a definite instant at which boiling started, if the thermocouple junction is located relatively near the nucleation point. If the liquid is subcooled or very close to saturation at incipience, the temperature change will not be as dramatic as in the superheated case. In place of a sudden change in temperature, a change in the frequency of temperature fluctuations will result. This is usually more difficult to detect, and thus results in more error in determining the time at which nucleation occurred.

(2) Accelerometer. The ability of an accelerometer to detect incipient boiling depends on vibrations caused by growing and collapsing

vapor bubbles. In our tests, the accelerometer was mounted on a rod that was welded to the outer wall of the test apparatus. The output signal was recorded electrically and also amplified and fed into a loudspeaker. This technique did not require placement of the accelerometer close to the nucleation point, but merely required it to be in contact with a part of the structure in intimate contact with the liquid. For our purposes, the accelerometer provided an excellent qualitative indication of boiling, especially because of the audio possibilities. Again, because of the suddenness in the change of the sound level, nucleation of a superheated liquid was more readily observable than that of a saturated liquid.

(3) Eddy-current Coil Pairs. When boiling occurs, the surrounding liquid is accelerated away from the point of nucleation by the vapor growth. This liquid motion can be detected by several techniques, including an electromagnetic flowmeter in the all-liquid region or a pair of interacting eddy-current coils in the multiphase region. The latter technique was used during the sodium-expulsion tests in which a number of coil pairs were located at spaced axial positions in the flow channel. The principle of operation of the coil pairs involves the generation of a high-frequency signal in one coil that is detected in the other coil. The magnitude of the detected signal is directly proportional to the electrical conductivity of the material between the coils. Thus, the coil pair can sense the passage of a gas-liquid or vapor-liquid interface through the high-frequency field. The coils were mounted outside the flow channel and were operated at an ambient temperature of 1000°F.

Because these coils are only sensitive to an interface moving through their field, it follows that they are most accurate when a rapid vapor growth occurs. Thus, as with the previous two techniques, this technique has its best accuracy when initial superheat exists.

(4) Pressure Transducers. When a liquid suddenly boils or a vapor bubble condenses, a pressure pulse occurs that is propagated throughout the system. If a pressure transducer is located within the fluid, it is possible to detect this pressure fluctuation. The pressure rise associated with vapor growth is essentially limited by the incipient liquid superheat; so again, the detection of this pressure rise is enhanced when the liquid has significant superheat. The vapor-collapse pressure pulses, however, can be much larger than the vapor-growth pressure pulses and can be detected much more easily.

In our pool-boiling tests, a strain-gauge-type pressure transducer operating at about 500°F and located approximately 18 in. from the boiling region responded quite well to pressure disturbances caused by boiling. In our forced-flow tests, a similar transducer located downstream from the test section gave a clear indication of pressure pulses caused by vaporization and condensation. The actual location of the transducer in

either test should not have a major effect on the detection of boiling per se, but might affect the accuracy of the determination of the actual time of nucleation.

(5) Voltage Taps. For our out-of-pile experiments, the most satisfactory technique for detecting incipient boiling, both in regard to sensitivity and accuracy, was that of voltage taps that were used to measure the electrical resistance of short axial segments of the fluid and structure. This technique consisted simply of passing a small direct current through the liquid and outer structure and measuring the voltage drop in the test apparatus using wire electrodes attached to the outer-wall structure.

By such a procedure, the change in electrical resistance caused by vaporization could be detected easily; in addition, the passage of small discrete gas bubbles could be observed. This technique not only indicates when boiling begins, but also (1) the time it was initiated and (2) the space-time behavior of the liquid-vapor interfaces following inception.

2. Sodium Expulsion and Reentry: Out-of-pile. R. E. Henry and R. M. Singer (Last reported: ANL-7833, p. 8.2)

To study the expulsion and reentry phenomena and their relationship to a given LMFBR, it is necessary to achieve a close simulation of the primary factors governing the transient behavior of the coolant, such as (1) hydraulic diameter, (2) heated and unheated length, (3) upper and lower plenum regions, and (4) a close approximation to the actual flow-coastdown rate. The Out-of-Pile Expulsion and Reentry Apparatus [OPERA], which is under construction, will produce a close simulation for all these parameters. The apparatus is a once-through system in which the sodium flows from a high-pressure vessel, through the test section, and into the receiver (low-pressure) vessel. The flow transients that will be investigated are (1) an unprotected flow coastdown, and (2) partial or complete inlet flow blockages. A gas-operated control valve will be used to produce the required blockages, and the coastdown will be generated by venting the high-pressure tank through a converging-diverging depressurizing nozzle.

The basic OPERA system is identical to the R-series in-pile vehicle. Therefore, the experience gained in the system performance will be of value in designing and debugging the in-pile apparatus.

In the preparation of OPERA, the status is: (1) The high-pressure and low-pressure vessels have been fabricated, and all the welds have been checked; (2) the unistrut support structure has been completed; (3) the 22.5-in.-heated-length test section has been instrumented with inlet and outlet flowmeters, 23 outer-wall thermocouples, and 26 voltage taps; and (4) modifications for the seven-pin heater have been completed.

B. Fuel-element Failure Propagation
B. D. LaMar (02-116)

1. Out-of-pile Studies. J. B. van Erp (Last reported: ANL-7776, p. 103)

a. Fission-gas Release Studies (Last reported: ANL-7776, p. 103)

(1) Gas-release Studies in Small Pin Arrays with Nonmetallic Fluids (T. C. Chawla and E. L. Kimont). Slow-gas-release experiments, using an electrically heated test section having 19 stainless steel pins with water as coolant, were completed. Preliminary results have been reported (J. B. van Erp, C. J. Roop, and P. L. Zaleski, Simulation of Slow Fission Gas Release in an LMFBR Fuel Subassembly, Trans. Am. Nucl. Soc. 14, 1, p. 277, June 1971). Detailed analysis of the data is under way.

A series of experiments is being performed, using a three-pin unheated test section, to establish the operating conditions for the heated three-pin sodium experiment. Particular attention is being given to (a) gas-jet impingement and (b) gas blanketing immediately downstream of the in-



Fig. VIII.1

Release of Argon in a Continuous Stream into a Three-pin Test Section. Operating conditions are: circular orifice with 0.060-in. diameter, 2.5-psi pressure drop across orifice, and 20-ft/sec coolant velocity. ANL Neg. No. 900-962.

jection point for a large breach combined with a low pressure drop across the breach. Figure VIII.1 shows how, for this latter condition, the gas will stay in a confined region (one or more subchannels, depending on the release rate) over a certain axial height, before breaking up and dispersing in the test section.

For the case of Fig. VIII.1, argon was injected in a continuous stream into a three-pin test section with water as coolant. The test section consisted of one stainless steel pin and two Lucite pins. The gas was injected from the stainless steel pin through a 0.060-in.-dia hole, at a pressure drop of 2.5 psi across the hole. The coolant velocity was 20 ft/sec. A region with high void fraction is formed (having for the case of Fig. VIII.1 an axial height of approximately 2 in.), in which the coolant film could heat up. Additional tests are planned with larger gas-injection holes with slit-like shape, and for larger gas-release rates.

(2) Gas-release Studies in Sodium (R. E. Wilson). Gas-jet impingement studies using a single-channel rectangular heated test section have been completed using argon heated to 900°F. The data are being analyzed. Previous results with unheated argon have been reported (R. E. Wilson, J. B. van Erp, and H. K. Fauske, Heat Transfer to a Flowing Sodium-Gas Mixture, Trans Am. Nucl. Soc. 14, 1, p. 244, June 1971).

Fabrication of a three-pin test section for use with sodium has been completed, and assembly, instrumentation, and installation preparations for tests are under way. Ten heaters were received for this test section; however, it was necessary to reject a disappointing number of them because of faulty internal thermocouples.

The design of a seven-pin sodium test section is nearing completion. (Some redesign was necessary to accommodate the differential thermal expansion between the outer shell and inner shroud.) Fabrication of some components has started.

(3) Analytical Studies of Fission-gas Release (T. C. Chawla and C. Fiala). The sudden nearly simultaneous failure of a large number of fuel pins in an LMFBR subassembly might be caused by, e.g., (a) unprotected loss-of-flow or power-excursion accidents, causing the cladding temperatures to rise beyond their failure threshold, or (b) sudden failure of one or a small number of fuel pins at very high burnup, resulting in rapid fission-gas release and subsequent failure of neighboring pins due to generation of pressure pulses. At present, the latter mechanism is conjectural and might prove to be nonviable as more information becomes available.

The flow transients (both expulsion and reentry phases) subsequent to the occurrence of multiple-pin failures resulting in rapid fission-gas release are described here. These phenomena might be important because of reactivity effects or fuel-pin gas-blanketing times. The calculation method is based on an extension of a model that has been verified experimentally. [See T. C. Chawla and B. M. Hoglund, A Study of Coolant Transients During a Rapid Fission Gas Release in a Fast Reactor Subassembly, Nucl. Sci. Eng. 44, 320-344 (1971)]. The principal assumptions on which the model is based are: (a) The fission gas spreads out uniformly over the entire subassembly cross section, and (b) the coolant is incompressible. Furthermore, for the case reported here, it is conservatively assumed that (c) the resistance to the flow of gas within the fuel pin is negligible, and (d) the cladding breach size is so large that its effect on the gas-release rate may be neglected. Finally, the inertial and frictional contributions of the liquid columns beyond the pin bundle, as well as the three-dimensional flow effects in the outlet and inlet plenums, have been taken into account.

Figure VIII.2 gives some results for an FFTF driver fuel subassembly. The calculation of the flow transients was terminated when

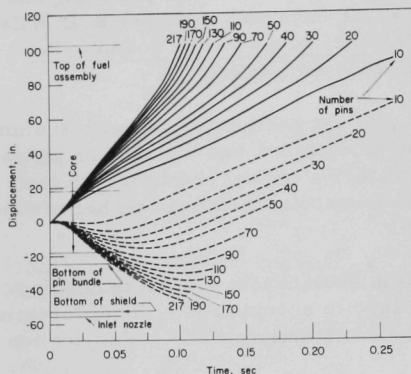


Fig. VIII.2

Displacement of Upper and Lower Gas-Liquid Interfaces, following Rapid Fission-gas Release in an FFTF Driver Fuel Subassembly, as a Function of Time, with Number of Fuel Pins Rupturing Simultaneously as Parameter. It is assumed that the axial location of the breach is at the core center, the gas-plenum pressure is 800 psia, and the coolant velocity is 25 ft/sec. ANL Neg. No. 900-933 Rev. 1.

for the case of simultaneous failure of more than ~90 pins, followed by time-staggered failure of additional fuel pins.

A model is being developed for calculating the amount of gas that might escape from the subassembly inlet nozzle after the upper liquid-gas interface has reached the subassembly outlet; the model will be verified experimentally.

As mentioned previously, these calculations are based on conservative assumptions (particularly in neglecting the flow resistance inside the fuel pins due to the presence of reflector and fuel) and thus represent an upper bound for the assumed cladding-rupture location.

b. Failure-propagation Modes Other than due to Fission-gas Release (Not previously reported)

(1) Subchannel Crossflow and Coolant-flow Starvation (T. C. Chawla). Subchannel coolant-crossflow data are needed in the analysis of fuel-failure propagation resulting from, e.g., subchannel flow blockages, fuel-pin bowing, and fission-gas release. Preliminary data are given

the upper interface reached the subassembly outlet. From Fig. VIII.2 it follows that the flow transients initiated by nearly simultaneous failure of more than ~90 pins will, under the above assumptions, result in gas blanketing of the fuel pins for time periods >0.25 sec, which is enough time for completely blanketed cladding to reach failure thresholds. Furthermore, it can be seen from Fig. VIII.2 that, if the number of pins that fail nearly simultaneously exceeds ~170, the gas could reach the subassembly inlet nozzle and enter adjacent subassemblies, so that reactivity changes would be greater than expected from a single-subassembly accident.

If the fuel pins remain gas-blanketed for times of ~0.4 sec, the cladding temperatures might exceed 1000°C. For this case, the coolant might boil on reentry near the core exit. Coolant boiling could also occur

here on subchannel crossflow, as well as on the effects of a planar flow blockage (i.e., the limiting case for coolant-flow starvation) in the heated zone, consisting of four coolant subchannels (one subchannel plus its three contiguous subchannels), on the cooling conditions in the affected subchannels.

The experiments used a test section consisting of a hexagonal array of 19 electrically resistance-heated stainless steel thin-walled pins in equilateral-triangular arrangement, which simulated part of an LMFBR subassembly. Water was used as coolant. The 72-in.-long pins were of 0.250-in. OD, were spaced at a pitch of 0.3025 in., and were wire-wrapped (wire diameter, 0.050 in.) at an axial pitch of 12 in. Thermocouples were installed inside the pins in representative subchannels at various axial locations, both in the coolant (protruding through the pin wall and insulated from it; the time constant was ~2 msec), as well as spot-welded onto the pin wall.

For the measurement of subchannel crossflow, hot water was injected at low velocity into the unheated test section through a 0.060-in.-dia hole in the wall of the central pin at an axial location 15.375 in. above the inlet grid, for various axial coolant velocities. The steady-state increases of the coolant temperatures in the subchannels at various axial and radial locations were recorded, from which the crossflow data were derived. The local axial subchannel coolant velocities were determined by introducing pulse-like temperature disturbances in the test section and measuring the transit time of the pulse between two coolant thermocouples located at different heights in the same subchannel, more than ~20 in. downstream of the source of disturbance. The crossflow coefficient, C_{ij} , is derived from the axial temperature profiles in the coolant subchannels using the equation

$$C_{ij} = \frac{\sum_{\Delta z_k}^p \frac{(w'_{ij} + w_{ij}) \Delta z_k}{\dot{m}_i}}{\sum_{\Delta z_k}^p \frac{\bar{w}_{ij} p}{\dot{m}_i}} = \frac{\sum_{\Delta z_k}^p \frac{2[T_i(z) - T_i(z + \Delta z_k)]}{3[T_i(z) - T_j(z) + T_i(z + \Delta z_k) - T_j(z + \Delta z_k)]}}$$

which is valid for fully developed flow [J. T. Rogers and N. E. Todreas, "Coolant Interchannel Mixing in Reactor Fuel Rod Bundles, Single-Phase Coolants," in Symposium Volume (V. E. Schrock, Editor), Heat Transfer in Rod Bundles, ASME Winter Meeting (1968)]. The subscripts i and j refer, respectively, to the subchannel into which hot water is injected, and to a contiguous subchannel. The left side of the equation represents the ratio of (1) the total crossflow from subchannel i to subchannel j to (2) the total axial flow in subchannel i , over an axial length equal to the axial pitch, p , of the wire-wrap. The factor 3 in the denominator of the equation accounts

for the fact that each subchannel has three contiguous subchannels, whose space-averaged behavior is assumed to be identical. For the test section described above, the coefficient C_{ij} was equal to ~ 0.39 for coolant velocities between 20 and 30 ft/sec (Re from 21,000 to 32,000). This value is in reasonably good agreement with the values found by Waters* (~ 0.4 for p from 4 to 18 in. and $Re \approx 70,000$), Baumann and Moeller** (~ 0.55 for $p = 10$ cm and $Re \approx 20,000$), and Marian and Hines† (0.48 for $p = 6$ in. and $Re \approx 55,000$).

The four-subchannel flow blockage was studied by heating the test section uniformly (maximum heat flux ~ 20 W/cm²), and recording the steady-state values of the coolant and pin-wall temperatures at various axial locations, both in subchannels behind the blockage and in not-blocked subchannels. It was found that the heat-transfer coefficient in the central subchannel of the blocked region at an axial location 0.25 in. downstream from the blockage, as determined from coolant and pin-wall temperatures, can be represented by

$$Nu = 9.58 Re^{0.28} Pr^{0.33},$$

within the range of Re values tested. The heat-transfer coefficient in unperturbed subchannels was experimentally found to follow the expression

$$Nu = 0.041 Re^{0.8} Pr^{0.33}.$$

For coolant velocities of less than about 30 ft/sec, the local heat-transfer coefficient for the blocked case was higher than that of the unblocked case, but for coolant velocities of greater than about 30 ft/sec the opposite was found. These findings are in general agreement with the trend found for the effect of turbulence on local heat transfer closely behind flow obstructions [J. Kestin, "The Effect of Free-stream Turbulence on Heat Transfer Rates," review article in *Advances in Heat Transfer*, Volume 3 (T. F. Irvine, Jr., and J. P. Hartnett, Editors), Academic Press, New York, 1966].

2. In-pile Studies. D. H. Lennox and C. C. Bolta (Last reported: ANL-7833, p. 8.6)

a. Loop Development. J. H. Tessier (Last reported: ANL-7833, p. 8.6)

Previous calculations (ANL-7833) describing the potential of the dogleg and concentric FEFP loop concepts to simulate FFTF coolant response to pressure perturbations led to the conclusion that both loop

*E. D. Waters, Fluid Mixing Experiments with a Wire Wrapped 7-Rod Bundle Fuel Assembly, HW-70178, REV (Nov 1963).

W. Baumann and R. Moeller, Experimental Study of Coolant Cross-Mixing in Multi-rod Bundles, Consisting of Unfinned, One-, Three-, and Six-fin Fuel Rods, Atomkernenergie **14, 56, 298 (1969).

†V. R. Marian and D. P. Hines, Transfer of Coolant Between Adjacent Subchannels in Wire-Wrap and Grid Spacer Rod Bundles, Trans. Am. Nucl. Soc. **13**, 2, 807 (1970).

concepts provided adequate simulation of upper slug response, but that the dogleg concept produced a poor simulation of the lower slug response because of high flow resistance in the pump leg. These analyses were based on a 37-fuel-element test subassembly and a hydraulic model describing only two fluid columns.

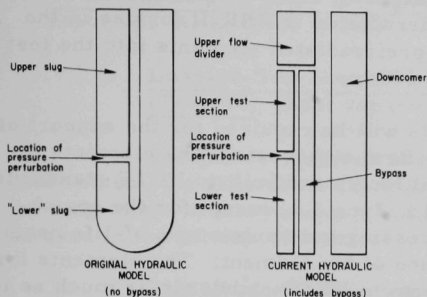


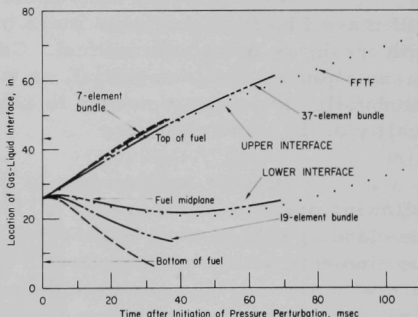
Fig. VIII.3. Original and Current Hydraulic Models

The hydraulic model has been extended to include bypass flow. Figure VIII.3 graphically illustrates the original and current hydraulic models.

Estimates of coolant response to pressure perturbations in the C2 loop caused by sodium boiling and fission-gas release have been made for test subassemblies containing 7, 19, and 37 fuel elements. Figure VIII.4 shows the results for gas release. The calculated expulsion characteristics of the C2 loop with a 37-element test subassembly are in good agreement with the characteristics calculated for a high-flow FFTF subassembly. Smaller FEFP test subassemblies show a faster response than the 37-element bundle because they contain less sodium (i.e., have smaller flow area and require less change in coolant flow rate to produce the same displacement as in a large subassembly). For the case of gas release, the bypass flow increases appreciably during the first 10 msec of the experiments and the flow through the pump decreases sharply, but does not reverse.

Fig. VIII.4

Coolant Response to Pressure Perturbation in C2 Loop Caused by Fission-gas Release. Pressure at fuel midplane is 90 psia before release and 800 psia at cladding rupture.



- b. Preparation of Experiment Plan. E. W. Barts and R. T. Curtis
(Last reported: ANL-7776, p. 106)

The fuel plan for the FEFPL test has been prepared. It identifies the fuel-element requirements for FY 1972 and FY 1973. The plan is

based on current experimental planning and on the use of the concentric FEFP in-pile loop with a helium heat exchanger and tests using either 19 full-length FFTF fuel elements or 37 shorter fuel elements. During that period, the use of preirradiated full-length FFTF fuel elements is not planned, but shorter elements can be irradiated in EBR-II for use in the test program. A facility to assemble preirradiated elements into the test train will become available during FY 1974.

A total of 293 fuel elements will be required for the support of the experimental program through the first eight tests. The elements for the first six experiments should be full length and built to FFTF standards insofar as feasible (RDT Standard E-13, Type 3.2) except for the enrichment of the uranium fraction, the processing to simulate end-of-life conditions in the fuel, and the instrumentation of the element. The elements for the next two experiments should conform to FFTF standards as much as is feasible, but in addition to enrichment and instrumentation deviations they must be shorter in both total length and length of active zone to permit irradiation in EBR-II.

The simulation of end-of-life conditions in the fuel element was examined. In general, all the effects of radiation are subjects of continuing research. In almost every case, the effects are known qualitatively and have been measured, but with considerable scatter, and the phenomena are not well-enough understood to allow prediction with substantial accuracy. For these reasons, there will be some doubt as to the steady-state conditions we wish to simulate, as well as more doubt as to the effectiveness of the simulation.

Nevertheless, reasonable efforts to simulate end-of-life fuel will make FEFP experiments more meaningful and better than if conducted with fresh, as-manufactured fuel. Continued efforts to monitor research in radiation effects is essential, as well as a selective program to develop the detailed procedures needed to achieve simulation and to verify the quality of the simulation.

Pending development of better steps to achieve simulation, the following process can be used: (1) To simulate the loss of cladding ductility, the cladding will be cold-worked 30%; (2) to simulate fission-gas buildup, the elements will be pressurized to approximately 300 psi at room temperature with argon; (3) to simulate the mechanical interaction of fuel and cladding, oversize pellets allowing only 3 to 4 mils gap will be used; (4) the other effects of irradiation can be achieved insofar as possible by irradiation in ETR and by conducting the experiments toward the end of a cycle; the fuel will be taken through at least three to four thermal cycles during the preparatory phase of the experiment; and (5) control experiments to characterize the fuel must be conducted using cladding materials that have been subjected to simulation processing.

C. Fuel Dynamics Studies in TREAT
C. E. Dickerman (02-117)

1. Transient In-pile Tests of Ceramic Fuel. C. E. Dickerman (Last reported: ANL-7845, p. 8.5)

a. Loss-of-flow Simulation with Seven-pin Cluster of Fresh Fuel (Test L2) (Last reported: ANL-7765, p. 93)

The power-calibration factor for the L2 experiment has been determined by a radiochemical analysis of the center fuel pin and a pin in the ring of six in a seven-pin assembly identical to the assembly that will be used in the L2 experiment.

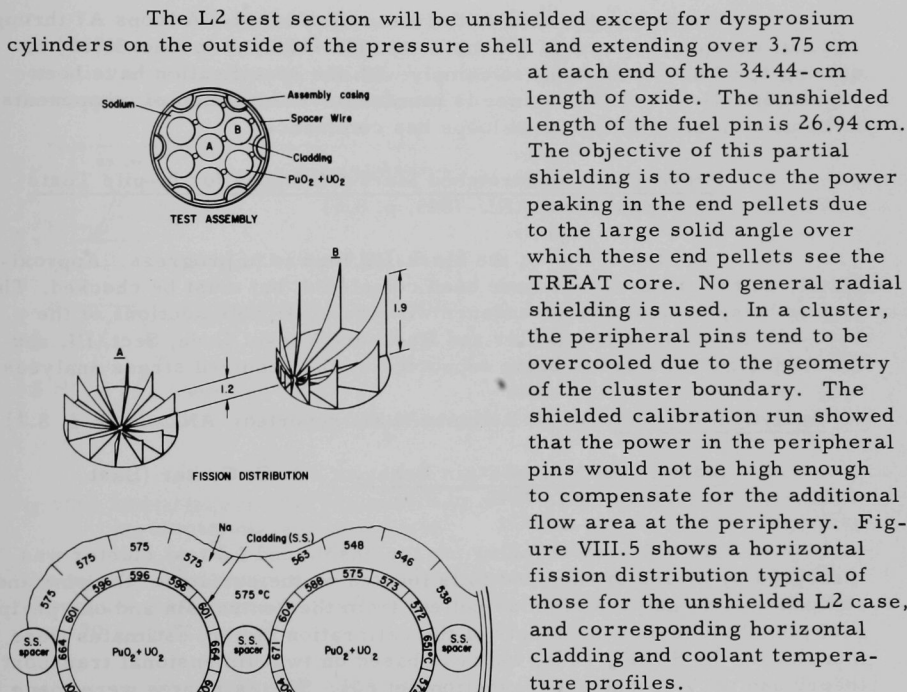


Fig. VIII.5. Horizontal Fission Distribution Typical of Those for the Unshielded L2 Case, and Corresponding Horizontal Cladding and Coolant Temperature Profiles

All the parts for the prototype void-detector system that will be tried in conjunction with the L2 experiment have been fabricated. Assembly of the L2 test section has begun.

2. Experiment Support. M. B. Rodin (Last reported: ANL-7845, p. 8.6)

a. Procurement of Mark-IIA Loops for In-pile Tests (Last reported: ANL-7845, p. 8.6)

All six Mark-IIA integral TREAT loops (through A6) have been completed. Completion of fabrication of the four closure flanges, including the two containing the enlarged penetration for placement of the thermocouples (to provide for the leads of the prototype void detector) and the two main closure clamps, is imminent. The A5 ALIP unit has been completed, and the A6 ALIP unit is undergoing final inspection. The prototype ALIP unit is being assembled. The quality-control records for the completed items are being audited.

Toward completion of the last run of Mark-IIA loops A7 through A12, all except two items of the material (TP316SS and Inconel X750) requiring special examinations to comply with the specification have been received; delivery of the balance is imminent. Fabrication of components to be used in assembling these loops has commenced.

b. Procurement of Stretched Mark-IIC Loops for In-pile Tests (Last reported: ANL-7845, p. 8.6)

Detailed design of the Mark-IIC loop is in progress. Approximately half of the drawings have been completed, but must be checked. The loop is being designed in accordance with the applicable sections of the 1971 edition of the ASME Boiler and Pressure Vessel Code, Sect. III, and the RDT Standards and is being supported by the required stress analyses.

3. Analytical Support. A. B. Rothman (Last reported: ANL-7845, p. 8.7)

a. Modeling of Multiple-pin Behavior. J. C. Carter (Last reported: ANL-7845, p. 8.9)

The calibration factor for the unshielded L2 test cluster was measured by means of enriched foils located on the surface of the pins and radiochemical analyses of oxide pellets from the central pin and one peripheral pin. Before measurements of the calibration factor, estimates were made using the SNARG code, which is based on two-dimensional transport theory and the Argonne cross-section set 201. The estimates were made in both R-Z and X-Y geometries. Table VIII.1 compares the estimates and measured values, averaged over the cross section of individual fuel pins, and over the assembly of seven pins.

In the R-Z estimate, the ring of six pins was transformed to a cylinder with approximately the same volume and surface as six 34.44-cm-long fuel pins.

TABLE VIII.1. Unshielded L2 Power Calibration Factor

| Fuel-pin Location | Calibration Factor, (J/g)/MW-sec | | |
|---|----------------------------------|------|----------|
| | R-Z | X-Y | Measured |
| 1 (central) | 3.11 | 3.50 | 3.22 |
| 2 (peripheral) | 4.72 | 5.31 | 4.49 |
| 3 | 4.72 | 5.30 | 4.59 |
| 4 | 4.72 | 5.31 | 4.69 |
| 5 | 4.72 | 5.30 | 4.67 |
| 6 | 4.72 | 5.31 | 4.57 |
| 7 | 4.72 | 5.31 | 4.48 |
| Average calibration factors for the seven-pin assembly: | | | |
| | 4.6 | 5.04 | 4.40 |

- b. TREAT Test Analyses. T. R. Burns (Last reported: ANL-7765, p. 96)

The current version of SAS2A, including both multibubble coolant voiding and pressure variation in the vapor, has been used to analyze potential experiments for the L2 loss-of-flow simulation in TREAT. The seven-pin test section is represented in the calculation by one "average" pin and an equivalent amount of coolant and structure. The remainder of the Mark-II loop has been approximated in the code by equivalent inertial lengths.

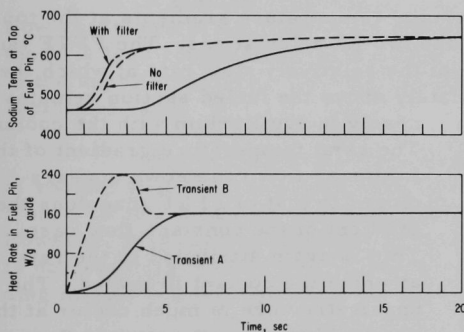


Fig. VIII.6. Effect of Shape of TREAT Transient on Duration of Steady-state Sodium Temperature

The power transient used is the overshoot Transient B shown in Fig. VIII.6. The linear power density is assumed to be a constant 10.3 kW/ft in the fueled section; steady-state power was 160 W/g. Sodium superheat was taken to be 5°C, and the two-phase friction-factor option available in SAS2A was used. A sodium-film thickness of 0.015 cm was used.

The inlet coolant temperature was assumed to remain constant at 460°C throughout the transient. Sodium exit pressure was 37 psi, and velocity was 170 g/cm²-sec.

Two different types of flow schemes were used in the L2 calculations: a constant reduced flow and, as shown in Fig. VIII.7, a linearly decreasing flow. A comparison of conditions at the top of the heated section was made between the decreasing flow, a constant flow of 40.0 g/cm²-sec, and a reference flow-coastdown calculation for FFTF. The FFTF case was a hot-channel calculation, using 14.8-kW/ft peak axial power, an initial coolant flow of 654 g/cm²-sec, and 5°C superheat. The rate of flow decay is that given in Fig. VIII.8.

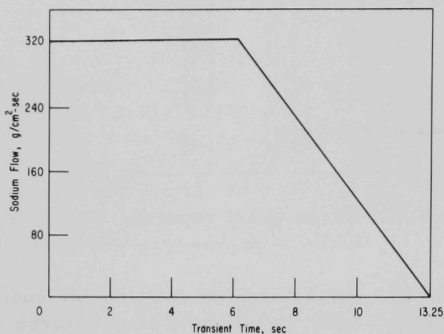


Fig. VIII.7. Test L2 Linear-flow Coastdown

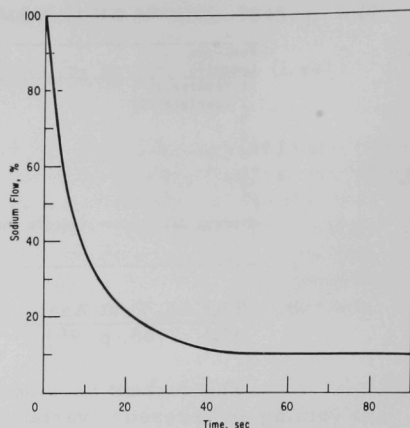


Fig. VIII.8. Primary-coolant Flow for FFTF Case

Figure VIII.9 shows the axial temperature gradients at the top of the fueled section for FFTF and the two L2 calculations. The FFTF temperature gradient is small because of the relatively slow rate at which the flow decays. The structure immediately above the fueled section remains

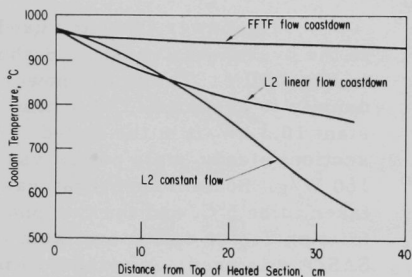


Fig. VIII.9. Comparison of Axial Temperature Gradients for Test L2 and FFTF at Boiling Initiation

nearly in equilibrium with the coolant. The axial temperature gradient of the L2 linear flow coastdown appears closer to that of FFTF than does the gradient of the constant-flow case. This is again attributed to the rate at which the coolant is heated. The upper structure is much cooler at the onset of boiling with constant flow. This is better shown in Fig. VIII.10, where the rates of coolant-temperature rise before boiling are shown for these same three cases.

Figure VIII.11 depicts the dynamics of voiding up to 1.5 sec after initiation for a constant sodium flow of $40.0 \text{ g/cm}^2\text{-sec}$. Note that in the initial stage of boiling many bubbles are formed that continually rewet the cladding and prevent overheating. Cladding dryout first occurs at the top of the fueled section 0.63 sec after boiling initiation. Melting of the cladding is calculated to occur first at this same position 1.41 sec after boiling begins. No fuel melting has taken place at the time the cladding begins to melt.

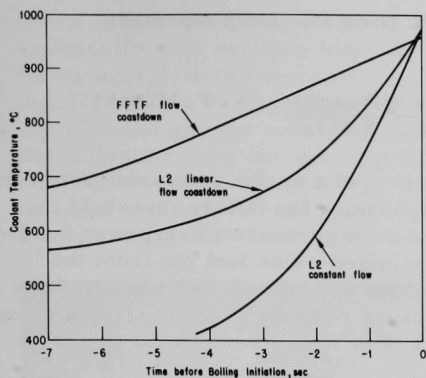


Fig. VIII.10. Rate of Coolant-temperature Rise for Test L2 and FFTF at Top of Heated Section

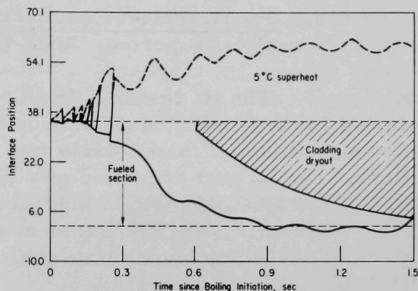


Fig. VIII.11. Dynamics of Voiding up to 1.5 sec after Initiation for a Constant Sodium Flow of $40.0 \text{ g/cm}^2\text{-sec}$

A similar sequence of events would be expected with the linear flow coastdown in L2. The main difference in the voiding dynamics is that there is less condensation at the upper interface due to higher temperatures in the upper structure. This causes the voiding to proceed somewhat more rapidly upward.

The voiding characteristics were very sensitive to the amount of sodium superheat assumed in the calculation. Increasing the superheat from 5 to 30°C resulted in boiling initiation 0.6 sec later in the transient. However, only one vapor bubble is formed with 30°C superheat, and there is no rewetting of the cladding during the first stage of boiling. The cladding melted 0.1 sec sooner in the transient with 5°C superheat.

Changing the constant flow rate over the range of $35\text{--}50 \text{ g/cm}^2\text{-sec}$ seemed to have no major effect on the sequence of events after boiling began. Boiling did not occur at a flow rate of $50 \text{ g/cm}^2\text{-sec}$, although the coolant saturation temperature was nearly reached. At lower constant flows, the only noticeable effect on the boiling characteristics was that the lower interface tended to move downward somewhat more rapidly during the initial stage of boiling. Indications are that any boiling situation that lasts $1.5\text{--}2$ sec or more will result in gross failure and melting of the cladding.

Increasing the power from 10.3 to 15 kW/ft resulted in much earlier and more violent boiling. Fuel temperatures were also relatively much higher with fuel melting occurring before cladding melting. In all cases at the lower power, melting of the cladding preceded any melting of the fuel.

4. Hot Laboratory Examinations. L. A. Niemark (Last reported: ANL-7825, p. 8.26)

a. Posttransient Examinations of Samples. W. F. Murphy (Last reported: ANL-7825, p. 8.26)

The H2 test in TREAT was part of a series of experiments conducted in the TREAT Mark-II loop to determine the failure threshold in flowing sodium of mixed-oxide fuel pins during transient overpower conditions. The H2 test consisted of a single mixed-oxide fuel pin from the PNL-17 series, with slight modifications to both the top end piece and the spiral spacer wire. The transient exposure resulted in an integrated sample power of 1485 J/g, which was sufficient to fail the element with extensive melting of fuel and cladding.

Posttest neutron radiography had indicated that failure occurred near the top of the fuel column, and appreciable quantities of fuel had been lost over the entire length of the fuel column.

When the test section containing the remains of the fuel element was removed from the loop, it was apparent that local meltthroughs of the test-section tubing had occurred. The test section was slit lengthwise at two locations 180° apart, and the parts were separated to expose the remains of the fuel element.

Visual examination revealed that the cladding appeared to have melted over the length of the fuel column, except for a small section at the bottom. The spiral spacer wire was intact where visible. An obvious tendency for the molten stainless steel to flow downward was noted, although solidification had occurred before this process had proceeded appreciably. The cinder-like remains of fuel intermixed with globules and filaments of stainless steel showed little indication of a tendency to flow downward. At least two regions of the fuel column had parts of unmelted fuel pellets. One section toward the top of the column had pellets that might be the top insulator pellets (see Fig. VIII.12); about 1.5 in. below this region, there appeared to be unmelted fuel pellets (see Fig. VIII.13). The examination is continuing.

5. Idaho Loop Operations. D. L. Mitchell (Last reported: ANL-7825, p. 8.29)

a. Unloading of TREAT Loops in Idaho Facilities

The D1 test train was unloaded successfully from its loop using the FEF inert-gas glovebox set up for interim loop-unloading operations. Samples of loop sodium indicated no sample failure. The pins and a flux monitor were removed from the test section. A preliminary macroscopic

visual inspection indicated no cladding damage. Detailed nondestructive examinations on each pin have been scheduled at the FEF, including the following: (1) detailed visual examinations and photographs, including bowing, (2) neutron radiography, (3) diametral measurements and profilometry, and (4) axial gamma scan. After these examinations, the central D1 pin, which has the fully enriched section, will be returned to Illinois for destructive examinations. If the condition of the peripheral pins is confirmed, the test section is to be reconstituted at FEF using a fresh central pin in preparation for the D1 "backup" test.

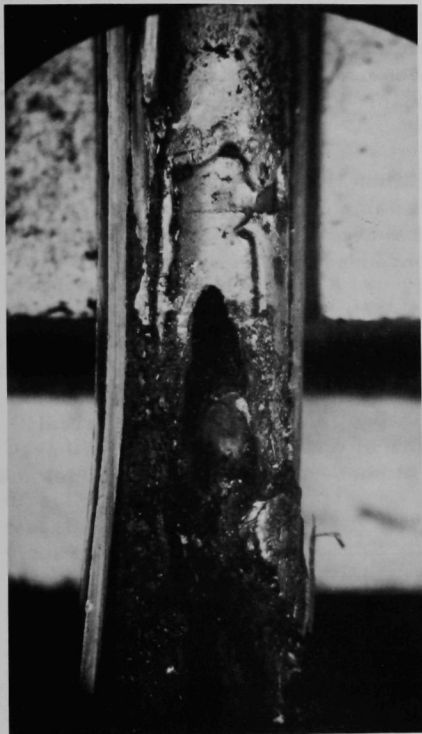


Fig. VIII.12

Section of Fuel Element PNL-17-42 near Top of Fuel Column after TREAT Exposure. Mag. ~3X. Neg. No. MSD-161431.

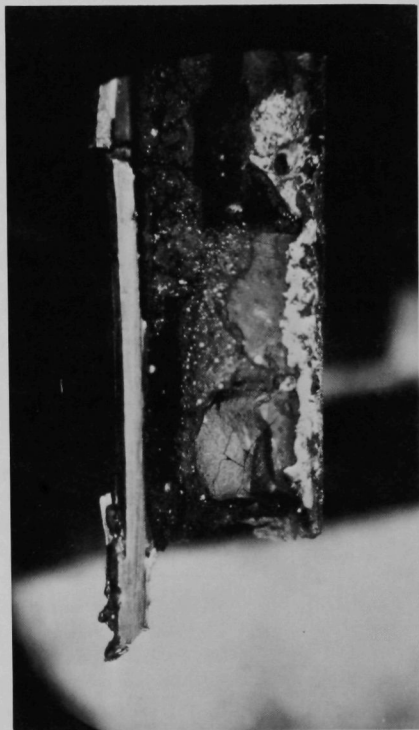


Fig. VIII.13

Section of Fuel Element PNL-17-42 about 1.5 in. below Top of Fuel Column after Treat Exposure. Mag. ~3X. Neg. No. MSD-161430.

D. High-temperature Physical Properties and Equation-of-state
of Reactor Materials. M. G. Chasanov (02-119)

1. Theoretical Extrapolation of Measured Physical Properties to Very High Temperatures. M. G. Chasanov (Last reported: ANL-7825, p. 8.30)

Calculations of equilibrium gas pressures above an LMFBR fuel-fission-product system have been carried out to 6000°K for a variety of parameters, including initial fuel composition, atom-percent burnup of the fuel, and fuel density. The model assumes the gas phase, a metallic phase, and an oxide phase to be at equilibrium in a closed system at uniform temperature. Ideal-solution theory has been used to predict the thermodynamic behavior of the various fuel and fission-product species in each of the two condensed phases.

The thermodynamic data upon which these calculations are based are statistical mechanical calculations using observed spectroscopic data for most of the gaseous oxides, and measured thermodynamic data and three-parameter extrapolations for condensed species and metallic vapor species.

Because the major contributors to the vapor pressure (noble gases at the lower temperatures and gaseous UO_2 at the higher temperatures) are not sensitive to the oxygen partial pressure, it is not surprising that the total pressure has been found to be relatively independent of the initial O/M ratio and plutonium fraction. A few of the results obtained are presented in Table VIII.2 as a function of atom-percent burnup of the fuel and

TABLE VIII.2. Gas Pressures above LMFBR Fuel-Fission-product System^a

| Burnup, % | Postburnup O/M | Partial Pressure, atm | | | | |
|---------------|-------------------|-------------------------|-------|---------------|-------------|--------------|
| | | O ₂ | Total | Alkali Metals | Noble Gases | Fuel Species |
| <u>2500°K</u> | | | | | | |
| 1 | 1.9835 | 4.04 × 10 ⁻⁶ | 31.2 | 11 | 17 | 0.02 |
| 3 | 1.9910 | 1.24 × 10 ⁻⁵ | 79.4 | 21 | 52 | 0.03 |
| 5 | 1.9972 | 2.90 × 10 ⁻⁵ | 122 | 26 | 80 | 0.05 |
| 8 | 2.0051 | 7.23 × 10 ⁻⁵ | 182 | 30 | 138 | 0.07 |
| 10 | 2.0101 | 1.15 × 10 ⁻⁴ | 220 | 31 | 173 | 0.08 |
| <u>3000°K</u> | | | | | | |
| 1 | 1.9821 | 7.51 × 10 ⁻⁴ | 42.4 | 15 | 22 | 1.4 |
| 3 | 1.9883 | 1.07 × 10 ⁻³ | 106 | 30 | 65 | 1.6 |
| 5 | 1.9947 | 1.53 × 10 ⁻³ | 161 | 37 | 108 | 1.8 |
| 8 | 2.0039 | 2.43 × 10 ⁻³ | 238 | 43 | 173 | 2.1 |
| 10 | 2.0096 | 3.14 × 10 ⁻³ | 288 | 45 | 217 | 2.3 |
| <u>4000°K</u> | | | | | | |
| 1 | 1.9788 | 1.67 × 10 ⁻¹ | 125 | 23 | 38 | 49 |
| 3 | 1.9819 | 1.63 × 10 ⁻¹ | 238 | 48 | 113 | 47 |
| 5 | 1.9868 | 1.65 × 10 ⁻¹ | 335 | 60 | 188 | 47 |
| 8 | 1.9961 | 1.76 × 10 ⁻¹ | 468 | 68 | 301 | 46 |
| 10 | 2.0031 | 1.87 × 10 ⁻¹ | 554 | 71 | 377 | 46 |
| <u>5000°K</u> | | | | | | |
| 1 | 1.9753 | 2.83 | 368 | 19 | 56 | 163 |
| 3 | 1.9752 | 2.55 | 588 | 49 | 168 | 159 |
| 5 | 1.9782 | 2.37 | 766 | 66 | 281 | 155 |
| 8 | 1.9866 | 2.23 | 1010 | 80 | 449 | 150 |
| 10 | 1.9943 | 2.18 | 1160 | 85 | 561 | 147 |
| <u>6000°K</u> | | | | | | |
| 1 | 1.9706 | 14.9 | 1190 | 9 | 83 | 72.8 |
| 3 | 1.9667 | 12.8 | 1810 | 30 | 250 | 703 |
| 5 | 1.9665 | 11.3 | 2320 | 50 | 417 | 687 |
| 8 | 1.9745 | 10.0 | 2950 | 72 | 667 | 667 |
| 10 | 1.9844 | 9.58 | 3320 | 80 | 834 | 656 |

^aInitial fuel composition = $(\text{U}_{0.8}\text{Pu}_{0.2})\text{O}_{1.98}$; fuel density = 5 g/cm^3 .

temperature for fuel of initial composition $(U_{0.8}Pu_{0.2})O_{1.98}$. In these calculations, 100% retention of fission-product species in the closed thermodynamic system was assumed. The chosen fuel density of 5 g/cm^3 is representative of that assumed in a sodium-out design-basis accident.

E. Fuel-Coolant Interactions. R. W. Wright (02-164)

1. In-pile Simulation Tests: Pressure and Work Energy. R. W. Wright, C. E. Miller, and J. J. Barghusen (Last reported: ANL-7833, p. 8.23)

a. Medium-energy Power-excursion Test (S7) (Not previously reported)

TREAT Test S7, the initial transient meltdown test that uses sections of prototypal FFTF fuel and a prototypal sodium temperature of 500°C , has been performed in the piston autoclave. The close-packed seven-pin array of fuel pins that was used was fabricated at HEDL with FFTF 0.230-in.-OD Type 316 stainless steel cladding, 0.190-in. UO_2 pellets, and 0.054-in. Type 316 stainless steel wire-wrap for pin spacing. The sodium-to-pin area ratio was 0.97. As in previous S-series tests, the lower 6 in. of the 12-in.-long two-piece pins contained UO_2 pellets. The six peripheral pins contained 10%-enriched UO_2 pellets. The center pin contained 13%-enriched UO_2 pellets to correct for flux depression, except that the two end pellets were of 10% enrichment.

A modified version of the piston autoclave was used for the first time in this test. It allows initial sodium temperatures up to 600°C to be used, and the Kaman pressure transducer (K-1903) is now mounted directly on the vessel bottom head for better frequency response. For this test, the piston did not vent the fuel chamber at full stroke as it did in previous tests.

The experimental conditions and results of Test S7 are given in Table VIII.3, and the measured pressure-time history in Fig. VIII.14. The average energy deposited in the fuel in the S7 test, $514 \text{ cal/g } UO_2$, was comparable to that in Tests S3, S5, and S6. The maximum observed pressure in Test S7 was 430 psi, and the calculated conversion ratio from thermal into mechanical energy was 6×10^{-6} . Both these values are the lowest observed in any of the S-series tests.

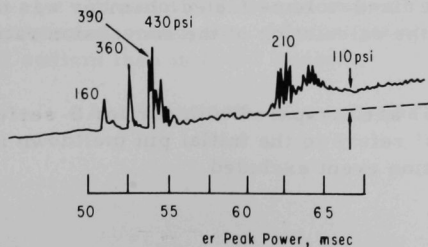


Fig. VIII.14

Pressure-response Record for Test S7

TABLE VIII.3. Experimental Conditions and Results
of Piston-autoclave Test S7

| | |
|--|--------------------------------|
| <u>Reactor characteristics</u> | |
| Peak power | 4644 MW |
| Period | 40 msec |
| Integrated power | 908 MW-sec |
| Reactivity | 2.9% |
| <u>Fuel and autoclave properties</u> | |
| Pin dimensions | 0.23-in. OD, 0.20-in. ID |
| Fuel length | 6 in. |
| Fuel internal pressure | 780 Torr |
| Mass of UO ₂ | 204 g |
| Uranium enrichment | 10%, 13% ²³⁵ U |
| Mass of sodium | 186 g |
| Mass of piston | 261 g |
| Sodium temperature | 500°C |
| Sodium-to-fuel-pin area ratio | 0.97 |
| <u>Results</u> | |
| Total fission energy | 514 cal/g UO ₂ |
| Fission energy at first pressure pulse | 360 cal/g UO ₂ |
| Amplitude of largest pressure pulse | 430 psi |
| Total impulse from all pulses | 1.3 x 10 ⁵ dyne-sec |
| Period during which pulses occurred | 15 msec |
| Calculated fractional conversion of nuclear to mechanical energy | 6 x 10 ⁻⁶ |

Test S6, like Test S7, was performed with a close-packed wire-wrapped seven-pin array, in contrast with the open square array of five fueled and four dummy pins used in previous tests. (Test S6 is described in ANL-7776, p. 119, and ANL-7833, p. 8.23.) However, Test S6 had the 0.290-in.-dia pins used in the previous tests. After the initial meltdown pressure pulses, and when the piston had reached its full travel in Test S7 as in Test S6, there was a delayed interaction between a mass of molten fuel and sodium. In Test S6, neutron-hodoscope data indicated that gross fuel motion initiated this delayed interaction. Hodoscope data for Test S7 are not yet available. In Test S6, this delayed interaction produced most of the calculated mechanical work in the event. It also produced much finely fragmented UO₂, which plugged the vents around the piston and allowed a quasi-static pressurization of the fueled chamber by sodium vapor. In Test S7, a similar quasi-static pressurization was produced in the unvented fueled chamber by the delayed interaction. In both Tests S6 and S7, this quasi-static pressurization of the fixed-volume fueled chamber was not considered to be work-producing in the calculation of the conversion ratio from thermal to mechanical energy.

The results of Test S7 are compared with earlier S-series tests in Table VIII.4, where Column S6' refers to the initial pin meltdown in Test S6 with the delayed-interaction event excluded.

TABLE VIII.4. Results of the S-series Piston-autoclave Tests

| | S3 | S4 | S5 | S6 | S6 ^a | S7 |
|---|----------------------|----------------------|----------------------|----------------------|----------------------|--------------------|
| Number of fueled pins | 5 | 5 | 5 | 7 | | 7 |
| Internal pin pressure, Torr | 780 | 780 | 5×10^{-5} | 780 | | 780 |
| Mass UO ₂ , g | 205 | 205 | 205 | 286 | | 204 |
| Ratio of sodium to fuel-pin areas | 2.2 | 2.2 | 2.2 | 0.94 | | 0.97 |
| Initial sodium temperature, °C | 170 | 165 | 165 | 210 | | 500 |
| Average specific energy, cal/g UO ₂ | 460 | 720 | 509 | 493 | 493 | 514 |
| Fission energy at first pressure pulse, cal/g UO ₂ | 440 | 480 | 430 | 380 | 380 | 360 |
| Amplitude of largest pressure pulse, psi | 540 | 1800 | 2940 | 2050 | 1800 | 430 |
| Impulse from all pulses, dyne-sec | 2.39×10^5 | 10.4×10^5 | 24.2×10^5 | 26.7×10^5 | 6.8×10^5 | 1.3×10^5 |
| Calculated conversion from nuclear to mechanical energy | 2.1×10^{-5} | 2.5×10^{-4} | 1.9×10^{-3} | 1.5×10^{-3} | 1.0×10^{-4} | 6×10^{-6} |
| Mass mean residue diameter, μ | 2700 | 1240 | 220 | 400 | -- | -- |
| Mass smaller than 41 μ , % | 1 | 2 | 17 | 4 | -- | -- |

^aS6' gives the mechanical energy, impulse, and peak pressure from the initial meltdown events in Test S6, but excludes the delayed interaction.

The results of Test S7 have received only a preliminary analysis. The relatively low pressure peaks and energy-conversion ratio appear to result from the low fuel-failure threshold energy of Test S7 in comparison with previous S-series tests. However, it is not presently known to what extent a hypothesized fundamentally lower interaction efficiency at the higher S7 sodium temperature could contribute to this result. The failure threshold listed in Table VIII.4 for Test S6 is anomalously low because, in this initial seven-pin test, 13%-enriched pellets were used for the full length of the center pin in contrast with the 10%-enriched peripheral pins. Therefore, the end pellets, where there was little flux depression, furnished hot spots and led to a "low apparent average energy" for initial pin failure.

Excluding Test S6, the 360-cal/g-UO₂ failure threshold for Test S7 is 20% lower than the 450-cal/g-UO₂ threshold of previous tests. However, the higher initial sodium temperature would add 30 cal/g UO₂ to the UO₂ energy. The higher initial sodium temperature in Test S7 would contribute to a lower failure-threshold energy than in previous tests. If the gap conductance in the prototypal FFTF fuel sections used in Test S7 is greater than in the fuel previously used, the S7 fuel would have a lower failure threshold and would give a lower peak pressure and energy-conversion ratio. However, according to the fuel-pin specifications, the gaps in the two types of pins were nearly identical (0.003 in.), and the cladding thickness was identical (0.015 in.).

It is not possible to say as yet from the S7 results that lower pressures and conversion efficiencies will result from pin meltdown in 500°C sodium than in 200°C sodium.

Analysis of the S7 results is continuing.

2. Model Development. D. H. Cho (Last reported: ANL-7783, p. 108)

a. Improvement of Basic Parametric Model of FCI (Not previously reported)

The computer program of the current basic parametric model has been improved, and a copy of the program deck with its description has been transmitted to HEDL.

The improved program considers one-dimensional one-way (upward) expansion of the heated sodium in the fuel-coolant mixing zone. Calculated are time histories of the pressure generation and coolant expansion, P-V work, and impulses from the interaction. The program can be run without interruption through all phases of the heated sodium. Three options are available for the type of constraint to be used in the program: (a) acoustic constraint for all times, (b) inertial constraint for all times, and (c) acoustic constraint up to the acoustic unloading time and inertial constraint for continuation to longer times. Complete cutoff in the heat transfer is assumed to occur by flashing of the heated sodium at the acoustic unloading time, which corresponds to the round-trip time to a free surface of the initial pressure wave. It is also assumed that upon flashing of the heated sodium at the unloading time, the pressure in the fuel-coolant mixing zone suddenly falls to the saturation pressure of the heated sodium. The ejection velocity of the unheated sodium column at the time of unloading, i.e., at the acoustic-inertial transition, is given by momentum conservation,

$$U = \int_0^T P \, dt / \rho_0 L,$$

where T is the acoustic unloading time, ρ_0 is the density of the unheated sodium column, and L is the sodium column length.

A new formulation of heat transfer has been made that takes into account such thermal resistance as might occur if the fuel particles were blanketed by a film of noncondensable gas or sodium vapor. Calculations based on the new formulation are under way.

F. Postaccident Heat Removal. L. Baker (02-165)

1. Core-debris Retention in Reactor Vessel. J. C. Hesson and E. Sowa (Last reported: ANL-7833, p. 8.34)

a. Simulation Experiments to Verify Heat-transfer Model for Internal Heat Generation in Pools (Last reported: ANL-7825, p. 8.34)

A container consisting of 6-in.-square copper electrodes, 8 in. apart, with double Pyrex-glass sides (with air space for thermal insulation)

and a water-cooled copper bottom electrically insulated from the salt water by a Pyrex-glass plate approximately 1 mm thick, was used to conduct tests in which salt water was heated electrically. The electric power input and heat transfer from the bottom (based on cooling-water flow rate and temperature increase) and from the top (by quantity of water evaporated) were determined.

Tests were conducted using pool depths of $4\frac{3}{4}$, $2\frac{3}{8}$, and $1\frac{3}{16}$ in. and three values of power input (~1.5, 2.6, and 4.4 kW) for each depth. The copper-bottom-plate temperature (which was measured) was varied by varying the cooling-water flow rate. The temperature difference across the bottom Pyrex-glass sheet (which was bonded to the copper plate by a thin water layer) was computed from the heat flux. This difference was added to the copper-bottom-plate temperature to obtain the temperature of the inner surface of the glass in contact with the salt water. The total heat flow (up and down) was checked with the power input.

Figures VIII.15-VIII.17 show the fraction of total heat flow down versus bottom-inner-surface temperature. During the tests, the internally heated salt water tended to superheat considerably, as evidenced by increased violence of boiling due to addition of salt, cold water, or

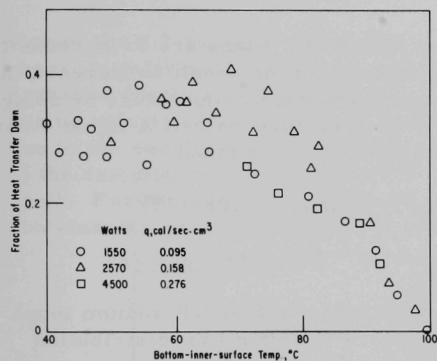


Fig. VIII.15

Heat Transfer in 4-3/4-in.-deep (3900 cm³)
Brine Pool Heated by Electrical Resistance

probes. Simple attempts to measure the superheat by thermocouples or thermometers failed because these probes acted as nucleation sites and caused immediate boiling. The variation in superheating might contribute

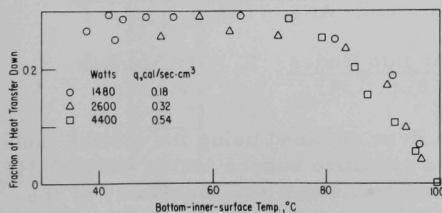


Fig. VIII.16

Heat Transfer in 2-3/8-in.-deep (1950 cm³)
Brine Pool Heated by Electrical Resistance

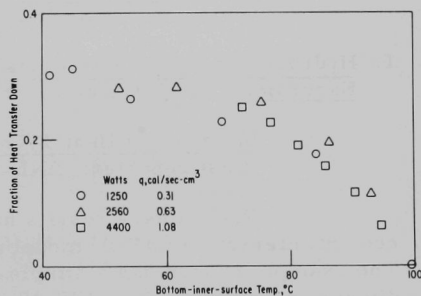


Fig. VIII.17

Heat Transfer in 1-3/16-in.-deep (975 cm³)
Brine Pool Heated by Electrical Resistance

to scatter in the data points. At higher power rates, foaming became a problem, but an antifoaming agent reduced this problem and should enable tests at higher power rates.

Figures VIII.15-VIII.17 indicate that the fraction of heat transferred down depends mainly on the bottom-inner-surface temperature in the region of 70-100°C, but is otherwise not very dependent on the parameters of the test. An attempt is being made to relate the behavior of molten UO_2 to that of the salt water in terms of density, specific heat, thermal conductivity, viscosity, coefficient of thermal expansion, latent heat of evaporation, and vapor density.

The experiments are being continued. Plans are to increase the power (specific heating rate) by using an antifoaming agent, to increase the pool depth, and to decrease the lower-inner-surface temperature by using a refrigerated coolant in place of room-temperature water. A liquid other than salt water might be used if a suitable one can be found.

G. TREAT Operations. J. F. Boland, IF (02-122)

1. Operations. J. F. Boland (Last reported: ANL-7845, p. 8.22)

Steady-state calibration runs were made on Mark-II sodium loops both with and without thermal-neutron filters to obtain flux-distribution information for future experiments RAS-L2 and RAS-H3.

a. Neutron Radiography (Last reported: ANL-7845, p. 8.22)

Neutron radiographs were made of EBR-II driver fuel and of experimental capsules from EBR-II Subassemblies X079, X086, and X080. Neutron radiographs were also made of the fuel elements from TREAT experiment RAS-D1.

H. Structural Dynamics and Containment S. H. Fistedis (02-126)

1. Hydrodynamic Response of Primary Containment to High-energy Excursion. Y. W. Chang (Last reported: ANL-7798, p. 134)

a. Insertion of Heat Transfer into Codes. T. J. Marciniak (Last reported: ANL-7798, p. 134)

Preliminary results have been obtained using the molten fuel-coolant interaction (MFCI) model as a pressure source inside REXCO-H. The example chosen has a simple geometry, being a subassembly of the dimensions shown in Fig. VIII.18. Three cases were studied: The first had a rigid vessel wall, the second a 0.1-in.-thick vessel wall with an annulus of sodium surrounding the vessel, and the third had an annulus of argon.

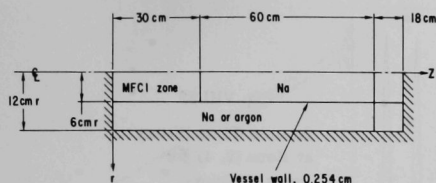


Fig. VIII.18

Simple Subassembly Used for Calculations of MFCI Model as Pressure Source Inside REXCO-H

clusion of the 0.1-in. wall with a sodium annulus caused a reduction of peak pressure to about 5000 psi; an argon annulus showed a 3000-psi maximum pressure during liquid heating. The reason for the pressure peaks occurring during calculations for Cases 2 and 3 is not clear. Apparently, they are not due to the quasi-viscous pressure term and are due either to an instability of the calculational procedure or to the natural frequency of the cylindrical shell. Further cases will be run to clarify this point. This phase of the containment-code development is being documented.

Figure VIII.19 shows the Lagrangian mesh used in REXCO-H calculations. Figures VIII.20-VIII.22 show the pressure-time histories at Zone (2, 4) in the middle of the MFCI zone. Inclusion of the flexible wall has a strong effect on the pressures developed during the liquid heating phase before vapor formation. The peak pressure reached with a rigid-wall constraint, Case 1, shows a peak pressure of about 20,000 psi. Inclusion

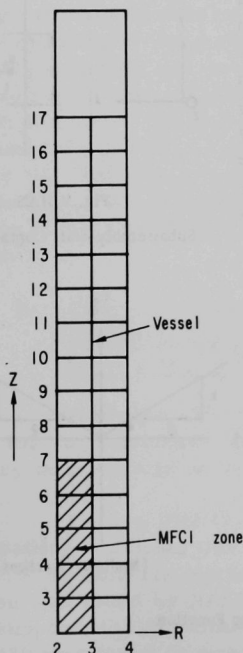


Fig. VIII.19

Lagrangian Mesh Used in REXCO-H Calculations

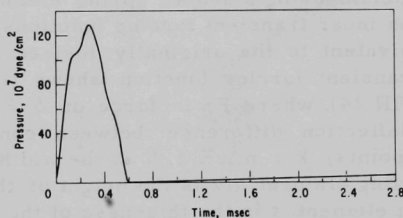


Fig. VIII.20

Pressure-Time History at Zone (2, 4) for Rigid Vessel Wall

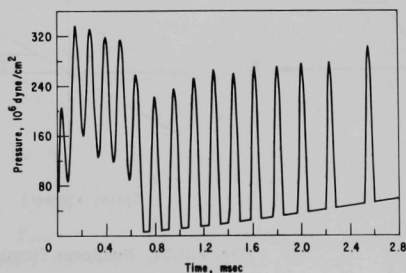


Fig. VIII.21

Pressure-Time History at Zone (2, 4) for 0.1-in.-thick Vessel Wall with an Annulus of Sodium Surrounding the Vessel

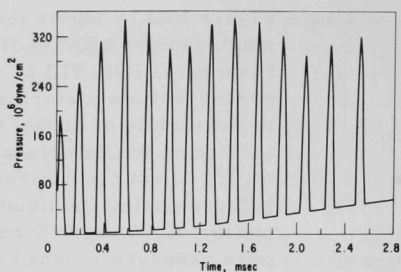


Fig. VIII.22

Pressure-Time History
at Zone (2, 4) for
Argon Annulus

2. Dynamic Response of Core Subassemblies. J. M. Kennedy (Last reported: ANL-7833, p. 8.38)

a. Development of Mathematical Model (Last reported: ANL-7833, p. 8.38)

The model for subassembly-wall contact with adjacent subassemblies (Fig. VIII.23) has been checked out. The stability problem caused by the steep-sloped nonlinear load was resolved by superimposing a scalar spring element and two nonlinear transient forcing functions, which is equivalent to the originally desired nonlinear transient forcing function (shown linear in Fig. VIII.24), where F_{δ} is force on $\delta = u_1 - u_2$ (the deflection difference between contacting mode points), $k = h\Delta z E/t$, h is the width of the contacting element, Δz is the height of the contacting element, t is the thickness of the subassembly wall, and E is Young's modulus.

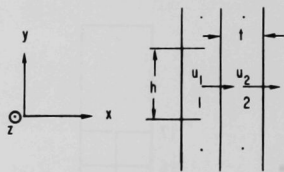


Fig. VIII.23

Subassembly-wall Contact Model

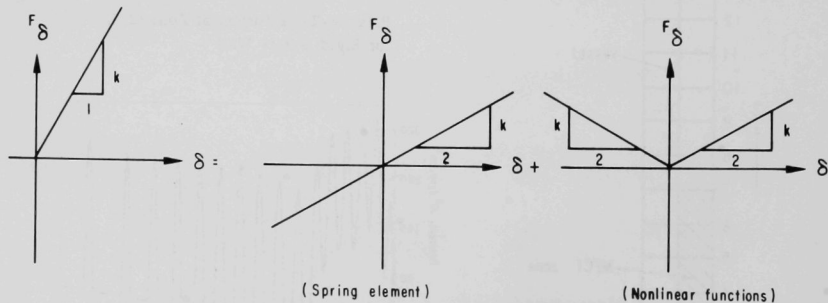


Fig. VIII.24. Nonlinear Transient Forcing Function

A sample problem for the wall-contact study was run using the schematic model shown in Fig. VIII.25. With the single unconstrained (laterally) subassembly providing the base for an indication of how much restraint

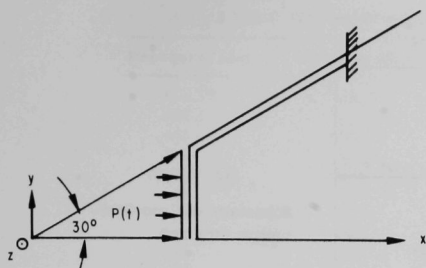


Fig. VIII.25. Schematic Model for the Sample Wall-contact Problem

checked out. The same sample problem employed in the wall-contact study using a similar schematic model (shown in Fig. VIII.26) was used for an elastic analysis. Early results indicate that the load is transmitted in much the same manner as if the adjacent walls were in contact, the corner deflection being the only value with a major change. The approximate deflection reduction for both the corner and flat midpoint of the accident subassembly was 40%; the stress level was also reduced approximately 40% for both positions. The liquid sodium was found to be moving at a slow rate through the channels, and there was no indication that wall contact was possible in this particular example problem.

is to be offered by the surrounding environment in an elastic solution, it was found that the above wall-contact model reduced the deflections approximately 45 and 15% for the flat midpoint and the corner, respectively, for the accident subassembly. The stress level was reduced approximately 45% at the flat midpoint and 40% in the corner.

The model for the liquid sodium existing in the channels between subassemblies has been partially

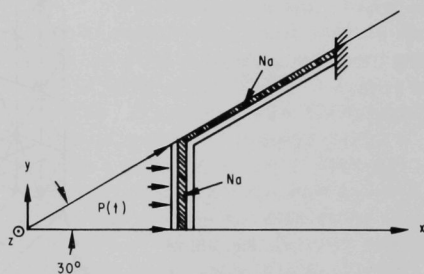


Fig. VIII.26. Schematic Model for the Liquid Sample Sodium in Channels Problem

- b. Use of Modified NASTRAN Code to Calculate Elastic and Plastic Stresses and Deformations for the FFTF Reactor Grid-support Structure (Last reported: ANL-7776, p. 133)

A stress and deflection analysis was performed for three different loading conditions on the FFTF reactor grid-support structure; primary interest was in the skirt support.

Figure VIII.27 shows the basic dimensions for the model. The first loading condition was a uniform static pressure load of 300 psi applied to the 15° symmetric-sector finite-element model in Fig. VIII.28; an elastic solution was found by NASTRAN. There was no indication of yielding in the skirt support; the maximum stress attained was only 10,100 psi. Grid point 259 was found to move down axially about 0.01 in.

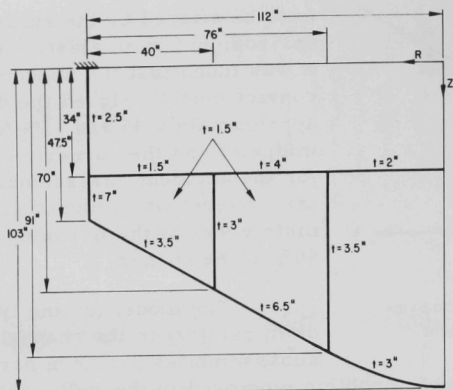


Fig. VIII.27
Schematic of Core Grid-
support Structure

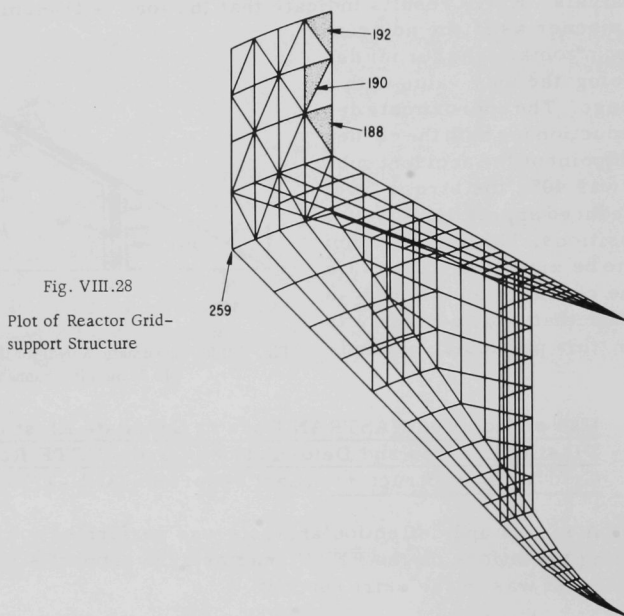


Fig. VIII.28
Plot of Reactor Grid-
support Structure

Two dynamic elastic conditions using the direct transient analysis of NASTRAN were studied by employing the results of the REXCO-H analysis on the 350-MW-sec CDA. The P-V values provided by WADCO are given in Table VIII.5; Fig. VIII.29 shows the reactor configuration used by REXCO-H in the analysis.

TABLE VIII.5. Core Sodium-vapor Expansion Values

| Pressure, atm | Volume, liters | Pressure, atm | Volume, liters |
|--------------------|----------------|---------------|----------------|
| 410.5 ^a | 1067.52 | 40 | 15610 |
| 408.2 | 1295 | 30 | 19471 |
| 400 | 2087 | 20 | 27572 |
| 375 | 2500 | 10 | 50822 |
| 350 | 2813 | 9 | 55850 |
| 325 | 3111 | 8 | 62076 |
| 300 | 3417 | 7 | 69990 |
| 200 | 4960 | 6 | 80389 |
| 100 | 8226 | 5 | 94680 |
| 90 | 8843 | 4 | 115587 |
| 80 | 9586 | 3 | 149214 |
| 70 | 10505 | 2 | 212840 |
| 60 | 11685 | 1 | 383852 |
| 50 | 13280 | | |

^aThis value was calculated by ANL based on the assumption that core vapor expanded from 1067.52 liters (core volume of ANL model) instead of 1295 liters as provided by WADCO.

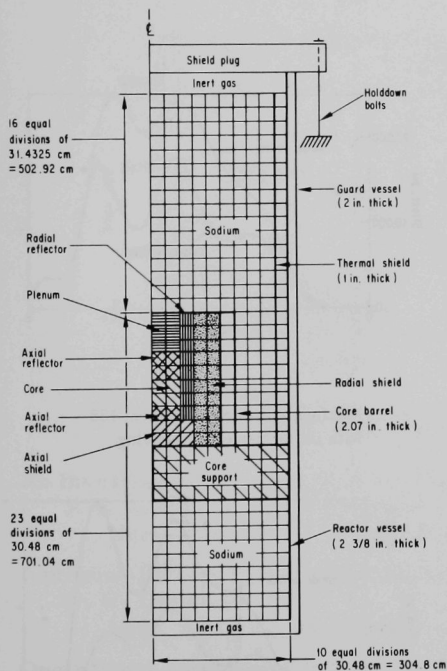


Fig. VIII.29

Reactor Model as Used
in REXCO-H Analysis

The first dynamic condition was to convert the total load on the reactor grid-support structure (obtained from REXCO-H) to a pressure loading. Then this was distributed uniformly over the upper surface of the structure as input loading. Definite yielding occurred in the core-basket region, and some yielding also occurred in the thin annulus near the skirt support. However, this yielding was thought to have little influence on the analysis of the skirt support.

The second dynamic condition was to take the pressure-difference loading on the reactor grid-support structure for the 10 horizontal divisions of the reactor configuration given in Fig. VIII.29. These pressure loads were applied to the various annulus regions of the NASTRAN finite-element model. Definite yielding again occurred in the core-basket region; however, much less yielding occurred in the thin annulus near the skirt support, because there was less direct applied load there.

The axial displacements for grid point 259 for the uniform-pressure loading and pressure-difference loading are given in Figs. VIII.30 and VIII.31, respectively. The stresses for Elements 188, 190, and 192 for the uniform and pressure-difference loadings are given in Figs. VIII.32-VIII.37. There is an indication that a small amount of yielding could occur in the skirt support, depending on the yield point of the material for both loading conditions. Higher stresses in the skirt support were attained in the pressure-difference loading condition, because the load is more centralized toward the core-basket region, causing more bending in the skirt region.

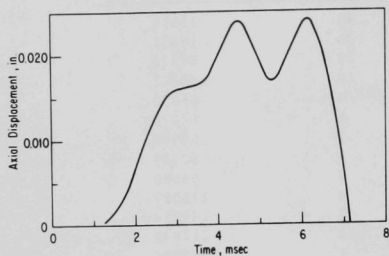


Fig. VIII.30

Axial Displacement of Grid Point 259
with Uniform-pressure Loading

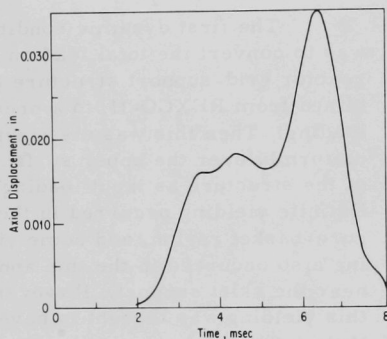


Fig. VIII.31

Axial Displacement of Grid Point 259
with Pressure-difference Loading

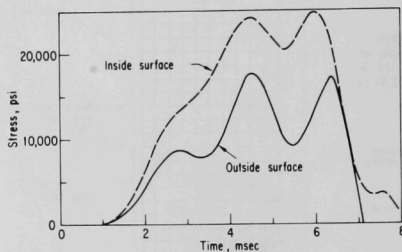


Fig. VIII.32

Maximum Stresses in Element 188
with Uniform-pressure Loading

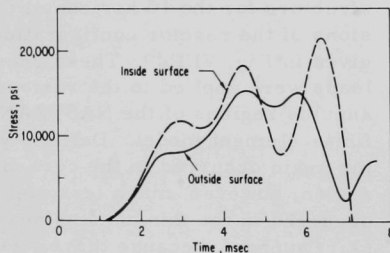


Fig. VIII.33

Maximum Stresses in Element 190
with Uniform-pressure Loading

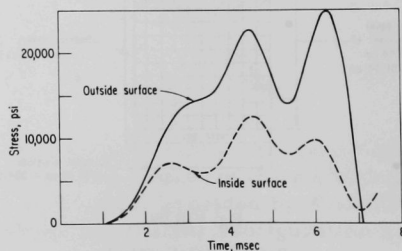


Fig. VIII.34

Maximum Stresses in Element 192
with Uniform-pressure Loading

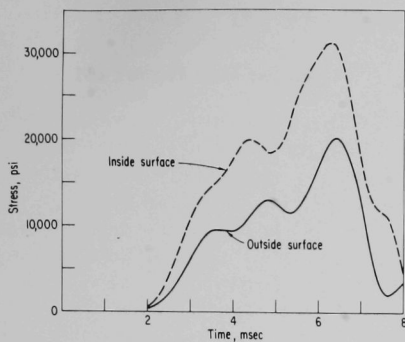


Fig. VIII.35

Maximum Stresses in Element 188
with Pressure-difference Loading

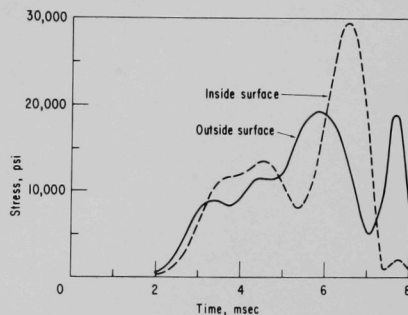


Fig. VIII.36

Maximum Stresses in Element 190
with Pressure-difference Loading

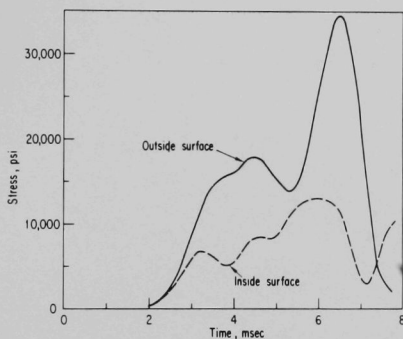


Fig. VIII.37

Maximum Stresses in Element 192
with Pressure-difference Loading

PUBLICATIONS

An Investigation of Fast-Reactor Fuel Testing in a Thermal Reactor Core

J. C. Carter and H. Greenspan

Nucl. Technol. 12, 36-45 (Sept 1971)

Radiation Effects on Superheating of Liquid Sodium

L. W. Deitrich

Nucl. Sci. Eng. 45, 218-220 (Aug 1971)

Operational Transients in LMFBR's and LWR's

J. B. van Erp and D. R. MacFarlane

Trans. Am. Nucl. Soc. 14(Suppl. 2), 39 (Aug 1971) Abstract

IX. ENVIRONMENTAL STUDIES

No report this month.

ARGONNE NATIONAL LAB WEST



3 4444 00011237 5

